MODEL BASED CONTROL WITH APPLICATIONS TO AUTOMOTIVE ENGINES

By

Stephen Daniel Pace

A DISSERTATION

Submitted to
Michigan State University
in partial fulfillment of the requirements
for the degree of

DOCTOR OF PHILOSOPHY

Electrical Engineering

2011

ABSTRACT

MODEL BASED CONTROL WITH APPLICATIONS TO AUTOMOTIVE ENGINES

By

Stephen Daniel Pace

Air-to-fuel ratio (AFR) is the mass ratio of air and fuel trapped inside a cylinder before combustion begins, and it affects engine emissions, fuel economy, and other performances. For a dual fuel engine equipped with both port-fuel-injection (PFI) and direct injection (DI) systems, the fuel ratio is the ratio of the first fuel and total fuel masses. In this research, a multi-input-multi-output sliding mode control scheme is developed with guaranteed stability to simultaneously control air-to-fuel and fuel ratios to desired levels under various air flow disturbances by regulating the mass flow rates of engine PFI and DI injection systems. A state estimator with varying parameter gain is designed with guaranteed stability to allow implementation of the proposed state feedback sliding mode controller into a Hardware-In-the-Loop (HIL) simulation environment, where the sliding mode control strategy is implemented into a production engine control module ("hardware"). The sliding mode control performance was compared with a well-tuned baseline multi-loop PID controller through HIL simulations and showed improvements, where HIL simulations were conducted to validate the feasibility of utilizing the developed controller and state estimator for automotive engines.

A dynamic linear quadratic (LQ) tracking controller is developed to regulate the transient AFR based upon a control oriented model of the engine PFI wall wetting dynamics and the transport delay between the measured air flow and manifold. The LQ tracking controller is designed to optimally track the desired transient AFR by minimizing the error between the trapped in-cylinder mass and the product of the desired AFR and fuel mass over a given time

interval. The performance of the optimal LQ tracking controller was compared with the conventional transient fueling control based on the inverse fueling dynamics through simulations and showed improvement over the baseline conventional inverse fueling dynamics controller. To validate the control strategy on an actual engine, a 0.4 liter single-cylinder direct-injection engine was used. The PFI wall-wetting dynamics were simulated in the engine controller after the DI injector control signal. Engine load transition tests for both DI and simulated PFI cases were conducted on an engine dynamometer, and the results showed improvement over the baseline transient fueling controller based on the inverse fueling dynamics.

To Daddy, Mommy, Stacey, and my entire family
For All Their
Love and Support

Acknowledgements

I would like to thank my advisor Dr. Guoming (George) Zhu for supporting me through my PhD work. His knowledge in the area of automotive engine modeling and control was invaluable in my quest to complete successful research. Also Dr. Zhu's guidance challenged me to achieve and allowed me to flourish as a PhD student.

Also, I would like to thank Xiaojian Yang, Zhen Ren, Xuefei Chen, and all the other members of the Automotive Controls Lab at Michigan State University.

Finally, I would like to thank my wife, parents, sister, and other family members and close friends for supporting me through this process.

TABLE OF CONTENTS

LIST OF TABLES

LIST OF FIGURES

Chapter 1: Introduction

Automotive internal combustion (IC) engines are designed to produce power from the energy that is contained in their fuel. More specifically, their fuel contains energy and together with air, this mixture ignites to output useable mechanical power. There are several types of fuels as well as combustion types that can be used in automotive IC engines, all of which must be controlled to optimize the fuel that is used by the engine, maximize the power that will be used to operate the vehicle, and reduce the harmful gases that are produced from the combustion.

1.1 Objective

The first objective of this work is to develop an air-to-fuel ratio (AFR) and dual fuel ratio feedback controller for an IC engine with guaranteed stability. The AFR and dual fuel ratio calculation process is a nonlinear system and thus a nonlinear controller must be designed to maintain the AFR and dual fuel ratio at desired values. Sliding mode control theory is used to adjust the fueling and achieve the nonzero target AFR and dual fuel ratio. Due to the fact that sliding mode control is a type of state feedback control, a state estimator is developed to estimate the states that are needed by the controller by using available measurements. Controlling an engine equipped with a dual fueling system and its AFR is an important way to reduce harmful emissions and improve fuel economy, making this objective is very significant.

The next objective is to design a transient feedforward AFR controller to regulate the transient AFR during engine transient operation. Linear quadratic optimal control theory will be used in the design of the transient AFR control scheme to adjust the port fuel injector fueling during these engine transient operations. Maintaining the engine AFR during these changes is important because without this control, engine fuel economy will be significantly reduced, therefore this objective is also very significant.

The last objective of this dissertation is to validate on a physical test engine the transient feedforward AFR controller and show its ability to regulate the AFR deviation during rapid engine load changes. Validating this controller on a test engine is important because this validation shows the potential to develop the controller on a production engine.

1.2 Engine Background

The application of controller deign to automotive engines is the overall topic of this dissertation. The next several sections will discuss the general operation and physical characteristics of the internal combustion engine.

1.2.1 Engine Operating Cycle

In an internal combustion engine, a piston moves up and down in a cylinder, and power is transferred through a connecting rod to a crank shaft. The continual motion of the piston and rotation of the crank shaft as air and fuel enter and exit the cylinder through the intake and exhaust valves is known as an engine cycle.

The first and most significant engine among all internal combustion engines is the Otto engine, which was developed by Nicolaus A. Otto in 1876 [1]. In his engine, Otto created a unique engine cycle that consisted of four piston strokes. These strokes are:

1. Intake stroke
2. Compression stroke
3. Expansion stroke
4. Exhaust stroke

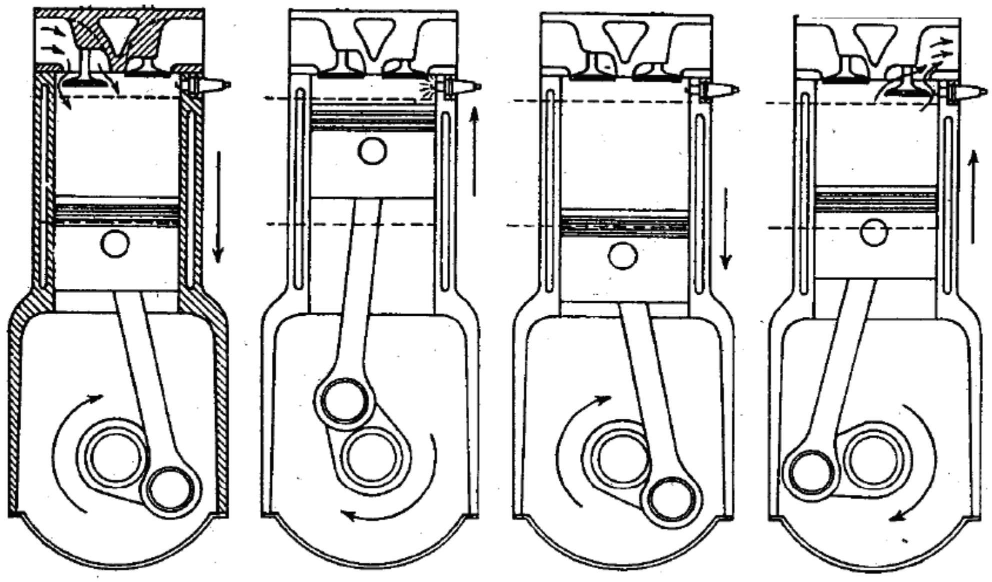

Figure 1-1: The four stroke engine cycle [1]

During the intake stroke, the piston begins at top-dead-center (TDC) and ends at bottom-dead-center (BDC). An air and gasoline mixture enters the cylinder through the intake valve and in some cases, this valve opens slightly before the intake stroke begins to allow more air-fuel mixture into the cylinder.

During the compression stroke, the intake and exhaust valves are closed and the mixture is compressed to a very small fraction of its initial volume. The compressed mixture is then ignited by a spark causing the pressure to rise very rapidly.

During the expansion stroke, the piston begins at TDC. Due to the high pressure and temperature gases in the cylinder, the piston is now pushed down, causing the crank to rotate. As the piston approaches BDC the exhaust valve opens.

During the exhaust stroke, the burned gases exit the cylinder due to the high cylinder pressure and low exhaust pressure and also due to the piston moving up towards TDC. The cycle starts again after the exhaust valve closes.

A complete engine cycle is divided into 720 crank angle degrees, where the crank angle is between the piston connecting rod at TDC and the connecting rod away from TDC. This means that the piston will move up and down in the cylinder two times during one complete engine cycle. Since there are two revolutions in one engine cycle, time duration (in seconds) of one engine cycle can be found given the rotations-per-minute (RPM). For example, at 1500 RPM, an engine cycle lasts 80 ms (ms) and at 3000 RPM an engine cycle lasts 40 ms.

Although, the Otto cycle was created many years ago, it remains a commonly used engine design. As previously mentioned, the modeling of the entire process of the internal combustion engine is a very complicated one, which involves modeling of thermal dynamics. This research intent is to develop a simple cylinder pressure model that can be used in real-time simulation for controller design and validation purposes.

1.2.2 Combustion Process

In developing a valid engine model of spark-ignition engines, the concept of the combustion process must be understood. The combustion process is relatively simple and it begins with fuel and air being mixed together in the intake manifold and cylinder. This air-fuel mixture is trapped inside the cylinder after the intake valve(s) is closed and then gets compressed. Thereafter, the compressed mixture is combusted, usually close to the end of the compression stroke, due to an electric discharge from the spark plug. The flame that is produced near the spark electrode travels through the unburned air-fuel mixture and extinguishes when it hits the combustion chamber walls. This combustion process varies from engine cycle-to-cycle and also varies from cylinder-to-cylinder. The actual combustion of the air-fuel mixture begins before the end of the compression stroke, extends through combustion stroke, and ends after the peak cylinder pressure occurs [1].

1.2.3 Abnormal Combustion

The previous explanation of the combustion process can be described as the normal combustion phenomenon. A very important abnormal combustion event is known as knock and its name arises from the audible noise that resonates from the pre-ignition of the air-fuel mixture. When the air-fuel mixture is compressed it causes the pressure and temperature to increase inside the cylinder as previously discussed. Unlike normal combustion, the cylinder pressure and temperature can rise so rapidly that it can spontaneously ignite the air-fuel mixture causing high frequency cylinder pressure oscillations. These oscillations cause the metal cylinders to produce sharp noises called knock [1].

1.2.4 Cylinder pressure

The pressure in the cylinder is a very important physical parameter that can be analyzed from the combustion process. The pressure in the cylinder is at a certain level (in the absence of combustion) because the air-fuel mixture within the cylinder is compressed. Immediately after the flame develops, the cylinder pressure steadily rises (in the presence of combustion), reaches a maximum point after TDC, and finally decreases during the expansion stroke when the cylinder volume increases.

The time at which the electrical discharge from the spark plug occurs is very important to the combustion event and must be designed to occur at the peak cylinder pressure which occurs very close to top dead center. This is done so that the maximum power or torque can be obtained. As a result, this optimum timing is called Minimal advance for the Best Torque or MBT timing. The spark timing can sometimes be advanced or retarded due to various operating conditions, which include engine speed and load, and this will result in reduced output torque or power. The optimal spark timing (or MBT timing) can also be determined using cylinder pressure signals and mass fraction burned (MFB) derived from the cylinder pressure. In recent years, two important results have been found using in-cylinder pressure signals: peak cylinder pressure occurs around 15 degrees after TDC and 50% mass fraction burned occurs at 8 to 10 degrees after TDC [2]. The velocity and acceleration of combustion can be obtained by taking the first and second derivatives of the MFB signal, which can be parameterized by a so-called Wiebe function [1]. Using the peak cylinder pressure location, 50% MFB location, and maximum acceleration of MFB as a closed loop control criterion, the MBT spark timing can be optimized in real-time.

1.3 Air-to-Fuel Ratio

1.3.1 Introduction

Air-to-fuel (A/F) ratio is the mass ratio of air and fuel trapped inside the cylinder of an engine before combustion starts. When all of the fuel in the cylinder is combined with all of the oxygen in the combustion chamber (cylinder), the mixture of air and fuel is a stoichiometric mixture. For gasoline, stoichiometry is achieved when the A/F ratio is 14.6.

In internal combustion engines, the air-to-fuel ratio is measured by a device known as an oxygen sensor, or sometimes called a lambda sensor. The sensor is located in the exhaust manifold and its main purpose is to determine how far away from stoichiometry the air-fuel mixture is. This unique location of the oxygen sensor is important in reducing the response time from the fuel injector to the sensor, which is a very important time delay that is taken into consideration in A/F ratio feedback control systems. The control of the A/F ratio in an engine will be discussed in Chapter 2 and Chapter 3.

1.3.2 Motivation of Air-to-Fuel Ratio Control

Increasing concerns about global climate changes and ever-increasing demands on fossil fuel capacity call for reduced emissions and improved fuel economy. The control of air-to-fuel ratio is an increasingly important control problem due to federal and state emission regulations. Operating the spark ignited internal combustion engines at a desired air-to-fuel ratio is necessary because the highest conversion efficiency of a three-way catalyst occurs around stoichiometric A/F ratio. This is important because the three-way catalyst helps significantly reduce post-combustion pollutants such as hydrocarbons, carbon monoxide, nitrogen oxides, particulate matter (soot), and sulfur oxide, all of which are harmful in various ways. If the AFR is too lean, where the AFR is greater than 14.6, the combustion will produce more nitrogen oxide and can reduce engine performance. Likewise, if the AFR is too rich, where the AFR is less than 14.6, the engine will waste fuel and efficiency is greatly reduced. Both of these cases demonstrate the need for AFR control, and therefore, are the motivation of this work.

1.3.3 Background of Air-to-Fuel Raito Controller Design

Over the past several decades, there have been several engine AFR controller designs where the goal is to improve the efficiency and exhaust emissions of the automotive engine. A key development in the evolution was the introduction of a closed loop fuel injection control algorithm by Rivard in 1973 [3]. This strategy was followed by an innovative linear quadratic control method in 1980 by Cassidy [4] and an optimal control and Kalman filtering design by Powers [5]. Although the theoretical design of these controllers was valid, at that time it was not realistic to implement such complex designs. Therefore, the production of these designs did not exist and engine designers did adopt the methods.

Due to the increased production of the microprocessor in the 1990's, it became practical to use these microprocessors in developing more complex control and estimation algorithms that could potentially be used in production automotive engines. Specific applications of A/F ratio control based on observer measurements in the intake manifold were developed by Benninger in 1991 [6]. Another approach was to base the observer on measurements of exhaust gases measured by the oxygen sensor and on the throttle position, which was researched by Onder [7]. These observer ideas used linear observer theory. Hedrick also used the measurements of the oxygen sensor to develop a nonlinear, sliding mode approach to control the A/F ratio [8].

All of the previous control strategies were applied to engines that used only port fuel injections, where fuel was injected in the intake manifold. The development of these control strategies for direct injection was not practical because the production of direct injection automobiles did not begin until the mid 1990's. Mitsubishi began to investigate combustion control technologies for direct injection engines in 1996 [9]. Furthermore, engines that used both port fuel and direct systems appeared a couple years ago, leading to the interest of developing the corresponding control strategies.

1.3.4 Modern Air-to-Fuel Raito Controller Design

Modern production air-to-fuel ratio control is commonly achieved by combining feedback and feedforward control of the fuel injection for a given air charge in the cylinder to achieve the desired stoichiometric mixture. Therefore, production AFR control has two components, feedback and feedfoward.

The feedback control uses measurements from the oxygen sensor to control the desired amount of fuel that should be injected over the next engine cycle and has been able to control the A/F very well. Research of the modern design of feedback AFR controllers include adaptive control [10], sliding mode control [11], linear parameter-varying control [12], and flex-fuel puddle compensation [13]. Since the feedback component is based on the oxygen sensor measurement of the AFR and due to the fuel flow transport delay, a feedforward component is added to the AFR control to reduce transient effects of the port fuel injector (PFI) wall wetting dynamics and other delays.

Conventional feed-forward AFR control is based on inverse fueling dynamics, where it is primarily derived from the estimated cylinder air charge divided by the desired stoichiometric ratio of the air and fuel ([13], [14], and [15]). In some cases, the estimated cylinder charge may have some error and slightly deviate from its real value, thus feedforward control alone can not maintain the AFR at stoichiometry.

Controlling the air-to-fuel ratio during engine transients has been a challenging control problem for many years. During rapid torque or load changes due to driver demands, automotive engines must maintain their AFR at a desired level to reduce engine emissions and maximize fuel efficiency, both of which are very difficult. Thus, there is increasing literature on improving transient AFR control, including in-cylinder air charge estimation [16], controller identification using repetitive control [17], wall-wetting dynamics compensations [18], and linear parameter varying control [19].

Both feedback and feedforward control are important in the regulation and control of AFR, and there is a need for improvement of both components. The design of an innovative sliding mode control scheme as a feedback controller and linear quadratic tracking control scheme as a feedforward controller will be discussed in Chapter 2 and Chapter 3.

1.4 HCCI Combustion

Homogeneously charged compression ignition (HCCI) combustion is a very promising combustion mode for internal combustion (IC) engines because it has the ability of meeting stringent federal and state emission regulations with improved fuel economy. In an HCCI capable IC engine, ignition is initiated by compressing the air/fuel mixture in the cylinder without using a spark plug. Therefore, HCCI combustion results in a flameless, low temperature burn that produces less nitrogen oxide (NOx) with better fuel economy. Furthermore, HCCI capable SI engines have been found to have very high fuel efficiency with significantly reduced NOx formation and reduced engine pumping loss ([20] and [21]).

The control of the HCCI combustion process has been widely studied in past decades. Through model based control, HCCI combustion control has shown significant improvement through exhaust gas recompression [22], variable valve actuation ([23],[24]), and SI and HCCI combustion mode transition ([25], [26]). During the gas exchange phase of the engine combustion process, it has been found that the timing of exhaust valve closing and intake valve opening is used to control the in-cylinder air-fuel mixture temperature [27]. More specifically, negative valve overlap (NVO), defined as the duration in crank angle in degrees between exhaust valve closing and intake valve opening, is used to adjust the exhaust gas recirculation (EGR) fraction temperature. Consequently, the in-cylinder air-fuel mixture temperature can be optimized for the desired SOC for HCCI.

Although the HCCI combustion starts without spark, it still requires an increased charge temperature (i.e. 450K) and other cylinder charge conditions to start the combustion process and therefore, its engine operational range is limited. It is limited at cold start and low engine load conditions due to the lack of sufficient thermal energy to trigger auto-ignition of the air-fuel mixture in the compression stroke, and at high engine speed and high engine load due to audible engine knock [28]. Therefore, HCCI combustion requires another combustion type, such as spark ignited (SI), to operate the engine in its full operational range. Since a specific in-cylinder gas temperature, among other charge conditions, is very critical to HCCI ignition, the control of this temperature must be taken into consideration.

Since auto-ignition timing of HCCI combustions is determined by the cylinder charge conditions, rather than the spark timing as is the case in SI combustion, regulating the charge properties, such as, temperature, pressure, and composition at intake valve closing (IVC) has been the focus of many HCCI combustion researchers. Furthermore, researchers have shown that variable valve timing (VVT) can influence the mixing conditions at IVC ([29] and [30]). Early exhaust valve closing (EVC) and late intake valve opening allow internal EGR with high temperature to be trapped in the cylinder, and this can alleviate some of the preheating that is needed to begin auto-ignition [31].

Most HCCI capable SI engines are equipped with both intake and exhaust variable valve timing (VVT) and an externally cooled exhaust gas recirculation (EGR) system which can allow the in-cylinder gas temperature and EGR fraction to be regulated. There has been various research conducted on the effects of external EGR on HCCI combustion including [32], [33], [34], and [35], and several EGR control schemes for HCCI combustion such as a robust control of external EGR [27] and model based control of EGR [36]. The development of a simplified control oriented model of the internal and external air flow into the cylinder will be discussed in detail in Chapter 5 of this dissertation. The purpose of this model is for it to be used for model-based control of the in-cylinder gas temperature and EGR fraction.

Chapter 2: Nonlinear Control of both Air-to-Fuel and Fuel Ratios for a Dual-Fuel Spark Ignited Engine

In this chapter, a multi-input-multi-output (MIMO) nonlinear control scheme will be designed with guaranteed stability to simultaneously control air-to-fuel ratio (AFR) and fuel ratio to desired levels under various air flow disturbances by regulating the mass flow rates of engine port fuel injector (PFI) and direct injector (DI) injection systems. A sliding mode controller will be used as the nonlinear control scheme, and its performance will be compared with a baseline multi-loop PID controller through simulations. Ultimately, the sliding mode controller is shown to be an improvement over the multi-loop PID controller.

2.1 Air-to-Fuel Ratio and Fuel Ratio Model

The control problem of this research is to vary both PFI and DI fuel mass injection rates ($\dot{m}_{PFI}$ and $\dot{m}_{DI}$) so that the engine AFR is regulated at a desired level (e.g., stoichiometric) and the fuel ratio of effective PFI fueling, $\dot{m}_{PFI\_E}$, to total fueling, $\dot{m}_{total} = \dot{m}_{PFI\_E}, + \dot{m}_{DI}$ is maintained at a desired value as shown in Figure 2-1. Note that the effective fueling for DI is equal to the injected DI fuel.

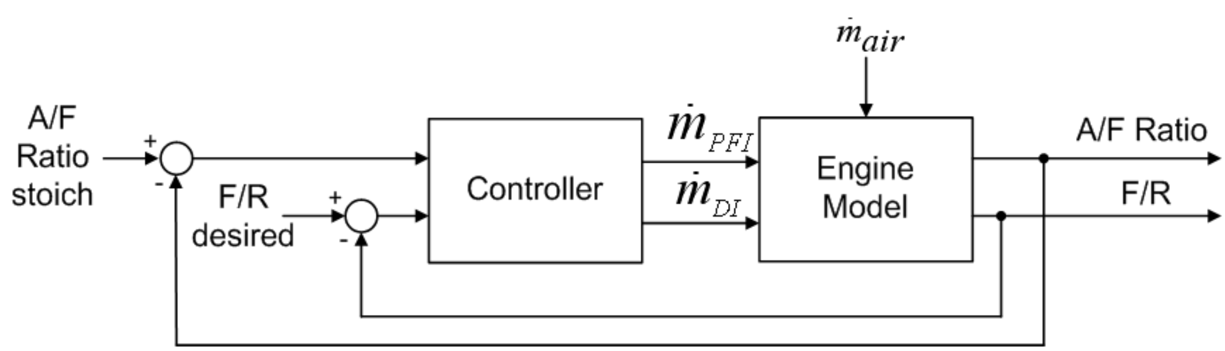

Figure 2-1: Diagram of A/F and Fuel ratio control problem

A nonlinear model for this problem, using simplified engine dynamics to model both the engine AFR and fuel ratio, is to be discussed. The air flow, $\dot{m}_{air}$, is modeled as,

$$\dot{m}_{air} = \omega = \omega_0 + \Delta\omega \tag{1}$$

where ω_0 is the nominal air flow and $\Delta\omega$ is the air flow disturbance due to the engine operational condition changes. Modeling the air flow in this way allows the study of fuel regulation due to air flow variation. The fuel flow wall-wetting model for discrete time dynamics proposed by Aquino [37] was modified for use in continuous time at a fixed engine speed of 1500RPM. Thus the wall-wetting dynamics from the port fuel injector is modeled by the following transfer function,

$$\frac{\dot{m}_{PFI\_E}(s)}{\dot{m}_{PFI}(s)} = \frac{\alpha s + 1}{\beta s + 1}, \tag{2}$$

where α and β are selected to be 0.5 and 0.8, respectively, in this model. The fuel flow from the direct injector contains negligible dynamics.

Due to the three-way catalyst used for emission control, most engines are designed to achieve a target A/F ratio around stoichiometry. For this research, the relative (normalized) target A/F ratio, λ_{target}, which is defined as the desired air-to-fuel ratio divided by the target stoichiometric air-to-fuel ratio (14.6 for gasoline), is used. Note that at stoichiometry, the relative target A/F ratio is equal to one. In the case where both gasoline and ethanol are used for the dual fueling sources, the corresponding target air-to-fuel ratio shall be used. The normalized A/F ratio can be expressed as,

$$\lambda = \frac{\dot{m}_{air}}{\mu_s \cdot \dot{m}_{total}}. \tag{3}$$

where μ_S represents the stoichiometry air-to fuel ratio. Now, the engine equivalence ratio ϕ is defined as the inverse of relative A/F ratio λ and can be approximated using equations (1) and (3) below,

$$\phi \approx \mu_s \cdot \dot{m}_{total} \left(\frac{1}{\omega_0} - \frac{1}{\omega_0{}^2} \Delta\omega \right), \tag{4}$$

where equation (1) is approximated by a first order Taylor expansion. In the remain discussion, only equivalence ratio control instead of A/F ratio is considered. The fuel ratio of the dual-fuel system is defined as the effective PFI fueling divided by total fueling, where,

$$R_{fuel} = \frac{\dot{m}_{PFI\_E}}{\dot{m}_{PFI\_E} + \dot{m}_{DI}} = \frac{\dot{m}_{PFI\_E}}{\dot{m}_{total}} \tag{5}$$

Similarly, fuel ratio, R_{fuel}, is approximated by substituting equation (4) into (5), replacing the engine equivalence ratio with the target ratio. Therefore,

$$R_{fuel} = \mu_s \cdot \dot{m}_{PFI\_E} \left(\frac{1}{\omega_0} - \frac{\Delta\omega}{\omega_0^2} \right) / \phi_{target} \cdot \tag{6}$$

The equivalence and fuel ratio model, operating at a fixed engine speed (1500RPM), includes wall-wetting dynamics of the PFI fuel system, average PFI fuel injection delay (50ms), average DI fuel injection delay (50ms), oxygen (A/F ratio) sensor delay and exhaust gas transport delay (total of 40ms), and air flow travel delay from engine throttle to cylinder (200ms). These time delays are approximated by unitary gain first order transfer functions. The complete model is divided into three subsystems, as shown in Figure 2-2, where the oxygen sensor dynamics are denoted as G1, the air flow dynamics as G2, and the fuel flow dynamics as

G3. The state space realizations of the three individual subsystems are shown in equations (7), (8), and (9).

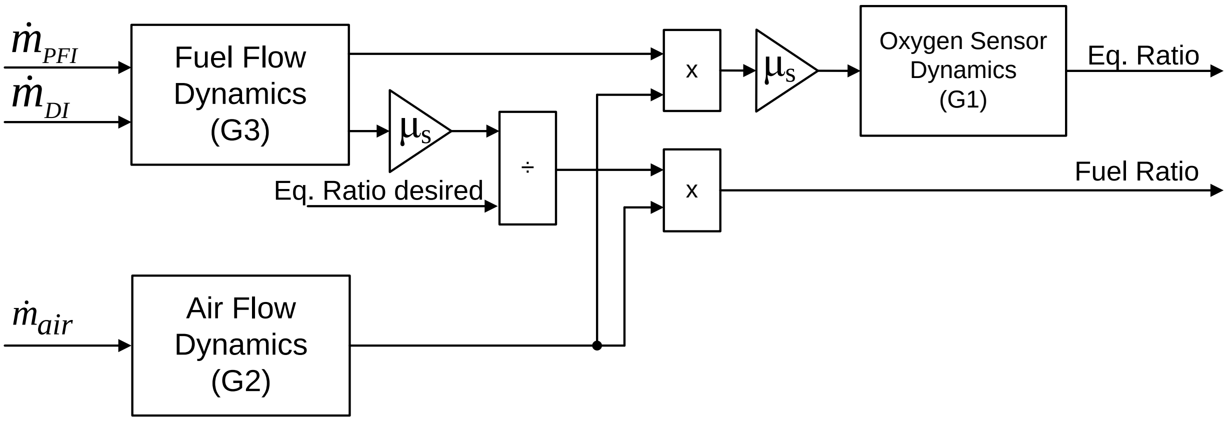

Figure 2-2: Equivalence and fuel ratio model

$$\begin{cases} \dot{x}_1 = a_1 x_1 + b_1 u_1 \\ y_1 = c_1 x_1 \end{cases} \tag{7}$$

$$\begin{cases} \dot{x}_3 = A_3 x_3 + B_3 u_3 \\ y_3 = C_3 x_3 + D_3 u_3, \ C_3 = [c_{31}^T \ c_{32}^T]^T \end{cases} \tag{8}$$

$$\begin{cases} \dot{x}_2 = a_2 x_2 + b_2 \Delta\omega \\ y_2 = c_2 x_2 \end{cases} \tag{9}$$

Note that,

$$u_1 = \mu_s \cdot y_2 \cdot y_{31}, \quad u_2 = \dot{m}_{air}, \quad u_3 = \left[\dot{m}_{PFI} \quad \dot{m}_{DI}\right]^T.$$

The entire system can be expressed by the following state-space model,

$$\dot{x} = \begin{bmatrix} a_1 & & \\ & a_2 & \\ & & A_3 \end{bmatrix} x + \begin{bmatrix} b_1 \\ 0 \\ 0 \end{bmatrix} \mu_s c_2 c_{31} x_3 x_2 + \begin{bmatrix} 0 \\ b_2 \\ 0 \end{bmatrix} \Delta\omega + \begin{bmatrix} 0 \\ 0 \\ B_3 \end{bmatrix} u_3 \tag{10}$$

where,

$$x = \left[x_1 \quad x_2 \quad x_{31} \quad x_{32} \quad x_{33}\right]^T \tag{11}$$

and the output equations for the equivalence and fuel ratios using (10) can be approximated by,

$$y_{EqRatio} = \mu_S \cdot c_2 c_{31} x_2 x_3 \tag{12}$$

$$y_{FuelRatio} = \mu_S \cdot c_2 x_2 (c_{32} x_3 + .625 u_1) / \phi_{target} \tag{13}$$

For the remaining discussion, μ_S =14.6 will be used, and for a blend of gasoline and another fuel (such as ethanol) μ_S will be changed correspondently. The parameter matrices of the engine model are listed below with ω_0 = 1, where system matrices, A_3, B_3, C_3, and D_3 are obtained from state space realization of G_3, see Figure 2-2.

$$\begin{aligned} a_1 &= -25; \quad b_1 = 1; \quad c_1 = 25; \\ a_2 &= -5; \quad b_2 = -1; \quad c_2 = 5; \end{aligned}$$

$$A_3 = \begin{bmatrix} -20 & 0 & 0.46875 \\ 0 & -20 & 0 \\ 0 & 0 & -1.25 \end{bmatrix}; \quad B_3 = \begin{bmatrix} 0.625 & 0 \\ 0 & 1 \\ 1 & 0 \end{bmatrix};$$

$$C_3 = \begin{bmatrix} 20 & 20 & 0 \\ 0 & 0 & 0.46875 \end{bmatrix}; \quad D_3 = \begin{bmatrix} 0 & 0 \\ 0.625 & 0 \end{bmatrix}.$$

This control oriented model was validated with the mixed mean value and crank resolved model (calibrated with GT-Power simulation data) presented in [38] with fairly good agreement. The nonlinear state space engine model must be transformed into the *regular form* [39] below to apply sliding mode control,

$$\dot{\eta} = f_a(\eta, z) + \delta(\eta, z) \tag{14}$$

$$\dot{z} = f_b(\eta, z) + G(\eta, z)u, \tag{15}$$

where the forcing term of equation (14), $\delta(\eta,z)$, contains the disturbance input $\Delta\omega$ and $f_a(\eta,z)$ contains the nonlinear portion of (10). A change of variables,

$$\begin{bmatrix} \eta \\ z \end{bmatrix} = T \cdot x \tag{16}$$

transfers the original state vector into the regular form coordinates, where the transformation matrix T is chosen such that,

$$\eta = [x_1 \quad x_2 \quad (x_{31} - 0.625 x_{33})]^T \tag{17}$$

$$z = [x_{33} \quad x_{32}]^T \tag{18}$$

Thus, the original system (represented in the regular form) is shown in (19) and (20). It can be seen that the model contains two control inputs (u_1 and u_2) corresponding to PFI and DI fueling and one mass air flow disturbance input $\Delta\omega$.

$$\dot{\eta} = \underbrace{\begin{bmatrix} -25 & 0 & 0 \\ 0 & -5 & 0 \\ 0 & 0 & -20 \end{bmatrix} \begin{bmatrix} \eta_1 \\ \eta_2 \\ \eta_3 \end{bmatrix} + \begin{bmatrix} 0 \\ 0 \\ -11.25 \end{bmatrix} z_1 + \begin{bmatrix} 1 \\ 0 \\ 0 \end{bmatrix} h(\eta, z)}_{f_a(\eta, z)} + \underbrace{\begin{bmatrix} 0 \\ -1 \\ 0 \end{bmatrix}}_{\delta(\eta, z)} \Delta\omega \tag{19}$$

$$\dot{z} = \underbrace{\begin{bmatrix} -1.25 & 0 \\ 0 & -20 \end{bmatrix} \begin{bmatrix} z_1 \\ z_2 \end{bmatrix}}_{f_b(\eta, z)} + \underbrace{\begin{bmatrix} 1 & 0 \\ 0 & 1 \end{bmatrix}}_{G} \begin{bmatrix} u_1 \\ u_2 \end{bmatrix} \tag{20}$$

where,

$$h(\eta, z) = 1460 \eta_2 (\eta_3 + 0.625 z_1 + z_2).$$

2.2 Sliding Mode Control Strategy

Existing sliding mode A/F ratio control applications in [40] and [41] utilized the binary nature of a HEGO (Heated Exhaust Gas Oxygen) sensor to reduce oscillation resulting from the time delay by using a dynamic, one dimensional sliding surface.

Recall the control problem is to regulate both engine A/F ratio and fuel ratio (PFI fuel mass to total fuel mass) to their target levels by adjusting the PFI and DI fuel mass injection rates. Due to the nonlinear nature of the proposed A/F ratio and fueling ratio dynamics, sliding mode control was proposed for this control problem due to its robustness to matched uncertainties [39]. Thus, a two dimensional sliding surface is selected to control both equivalence and fuel ratios of the dual-fuel system. The sliding surface is defined as,

$$s = z - \varphi(\eta), \tag{21}$$

where the control objective is to regulate "s" to zero by designing a feedback $\varphi(\eta)$ such that it stabilizes equation (19). Choosing,

$$z = \varphi(\eta) = \begin{bmatrix} z_1 \\ z_2 \end{bmatrix} = \begin{bmatrix} 1.6\eta_1 \\ -\eta_1 - \eta_3 \end{bmatrix} \tag{22}$$

results in the asymptotic stability at the origin given in equation (19) and decouples the nonlinear dynamics contained in $f_a(\eta,z)$ from the remaining equation. The initial choice of (21) and consequently (22) was to linearize the system through feedback and achieve acceptable stabilization of (19). Also, note that the selection of $\varphi(\eta)$ does not contain the state η_2 and removes it from having any effect on the system, which is significant since the state η_2 contained the input disturbance, $\Delta\omega$.

The selection of the control u to cancel the known terms of the differentiation of (21) and the control input v that guarantees asymptotic stability and forces s toward zero are designed from [39], see the following,

$$u = u_{eq} + G^{-1}(\eta, z)v \text{, where } u_{eq} = G^{-1}(\eta, z)\left[-f_b(\eta, z) + \frac{\partial \varphi}{\partial \eta} f_a(\eta, z) \right] \text{and}$$
$$v = -\beta \operatorname{sgn}(s) \tag{23}$$

where β is a vector to be determined later. The resulting control forces the system states onto the sliding surface in finite time and eventually brings these states on the sliding surface to zero. To achieve the desired nonzero equivalence and fuel ratios, consider,

$$\Delta\eta = (\eta - \eta_0) = \begin{bmatrix} \eta_1 - \eta_{1_0} \\ \eta_2 - \eta_{2_0} \\ \eta_3 - \eta_{3_0} \end{bmatrix}, \quad where \quad \eta = \Delta\eta + \eta_0 \tag{24}$$

$$\Delta z = (z - z_0) = \begin{bmatrix} z_1 - z_{1_0} \\ z_2 - z_{2_0} \end{bmatrix}, \quad where \quad z = \Delta z + z_0 \tag{25}$$

where $\Delta\eta$ and Δz go to zero, leading η and z to converge to the target states η_0 and z_0 as time goes to infinity since the sliding mode controller regulates the states $\Delta\eta_1$, $\Delta\eta_3$,Δz_1, and Δz_2 to the sliding manifold s = 0. Using these target states, η_0 and z_0 can bring the equivalence and fuel ratios to any desired value. To investigate the stability of the system with these new target states, $\varphi(\eta)$ from (22) is used and the final system becomes,

$$\Delta\dot{\eta} = \begin{bmatrix} -25 & -1460(\eta_{3_0} + 0.625 z_{1_0} + z_{2_0}) & 0 \\ 0 & -5 & 0 \\ -11.25 \cdot 1.6 & 0 & -20 \end{bmatrix} \begin{bmatrix} \Delta\eta_1 \\ \Delta\eta_2 \\ \Delta\eta_3 \end{bmatrix} + \begin{bmatrix} 0 \\ -1 \\ 0 \end{bmatrix} \delta$$
$$+ \begin{bmatrix} 1460\eta_{2_0}(\eta_{3_0} + 0.625 z_{1_0} + z_{2_0}) + 25\eta_{1_0} \\ 5\eta_{2_0} \\ 20\eta_{3_0} + 11.25 z_{1_0} \end{bmatrix} \tag{26}$$

$$\Delta\dot{z} = \begin{bmatrix} -1.25 & 0 \\ 0 & -20 \end{bmatrix} \begin{bmatrix} \Delta z_1 \\ \Delta z_2 \end{bmatrix} + \begin{bmatrix} 1 & 0 \\ 0 & 1 \end{bmatrix} \begin{bmatrix} u_1 \\ u_2 \end{bmatrix} + \begin{bmatrix} 1.25 & 0 \\ 0 & 20 \end{bmatrix} \begin{bmatrix} z_{1_0} \\ z_{2_0} \end{bmatrix} \tag{27}$$

It can be seen that the system is linear with constant matrices plus the forcing δ term. For the entire system stability analysis, the characteristic equation of the composite linear system matrix A_{comp} is,

$$\det(\lambda I - A_{comp}) = (\lambda + 25)(\lambda + 5)(\lambda + 20)(\lambda + 1.25)(\lambda + 20)$$

with all eigenvalues in the left half plane, where,

$$A_{comp} = \begin{bmatrix} -25 & -1460(\eta_{3_0} + 0.625 z_{1_0} + z_{2_0}) & 0 & 0 & 0 \\ 0 & -5 & 0 & 0 & 0 \\ -11.25 \cdot 1.6 & 0 & -20 & 0 & 0 \\ 0 & 0 & 0 & -1.25 & 0 \\ 0 & 0 & 0 & 0 & -20 \end{bmatrix}.$$

Note that the target states η_0 and z_0 can be determined with the given input air disturbance and desired equivalence and fuel ratios. The following output equations are the result of coordinate transformation of (12) and (13) using (16),

$$\tilde{y}_{EqRatio} = 25\eta_1 = 5 \cdot 20 \cdot \eta_2 (\eta_3 + 0.625 z_1 + z_2) \tag{28}$$

$$\tilde{y}_{FuelRatio} = 14.6 \cdot 5 \cdot \eta_2 (0.46875 z_1 + 0.625 u_1) / \phi_{t\arg et} \tag{29}$$

Consider the state equations (19) and (20) at steady state by setting derivative terms equal to zero, leading to the system steady-state states η and z expressed as a function of the desired output ratios and input disturbance. The target states η_0 and z_0 can be obtained with given target ratios and disturbance, see below,

$$\begin{cases} \eta_{1_0} = \frac{1}{25} \tilde{y}_{EqRatio} \\ \eta_{2_0} = -\frac{1}{5} \Delta\omega \\ \eta_{3_0} = -\frac{11.25}{20} z_{1_0} \end{cases} \tag{30}$$

and,

$$\begin{cases} z_{1_0} = \dfrac{\tilde{y}_{FuelRatio} \cdot \phi_{t\arg et}}{14.6 \cdot 5 \cdot \eta_{2_0} (0.46875 + 0.625 \cdot 1.25)} \\ z_{2_0} = \dfrac{25\eta_{1_0}}{14.6 \cdot 5 \cdot 20 \cdot \eta_{2_0}} - \eta_{3_0} - 0.625 z_{1_0} \end{cases} \tag{31}$$

The zero target state sliding mode control strategy is modified such that the closed-loop system converges to the desired target states, see Figure 2-3.

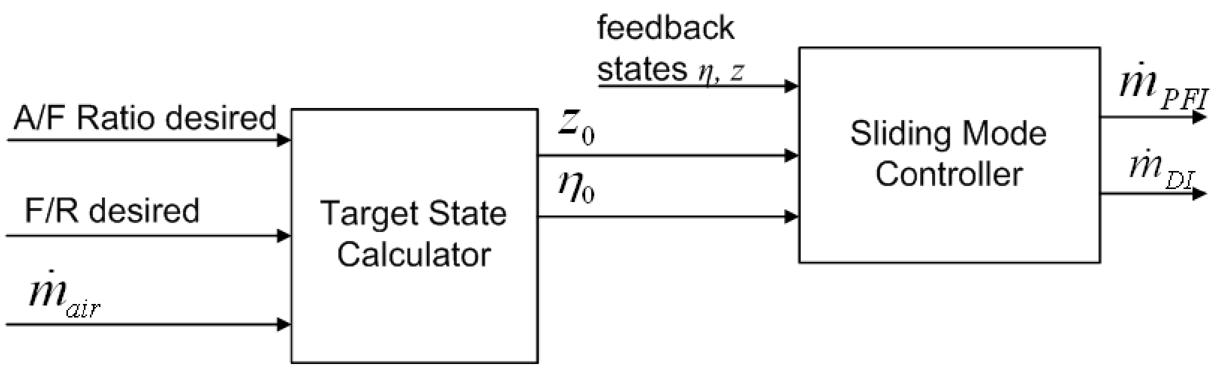

Figure 2-3: Schematic diagram of sliding mode control strategy

To improve the performance of the sliding mode controller, the stabilizing function $\varphi(\eta)$ was generalized as follows,

$$z = \varphi(\Delta\eta) = \begin{bmatrix} 1.6\Delta\eta_1 + \varepsilon\Delta\eta_3 \\ -\Delta\eta_1 - \Delta\eta_3 \end{bmatrix} \tag{32}$$

where ε is a positive constant. Substituting (32) into (19) yields,

$$\Delta\dot{\eta} = \begin{bmatrix} \text{-}25 & 0 & 0 \\ 0 & \text{-}5 & 0 \\ \text{-}11.25\cdot 1.6 & 0 & \text{-}20\text{-}11.25\varepsilon \end{bmatrix} \begin{bmatrix} \Delta\eta_1 \\ \Delta\eta_2 \\ \Delta\eta_3 \end{bmatrix} + \begin{bmatrix} d\Delta\eta_2 \\ 0 \\ 0 \end{bmatrix} \Delta\eta_3\varepsilon \tag{33}$$

where d = 91.25. Note that equation (33) is in the following form,

$$\Delta\dot{\eta} = A(\varepsilon)\Delta\eta + g(\Delta\eta, \varepsilon) \tag{34}$$

where,

$$A(\varepsilon) = \begin{bmatrix} \text{-}25 & 0 & 0 \\ 0 & \text{-}5 & 0 \\ \text{-}11.25\cdot 1.6 & 0 & \text{-}20\text{-}11.25\varepsilon \end{bmatrix}, \quad g(\Delta\eta, \varepsilon) = \begin{bmatrix} d\Delta\eta_2 \\ 0 \\ 0 \end{bmatrix} \Delta\eta_3\varepsilon.$$

It can been seen that $A(\varepsilon)$ is Hurwitz if $\varepsilon > 0$ and also,

$$\left\| \begin{bmatrix} d\Delta\eta_2 \\ 0 \\ 0 \end{bmatrix} \Delta\eta_3\varepsilon \right\|_2 \leq d\,\|\varepsilon\|_2\,\|\Delta\eta\|_2^2. \tag{35}$$

Let $Q = I$ and define $X(\varepsilon) > 0$ as the solution of the Lyapunov equation assuming $\varepsilon > 0$,

$$A^T(\varepsilon)X(\varepsilon) + X(\varepsilon)A(\varepsilon) = -Q.$$

The maximum and minimum eigenvalues of $X(\varepsilon)$ are plotted as function of ε in Figure 2-4. Define the Lyapunov function $V(\Delta\eta) = \Delta\eta^T X(\varepsilon)\Delta\eta$, leading to the following properties,

$$\begin{gathered} \lambda_{\min}(X(\varepsilon))\|\Delta\eta\|_2^2 \leq V(\Delta\eta) \leq \lambda_{\max}(X(\varepsilon))\|\Delta\eta\|_2^2, \\ \frac{\partial V}{\partial\Delta\eta} A\Delta\eta = \text{-}\Delta\eta^T Q\Delta\eta \leq \text{-}\lambda_{\min}(Q)\|\Delta\eta\|_2^2, \\ \left\| \frac{\partial V}{\partial\Delta\eta} \right\| = \left\| 2\Delta\eta^T X \right\|_2 \leq 2\|X\|_2\,\|\Delta\eta\|_2 = 2\lambda_{\max}(X)\,\|\Delta\eta\|_2. \end{gathered} \tag{36}$$

The derivative of $V(\Delta\eta)$ satisfies,

$$\dot{V}(\Delta\eta) = \Delta\eta^T (A^T(\varepsilon)X(\varepsilon) + X(\varepsilon)A(\varepsilon))\Delta\eta + 2\varepsilon d\Delta\eta_3 \begin{bmatrix} \Delta\eta_2 \\ 0 \\ 0 \end{bmatrix}^T X(\varepsilon)\Delta\eta$$
$$\leq -\lambda_{\min}(Q)\|\Delta\eta\|_2^2 + 2\lambda_{\max}(X(\varepsilon))\varepsilon d\,|\Delta\eta_3|\cdot\|\Delta\eta\|_2^2. \tag{37}$$

Note that the origin is exponentially stable if the derivative of $V(\Delta\eta)$ is negative. Therefore the system is exponentially stable if,

$$\varepsilon < \frac{1}{2\lambda_{\max}(X(\varepsilon))d\,|\Delta\eta_3|}. \tag{38}$$

The stability condition will hold assuming,

$$|\Delta\eta_3| = |\eta_3 - \eta_{3_0}| \leq \gamma \tag{39}$$

for all time, where γ is a positive constant, and can be restated as,

$$\varepsilon < \frac{1}{2\lambda_{\max}(X(\varepsilon))d\cdot\gamma} \tag{40}$$

Figure 2-4 shows that $\lambda_{\max}(X(\varepsilon)) = 0.1$ for all $\varepsilon > 0$, thus,

$$\varepsilon < \frac{1}{2\cdot 0.1\cdot d\cdot\gamma} < \frac{1}{2\cdot 0.1\cdot 1460\cdot 0.625\cdot\gamma} = \frac{1}{182.5\cdot\gamma} \tag{41}$$

Equation (41) shows that if γ is greater than zero, then there exists an $\varepsilon > 0$ with guaranteed stability.

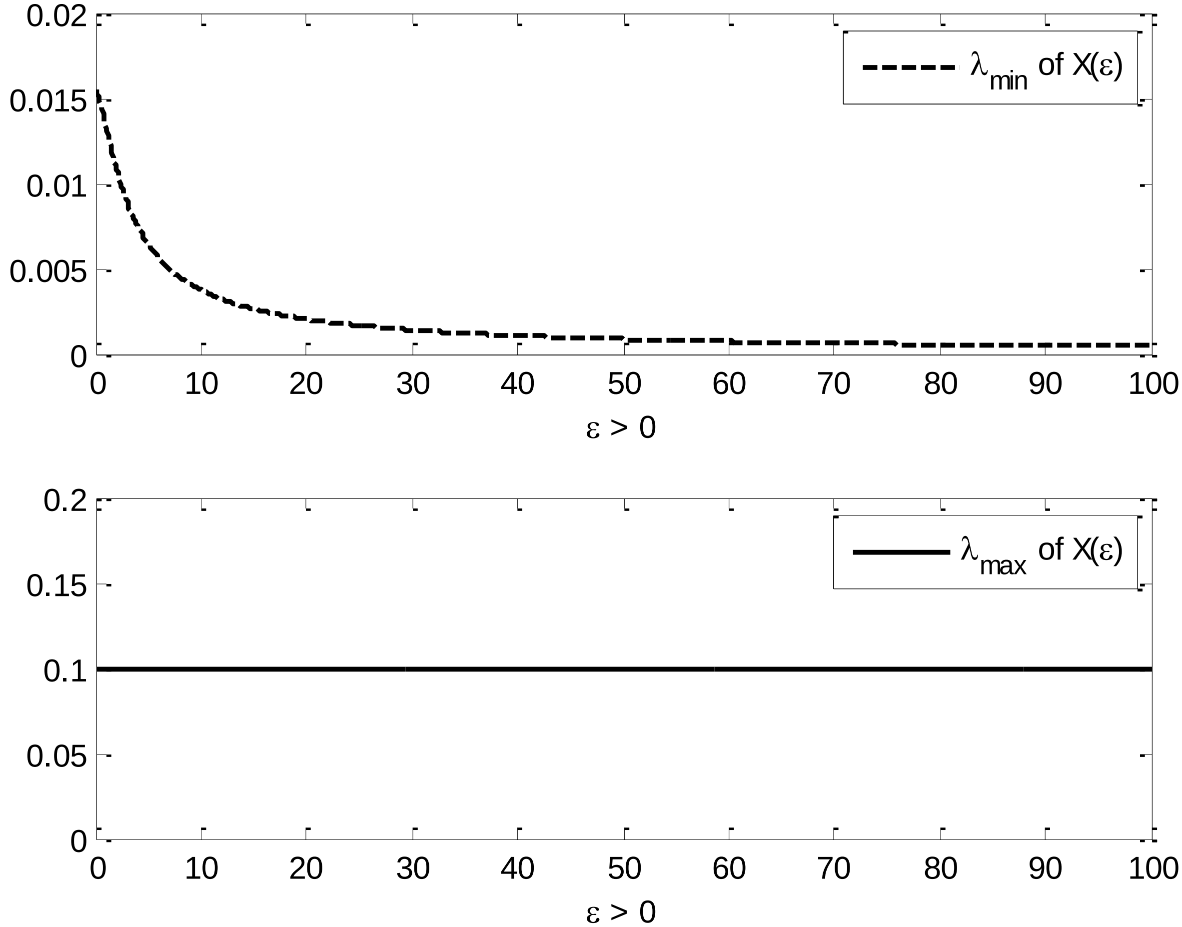

Figure 2-4: Maximum and minimum eigenvalues of $X(\varepsilon)$

2.3 State Feedback Simulation Results

2.3.1 Baseline PID Controller

A MIMO PID controller was designed in order to compare to the nonlinear MIMO sliding mode controller, see Figure 2-5. Since the equivalence ratio and fuel ratio are the two feedback signals, two controllers are cascaded together to the PFI and DI inputs. The first is a PID controller that corrects the error between the desired and measured equivalence ratios, in which the equivalence ratio signal is decoupled into the PFI and DI outputs. The second controller is a PI controller that corrects the fuel ratio error, in which the fuel ratio error is multiplied by the PFI signal from the output of the first PID controller. The controller gains for both PID and PI controllers are shown in Table 2-1. Note that the PID controllers 1 and 2 have the same gains listed in Table 2-1.

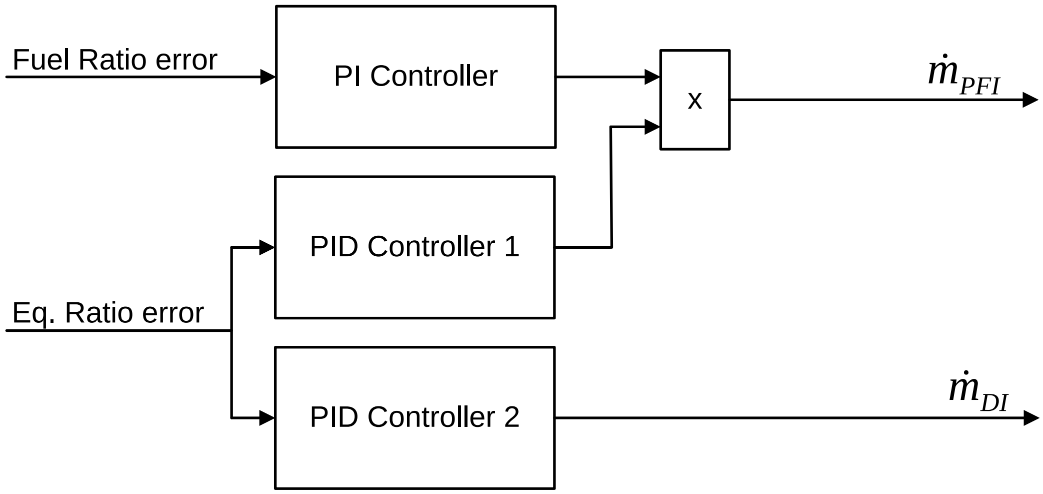

Figure 2-5: Schematic diagram of PID controller

All PID controller gains parameters were tuned such that the closed-loop system is stable and the equivalence ratio and fuel ratio responses are as fast as possible with reasonable overshoots. The derivative and proportional gains in equivalence ratio controller were first tuned to reduce the transient response time with good stability while the integration gain was set to zero. Next, the integration gain was tuned to reduce the steady state error, and finally the proportional gain was tuned again to optimize the system performance. The same process was repeated for the fuel ratio controller. Simulations of the sliding mode controller under different air flow input disturbances were conducted and compared to the PID controller.

$K_{p1} = K_{p2}$	0.000005	K_p	0.5
$K_{i1} = K_{i2}$	0.3	K_i	5
$K_{d1} = K_{d2}$	0.0207		

Table 2-1: PID and PI controller parameters

2.3.2 Simulation 1

The gain matrix β in the sliding mode controller for each simulation was tuned such that the transient response was acceptable and it was selected as,

$$\beta = \begin{bmatrix} 1.6 & 0 \\ 0 & 1.7 \end{bmatrix}. \tag{42}$$

A unitary target equivalence ratio and 60% (0.6) target fuel ratio were chosen for each simulation. Figure 2-6 shows the closed-loop response of the PID controller and sliding mode controller for Simulation #1. The simulation uses a constant input disturbance $\Delta\omega$ of 0.1 plus 5 percent noise, adding a step input of 0.15 to the constant disturbance at the 6th second. It also has a fuel ratio reduction from 0.6 to 0.4 at the 9th second, and shows that the controller rejects the disturbance quickly. Figure 2-6 also shows the PFI and DI fuel control inputs for both PID and sliding mode controllers. It can be observed that the sliding mode controller provides quick fueling inputs of both PFI and DI systems, leading to better disturbance rejection and transient response over the PID responses. Table 2-2 summarizes the overshoot and settling time for both PID and sliding mode controllers.

	% Overshoot (after 6th second)		Settling Time (after 9th second)		Steady State Error (after 12th second)	
	PID	Sliding	PID	Sliding	PID	Sliding
Eq. Ratio	5.19%	2.44%	1.6 (sec)	< 0.5 (sec)	0.016	0.0003
Fuel Ratio	2.30%	2.61%	3.29 (sec)	2.31 (sec)	0.033	0.0003

Table 2-2: Comparison of controllers for Simulation #1

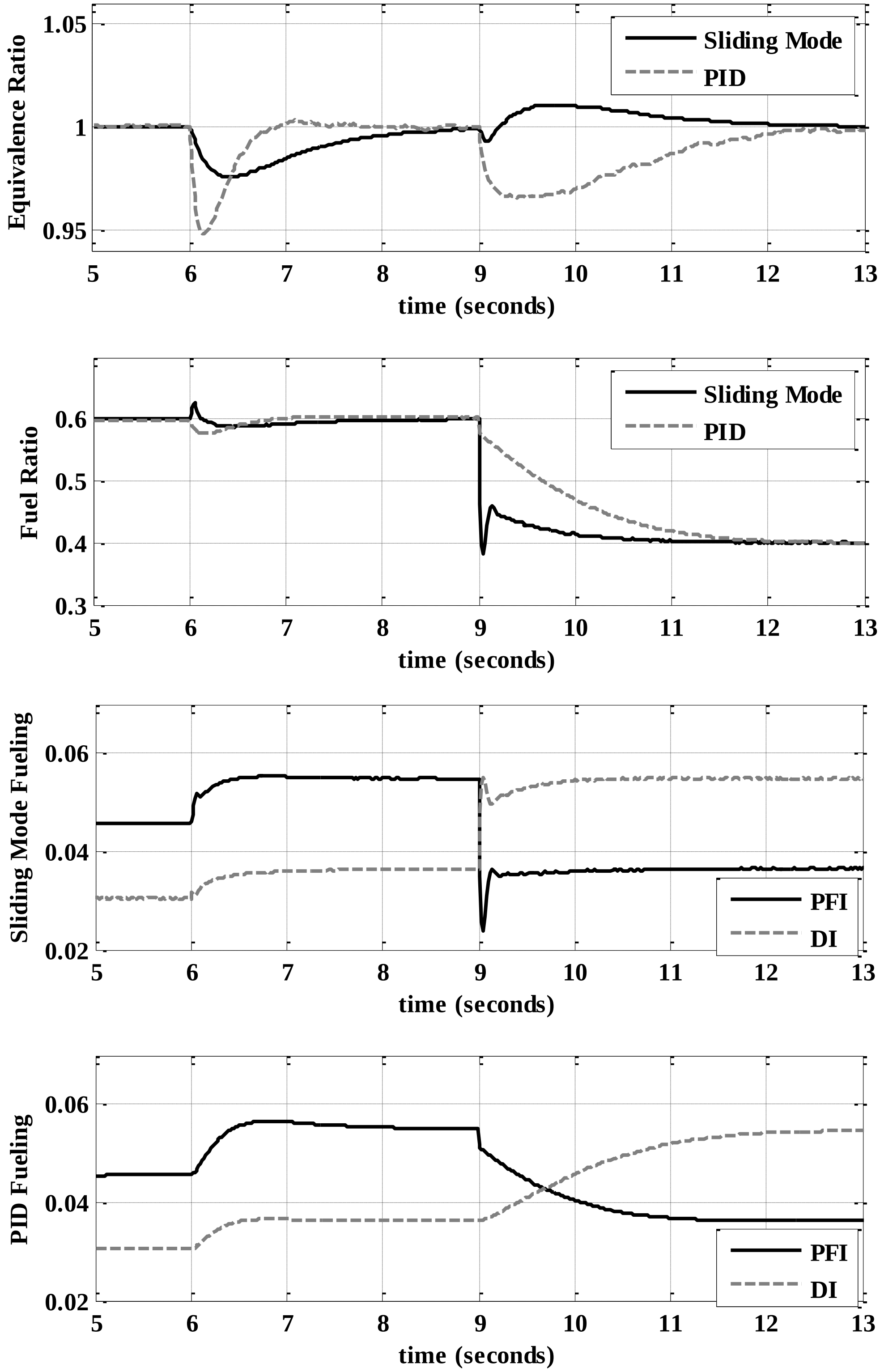

Figure 2-6: Closed loop response of simulation #1

2.3.3 Simulation 2

Figure 2-7 shows the closed-loop response of both PID and sliding mode controllers for Simulation #2. This simulation decreases the target equivalence ratio from 1 to 0.9 at the 6th second, and increases it back to unity at the 9th second. Again, the constant input disturbance $\Delta\omega$ was 0.1 plus 5 percent noise. Figure 2-7 also displays both fueling inputs of PID and sliding mode controllers.

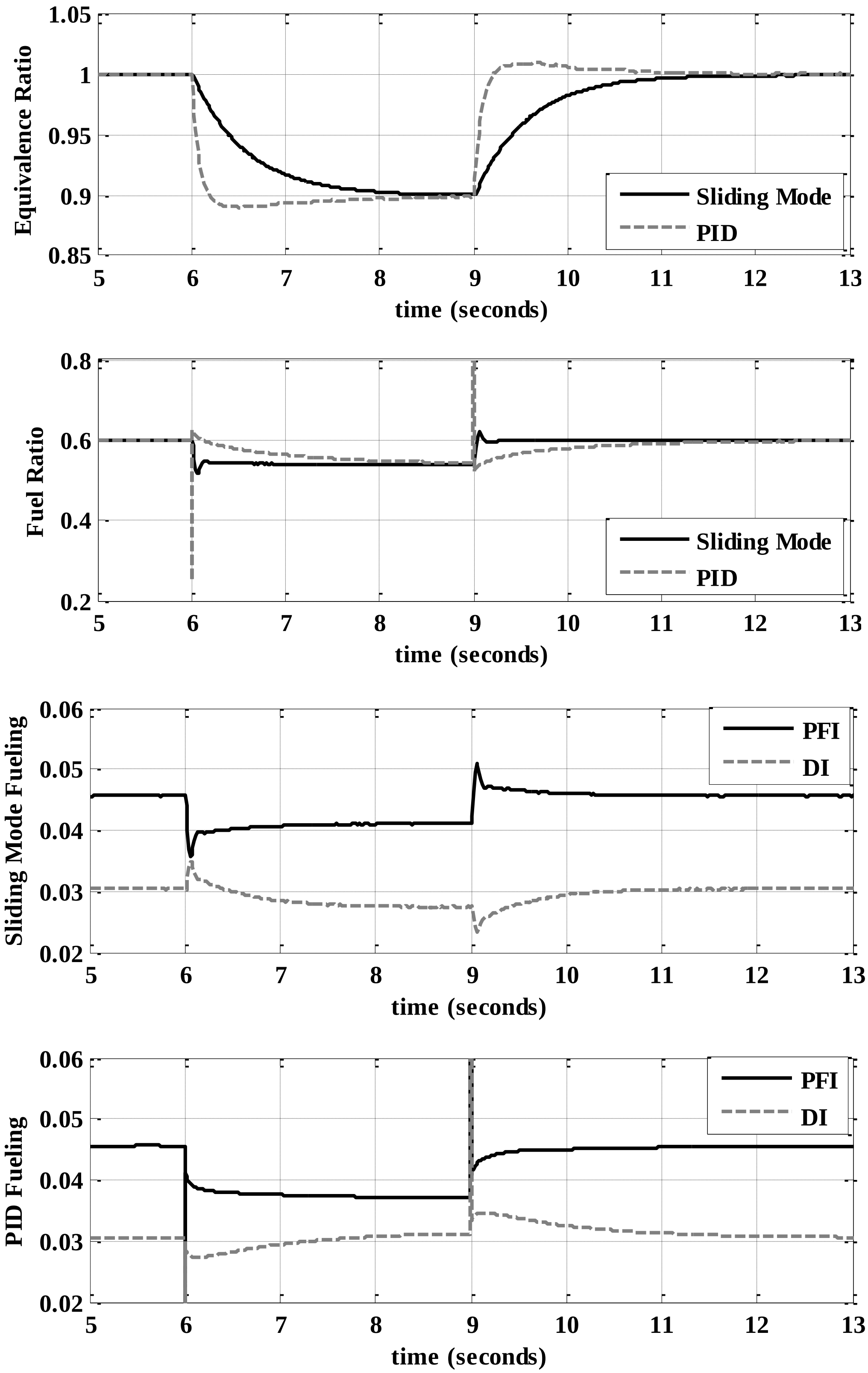

Figure 2-7: Closed loop response of simulation #2

Although the PID controller has a faster equivalence ratio response than the sliding mode one, it is under the penalty of the fuel ratio control accuracy (huge overshoot (29%) during the transition). On the other hand, the sliding mode controller provides smooth transitions for both equivalence and fuel ratios. Therefore, the sliding mode control responses are more favorable over the PID ones. Table 2-3 summarizes the overshoot and settling time for both PID and sliding mode controllers for Simulation #2. It is worth noting the 29% fuel ratio overshoot for the PID controller while the sliding mode controller only has 2.27% overshoot.

	% Overshoot (after 6^{th} second)		Settling Time (after 9^{th} second)		Steady State Error (after 12^{th} second)	
	PID	Sliding	PID	Sliding	PID	Sliding
Eq. Ratio	0.99%	0.05%	0.45 (sec)	1.29 (sec)	0.0018	0.0007
Fuel Ratio	29%	2.27%	1.53 (sec)	< 0.1 (sec)	0.0042	0.0005

Table 2-3: Comparison of controllers for Simulation #2

Simulation 3

Figure 2-8 shows the closed-loop response of both PID and sliding mode controllers for Simulation #3. This simulation has an air flow disturbance of zero and ω_0 is equal to unity, which constitutes the wide open throttle (WOT) case. The simulation decreases the target fuel ratio from 0.5 to zero (100% DI fueling). Since the engine speed is fixed, WOT implies high engine load, and the simulation shows that complete direct injection fueling can be achieved by the controller, and therefore can be used to suppress engine knock at high engine load.

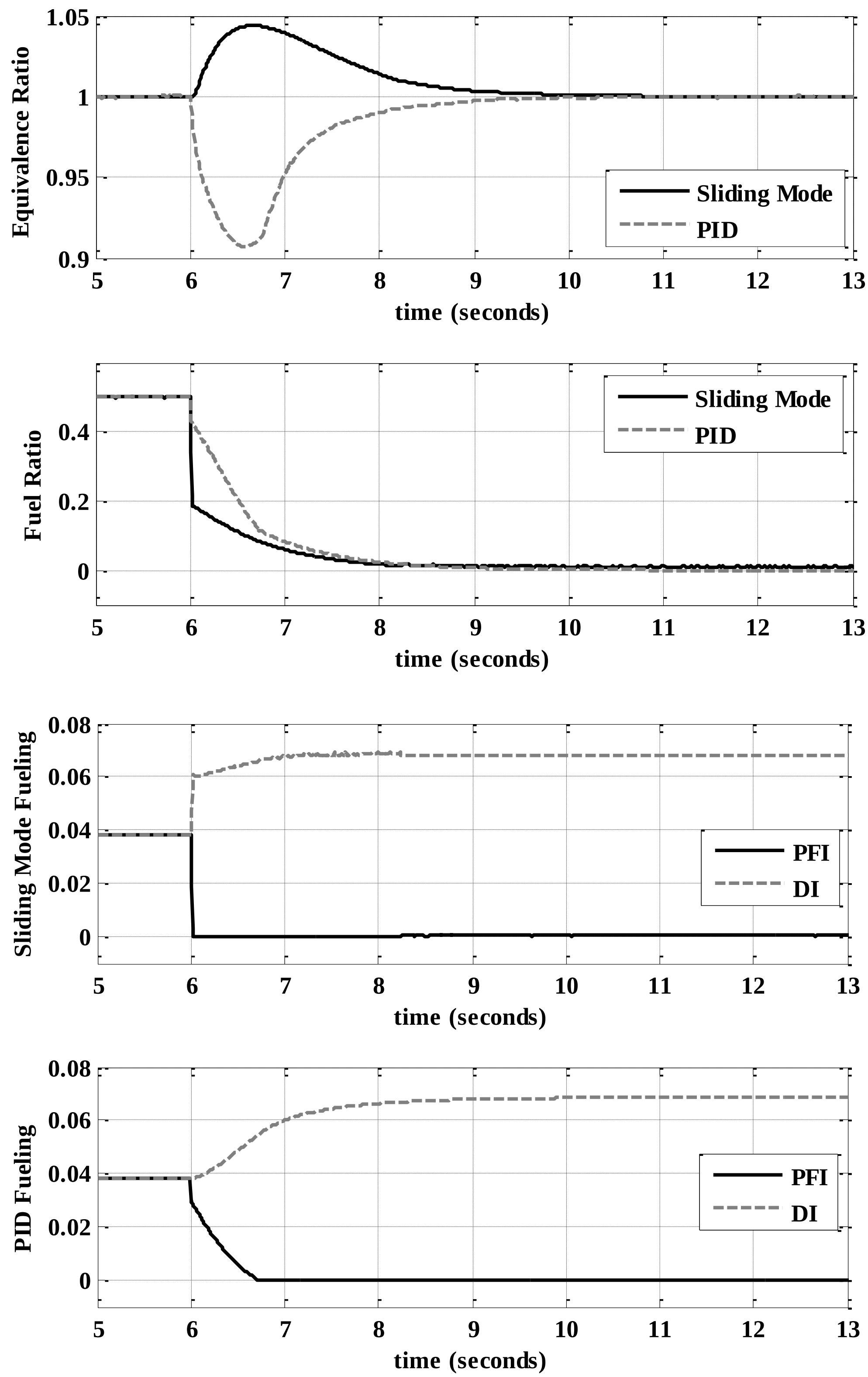

Figure 2-8: Closed loop response of simulation #3

Note that all simulations conducted in this section use the continuous ODE3 solver in Simulink.

2.4 State Estimator Design

The sliding mode control strategy was implemented using state feedback, but not all state information will be available for closed loop control since in practice only limited sensors are available to measure certain states/outputs. In some cases, even though these states are measurable, the cost limitations prohibit utilizing state feedback. Therefore, to implement the sliding mode control scheme, a state estimator must be designed to obtain state information in real-time from the available measurements. These measurements are the equivalence and fuel ratio outputs, and the PFI and DI fueling inputs. The equivalence ratio can be measured by a UEGO (universal exhaust gas oxygen) sensor; and the fuel ratio can be estimated using a virtual sensor technology that combines UEGO signal, DI fueling quantity (estimated based upon the fuel pressure and injection pulse width), and measured mass air flow rate. Therefore, for state estimation, it was assumed that system control inputs (PFI and DI fueling), outputs (equivalence and fuel ratios), and mass air flow rate variation $\Delta\omega$ are measurable.

The fuel ratio estimation also works with the case where two different fuels are used for DI and PFI, for example, gasoline for PFI and ethanol for DI. Assuming that $\dot{m}_{\mathrm{DI}}$ in (5) can be estimated from fuel injection duration and pressure, PFI effective fueling $\dot{m}_{\mathrm{PFI\_E}}$ in (5) is required for estimating fuel ratio. The overall equivalence ratio can be expressed below,

$$\phi = \frac{\dot{m}_{DI}}{\dot{m}_{air}}\mu_{DI} + \frac{\dot{m}_{PFI\_E}}{\dot{m}_{air}}\mu_{PFI} \tag{43}$$

where ϕ can be estimated from the oxygen sensor, $\dot{m}_{\mathrm{air}}$ can be estimated from the mass-air-flow sensor, and μ_{DI} and μ_{PFI} are stoichiometry air-to-fuel ratios for DI fuel and PFI fuel, respectively. Therefore, PFI effective fueling $\dot{m}_{\mathrm{PFI\_E}}$ can be estimated as well as the fuel ratio.

Consider the nonlinear system described in equations (10), (12), and (13). Since state x_2 can be estimated from the mass air flow sensor signal $\Delta\omega$ equipped on the engine, and thus assuming that x_2 is known, the system can be rewritten as,

$$\dot{\tilde{x}} = \begin{bmatrix} -25 & 1460x_2 & 1460x_2 & 0 \\ 0 & -20 & 0 & 0.46875 \\ 0 & 0 & -20 & 0 \\ 0 & 0 & 0 & -1.25 \end{bmatrix} \tilde{x} + \begin{bmatrix} 0 & 0 \\ 0.625 & 0 \\ 0 & 1 \\ 1 & 0 \end{bmatrix} u = A_S \tilde{x} + B_S u \tag{44}$$

$$\tilde{y} = \begin{bmatrix} 25 & 0 & 0 & 0 \\ 0 & 0 & 0 & 34.21875x_2 / \phi_{target} \end{bmatrix} \tilde{x} + \begin{bmatrix} 0 & 0 \\ 45.625x_2 / \phi_{target} & 0 \end{bmatrix} u = C_S \tilde{x} + D_S u \tag{45}$$

where $\tilde{x} = [x_1 \quad x_{31} \quad x_{32} \quad x_{33}]^T$ The system is now in a linear parameter variation (LPV) system form. Also, note that the time varying system is not observable since when x_2 is zero, states 2 and 3 of (44) and (45) cannot be reconstructed from the output. Through the *Luenberger state observer* design [42], it will be shown that the proposed observer error reduces to zero asymptotically. The state estimator has the following form,

$$\begin{aligned} \dot{\hat{x}} &= A_S \hat{x} + B_S u + L(\tilde{y} - \hat{y}) \\ \hat{y} &= C_S \hat{x} + D_S u \end{aligned} \tag{46}$$

where matrix L is a function of both x_2 and ϕ_{target} such that the estimation error goes to zero as time goes to infinity. The estimation system equation can also be rewritten as,

$$\begin{aligned} \dot{\hat{x}} &= (A_S - LC_S)\hat{x} + \begin{bmatrix} B_S - LD_S & L \end{bmatrix} \begin{bmatrix} u \\ \tilde{y} \end{bmatrix} \\ \hat{y} &= C_S \hat{x} + D_S u \end{aligned} \tag{47}$$

and the error between the actual state $\tilde{x}(t)$ and the estimated state $\hat{x}(t)$ is governed by the following equation,

$$\dot{e}(t) = \dot{\tilde{x}}(t) - \dot{\hat{x}}(t) = A_S\tilde{x} + B_S u - (A_S - LC_S)\hat{x} - \begin{bmatrix} B_S - LD_S & L \end{bmatrix}\begin{bmatrix} u \\ \tilde{y} \end{bmatrix}$$
$$= (A_S - LC_S)(\tilde{x} - \hat{x}) = (A_S - LC_S)e(t). \tag{48}$$

By choosing the estimation gain matrix L as a function of both x_2 and ϕ_{target},

$$L^T(x_2, \phi_{target}) = \begin{bmatrix} 19 & 0 & 0 & 0 \\ 0 & \dfrac{0.46875 \cdot \phi_{target}}{34.21875 x_2} & 0 & \dfrac{48.75 \cdot \phi_{target}}{34.21875 x_2} \end{bmatrix}, \tag{49}$$

the error system matrix becomes,

$$\bar{A}(x_2) = A_S - LC_S = \begin{bmatrix} -500 & 1460x_2 & 1460x_2 & 0 \\ 0 & -20 & 0 & 0 \\ 0 & 0 & -20 & 0 \\ 0 & 0 & 0 & -50 \end{bmatrix}. \tag{50}$$

The stability of $\bar{A}$ when x_2 is a constant is guaranteed since its eigenvalues have negative real parts. Since x_2 varies as a function of time, the stability of $\bar{A}(x_2)$ cannot be determined by the location of its eigenvalues. To investigate the stability of the LPV error system in (48), for a given range of x_2, $\bar{A}$ can be rewritten as,

$$\bar{A}(x_2(t)) = \alpha_1 A_1 + \alpha_2 A_2 \tag{51}$$

where,

$$\alpha_1 \geq 0, \alpha_2 \geq 0, \alpha_1 + \alpha_2 = 1 \tag{52}$$

The error system in (48) is now in the polytopic form [43] and it is quadratically stable if there exists fixed $P = P^T > 0$ such that for all x_2 [44],

$$\bar{A}^T P + P\bar{A} < 0 \tag{53}$$

and furthermore (53) is equivalent to,

$$\bar{A}^T P + P\bar{A} = \left(\alpha_1 A_1^T + \alpha_2 A_2^T\right)P + P\left(\alpha_1 A_1 + \alpha_2 A_2\right) < 0. \tag{54}$$

Define,

$$A_0 = \begin{bmatrix} -500 & 0 & 0 & 0 \\ 0 & -20 & 0 & 0 \\ 0 & 0 & -20 & 0 \\ 0 & 0 & 0 & -50 \end{bmatrix} \text{ and } \Delta A = \begin{bmatrix} 0 & 1460 & 1460 & 0 \\ 0 & 0 & 0 & 0 \\ 0 & 0 & 0 & 0 \\ 0 & 0 & 0 & 0 \end{bmatrix} \tag{55}$$

Let,

$$A_1 = A_0 + \gamma\Delta A \text{ and } A_2 = A_0 - \gamma\Delta A, \quad \gamma = 0.2 \tag{56}$$

that allows x_2 to vary between -0.2 and 0.2. Choosing,

$$P = \begin{bmatrix} 0.01 & 0.001 & 0.001 & 0 \\ 0.001 & 0.25 & 0 & 0 \\ 0.001 & 0 & 0.25 & 0 \\ 0 & 0 & 0 & 0.1 \end{bmatrix} > 0 \tag{57}$$

which satisfies (54), guarantees that the LPV error system in (48) is stable for any x_2 between -0.2 and 0.2. As a result,

$$\lim_{t\to\infty} \left\| \dot{\tilde{x}}(t) - \dot{\hat{x}}(t) \right\| = 0, \ \forall\ x_2 \in [-0.2, \quad 0.2]. \tag{58}$$

Since the separation theory does not apply for this nonlinear case, the closed loop system stability using the sliding mode controller with the state estimator is not guaranteed. Figure 2-9 shows the comparison of the estimated states constructed by the state estimator in (48) with the actual states used to achieve the desired target equivalence and fuel ratios. Note that the states are shown after the state transformation described in (17) and (18).

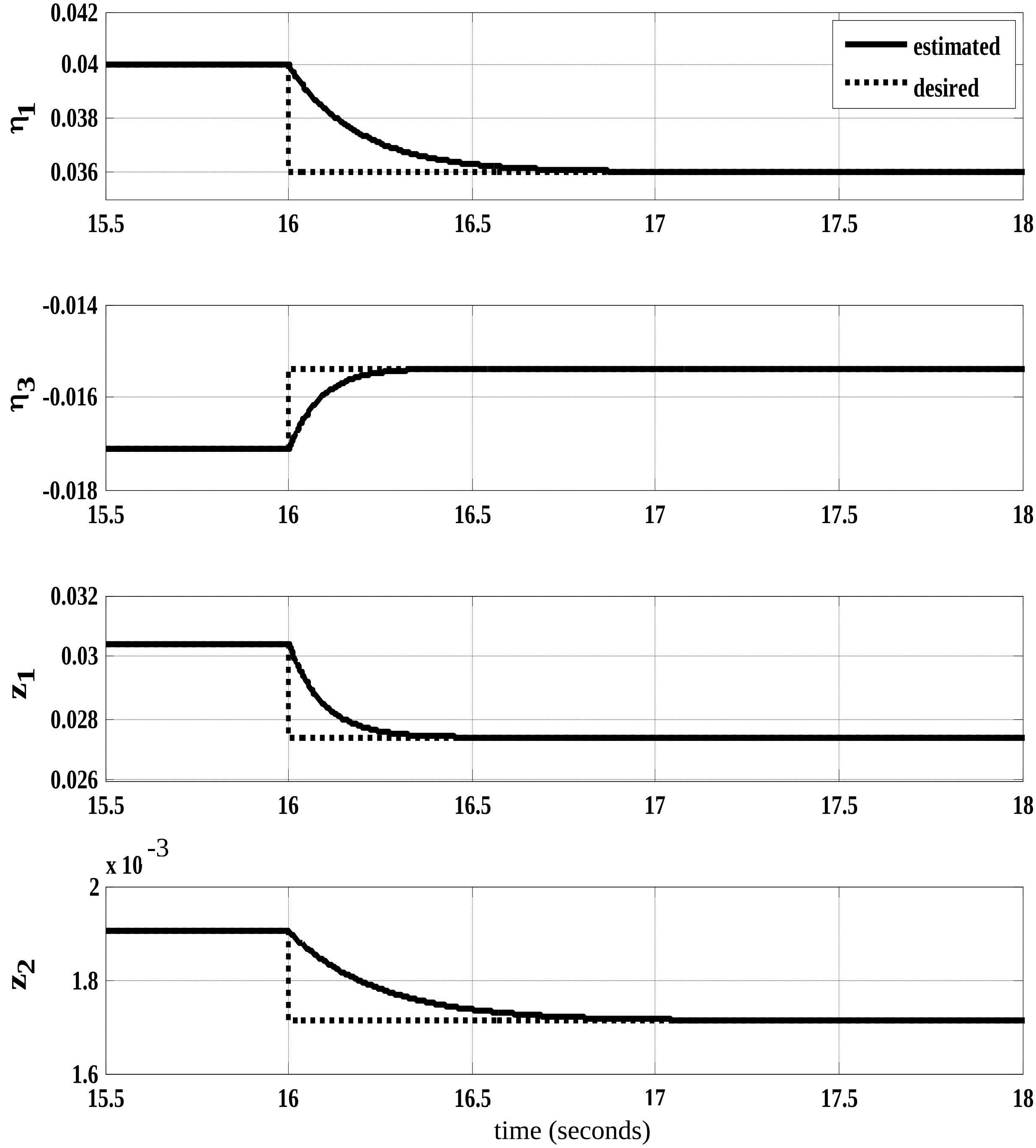

Figure 2-9: Comparison of state estimation and actual states in HIL simulation

2.5 Hardware-In-The-Loop Simulation Results

The engine model used for the HIL simulation was a control oriented 1.2L three-cylinder engine with dual-stage turbochargers mixed mean-value and crank angle based engine model developed based upon [45], see Yang and Zhu [38]. The modeled engine is also equipped with dual fuel injection systems (port fuel injection and direct injection), and can be operated with any blend of ethanol and gasoline. The engine air flow dynamics were modeled using mean value techniques described in [45]; the engine fueling and torque were updated after the corresponding cylinder top dead center (TDC); and the in-cylinder combustion process is modeled using a crank resolved approach (see [38]), where both in-cylinder temperature and pressure are modeled based upon the Wiebe function. The developed real-time engine model was implemented in an Opal-RT based HIL simulator which is to be used in this study. The subsystems from this model that were used in this study had a structure similar to Figure 2-2.

The mixed mean value engine model was implemented in MATLAB/Simulink and auto-coded into an Opal-RT based HIL simulation system [46]. The engine model was executed in the Opal-RT HIL simulator with a sample period of 1 millisecond. Similarly, the continuous time sliding mode controller, along with its state estimator, was discretized with a five-millisecond sample period (T = 0.005 second) and implemented in Simulink. The discrete Simulink controller and state estimator were then implemented into a production Mototron Engine Control Module (ECU) sampled every 5 ms [47]. The Opal-RT HIL simulator communicates with the Mototron ECU through the high speed controller-area network (CAN), where signals were sent and received with minimal delay. The HIL simulation scheme is shown in Figure 2-10.

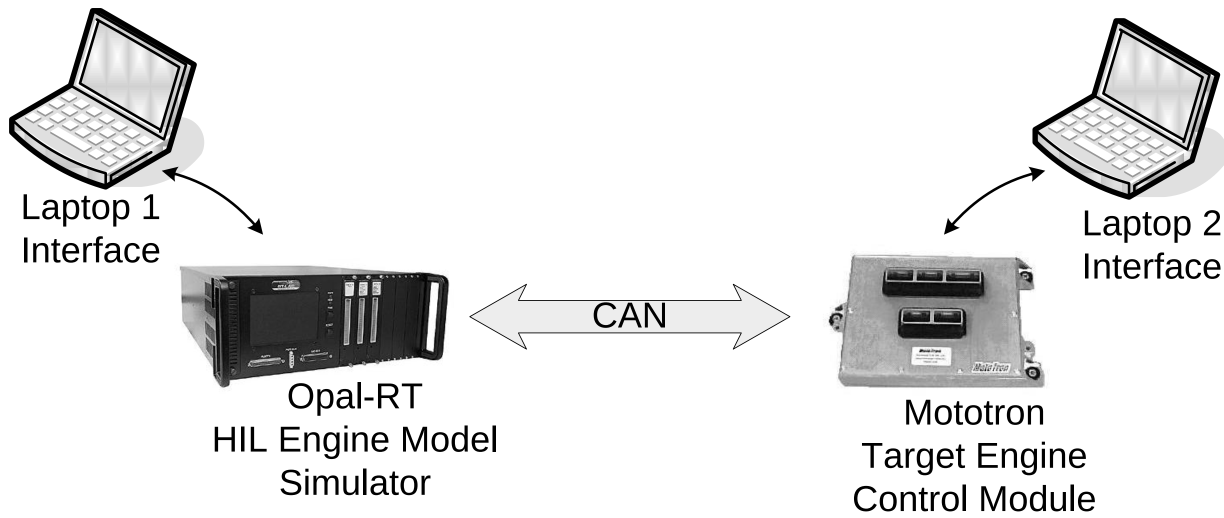

Figure 2-10: HIL simulation setup

The Opal-RT simulation step size of 1 millisecond was chosen in order to emulate a real-world continuous time engine system, while the Mototron controller sampling period of 5 ms was close to that of many production engine control systems. The CAN communication between Opal-RT and Mototron had a time delay between the time when signals were sent from Mototron and the time when these signals were received by Opal-RT, and vice versa. Furthermore, the total delay which includes the model/controller timing synchronization delays, the delay from when signals were sent from the model to the controller, controller computation, and the delay from signals sent from the controller back the model, was found to be approximately 8 ms. This delay is acceptable for the current setup since one engine cycle at 1500RPM is 80 ms. The timing scheme is shown in Figure 2-11. Also in the HIL simulation, the gain β defined in (42) was tuned for minimal settling time without oscillation. Figure 2-12 shows the responses of the equivalence and fuel ratios for different β values. It turns out that when $\beta_{HIL} = 0.4\beta$, the HIL simulation provides the best response for the discretized sliding mode controller.

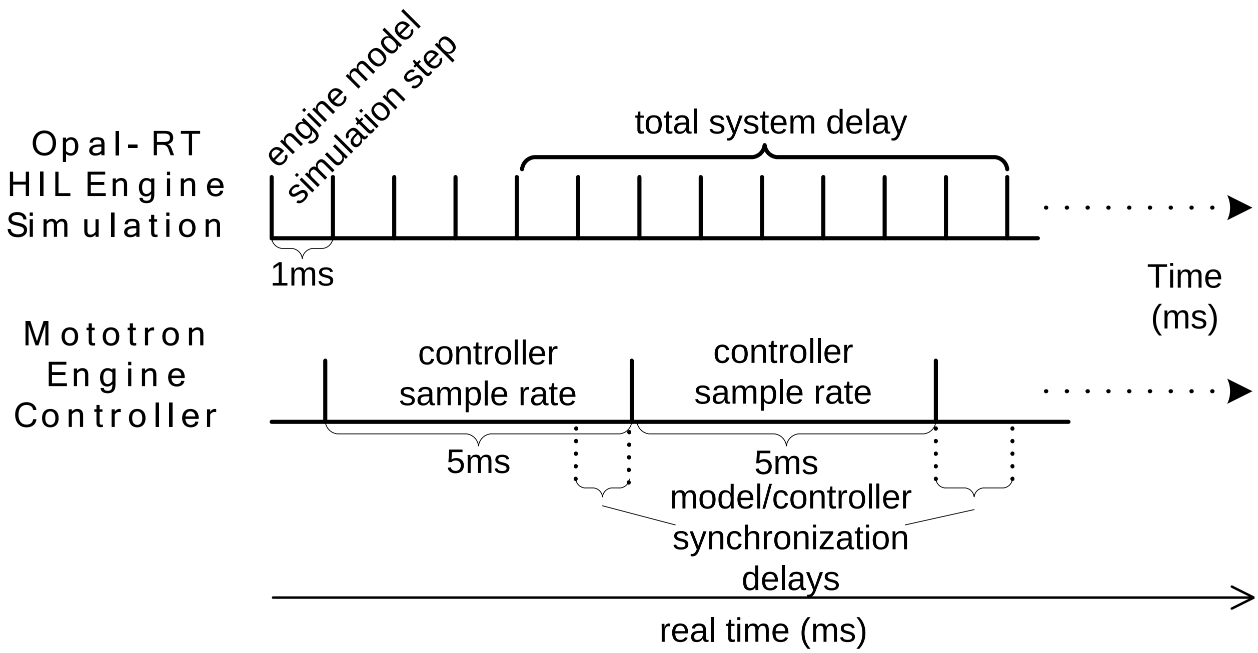

Figure 2-11: HIL timing scheme

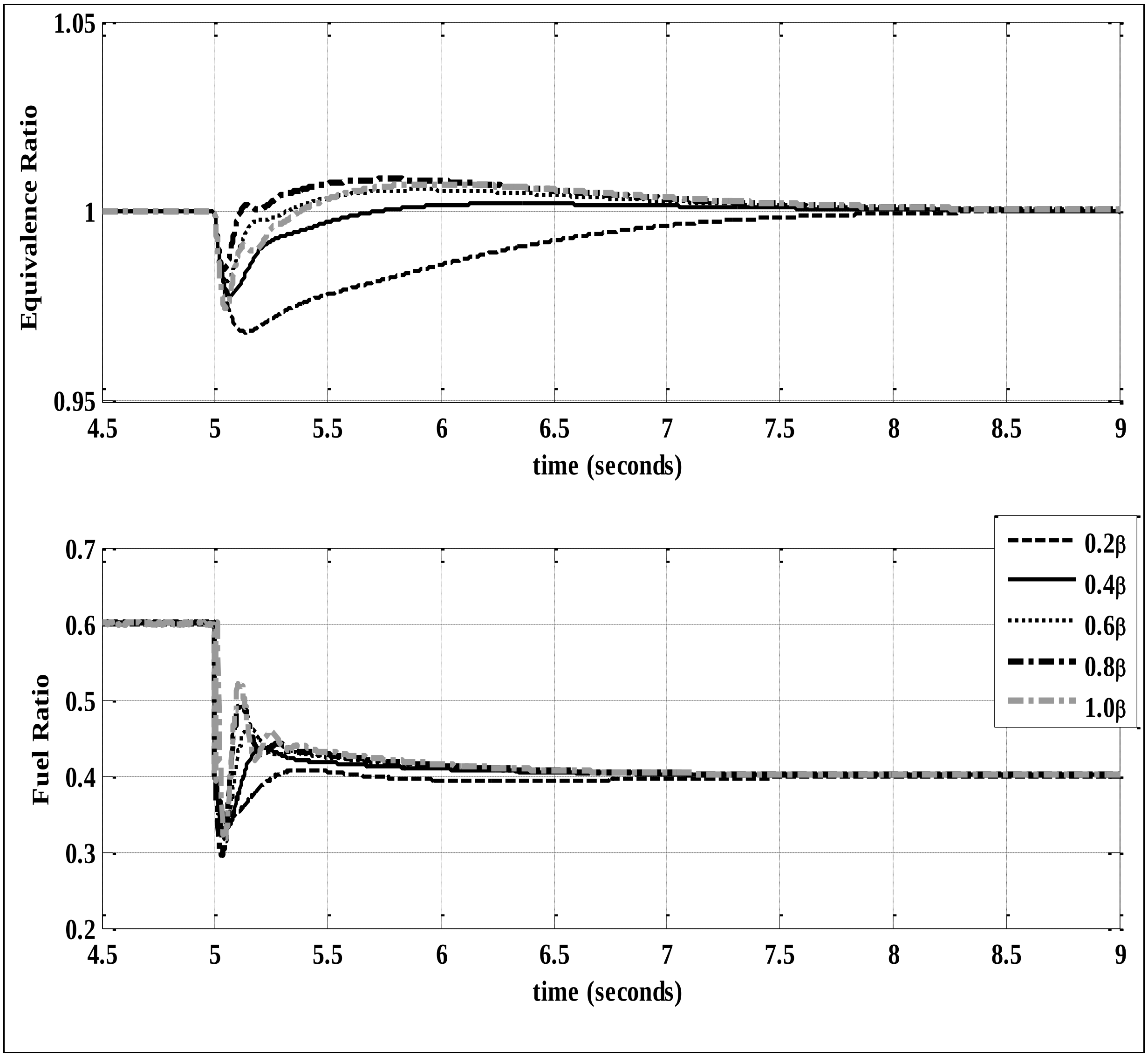

Figure 2-12: Response of ratios for different β

2.5.1 Simulation 1

For the HIL simulation 1, a fixed engine speed of 1500 RPM along with a fixed throttle opening of 90% was used throughout the entire simulation. The air flow disturbance $\Delta\omega$ was measured, resulting in the estimate of the state x_2. A unitary target equivalence ratio and 60% (0.6) target fuel ratio were chosen for the simulation. The equivalence ratio and fuel ratio HIL responses of the mean value engine model and the equivalence and fuel ratio model simulations are shown in Figure 2-13, which shows a step fuel ratio reduction from 0.6 to 0.4 at the 10th second. Figure 2-13 also shows the pure simulation response of the mean value engine model. It can be observed that the fuel ratio response for the mean value model in HIL has very minimal overshoot compared with the other output responses. Although the sliding mode controller gain of 0.4β was used for all three simulations, their responses are slightly different which is due to the feedback and control time delays between the HIL simulator and engine sliding mode controller. The tuning of β for each model in its simulation setup is important in determining its acceptable output response.

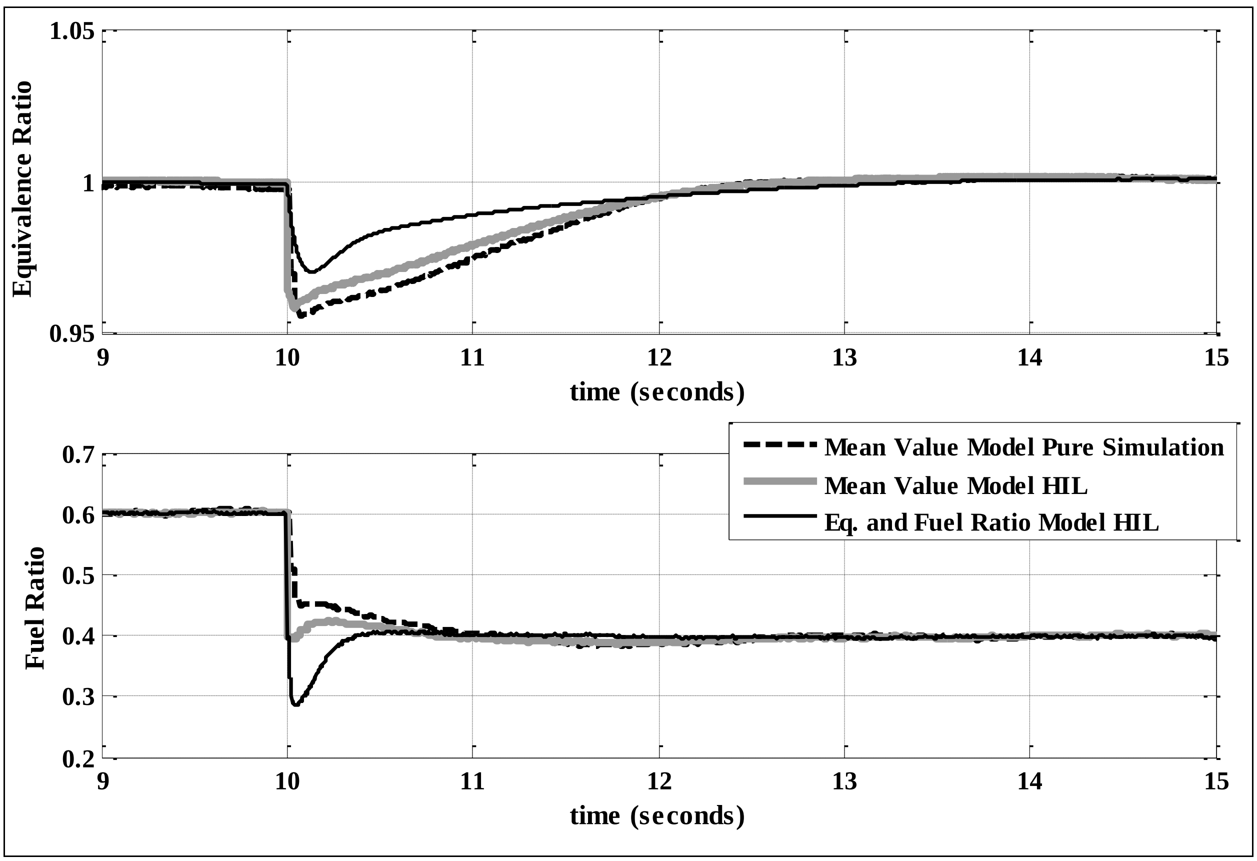

Figure 2-13: CL response of HIL simulation of fuel ratio step down

2.5.2 Simulation 2

Figure 2-14 shows the HIL simulation 2 results of an equivalence ratio step increment from unity to 1.1 at the 30th second. Similarly, the HIL simulation responses show negligible steady state errors of both equivalence and fuel ratios due to cycle-to-cycle air flow dynamics. The mean value engine model HIL simulation equivalence ratio response achieves the target slightly quicker than the other responses and its fuel ratio response also has minimal overshoot. In summary, both the fuel and equivalence ratio step responses demonstrate that the real-time sliding mode controller implemented in the HIL environment was able to achieve similar performance comparing to those of the Matlab simulations.

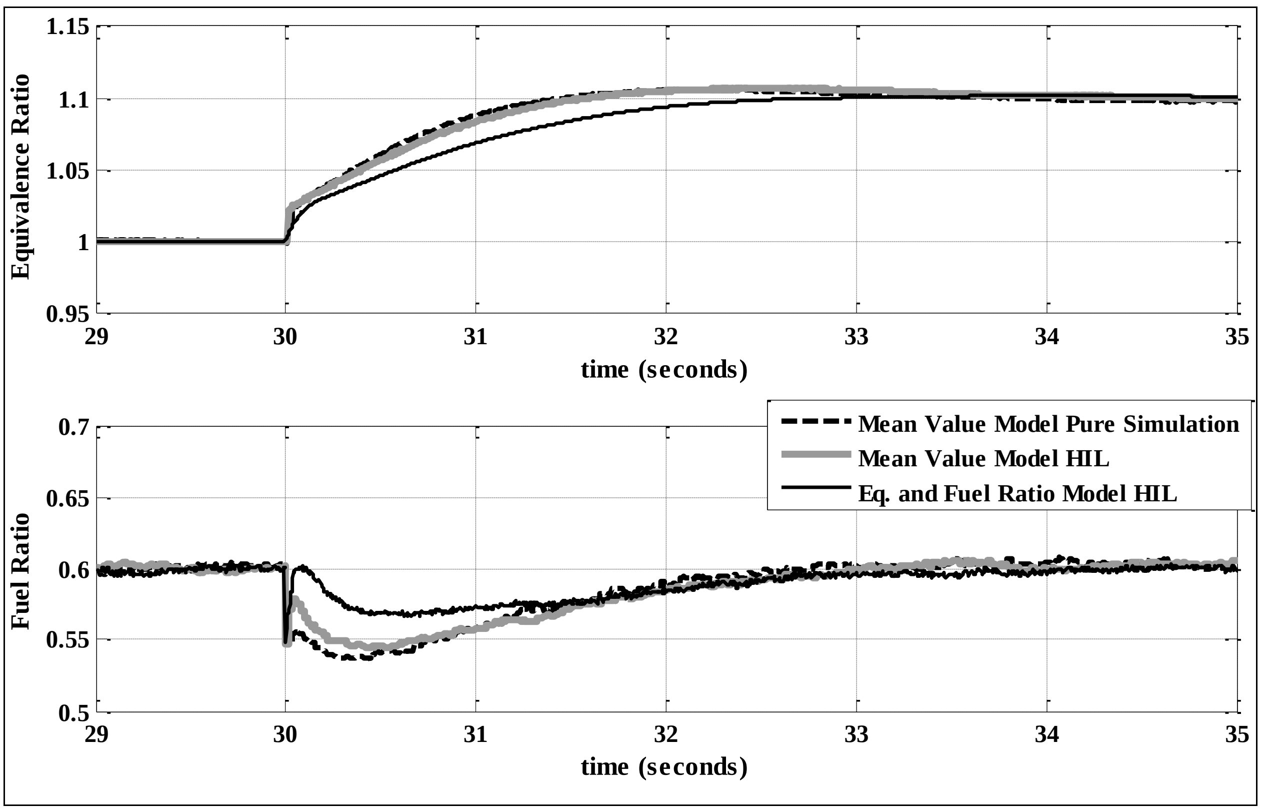

Figure 2-14: CL response of HIL simulation for step equivalence ratio

Chapter 3: Optimal LQ Transient Air-to-Fuel Ratio Control of an Internal Combustion Engine

3.1 Introduction

As discussed in Chapter 1, most modern spark ignited (SI) internal combustion engines maintain their air-to-fuel ratio (AFR) at a desired level to maximize the three-way catalyst conversion efficiency to minimize harmful engine emissions. However, maintaining the engine AFR during its transient operation is quite challenging due to rapid changes of driver demands. Conventional transient AFR control is based upon the inverse dynamics of the engine port-fuel-injection well-wetting dynamics and the measured mass air flow rate. This chapter develops a dynamic linear quadratic (LQ) tracking controller to regulate the AFR using a control oriented model of the wall wetting dynamics of a port fuel injector (PFI) and estimated transport delays of the air flow travel and throttle dynamics. The LQ tracking controller is designed to optimally track the desired AFR based upon the measured air flow through the throttle during engine transients. The LQ tracking controller is designed to reduce the AFR deviation from a desired value during engine transient operations, and it will be implemented as a type of feedforward control. Therefore, performance of the optimal LQ tracking controller will be compared with the conventional inverse fueling dynamics through simulations and results will show improvement over the baseline feedforward controller. The experimental results of the LQ tracking controller will be shown in Chapter 4.

3.2 Previous Transient AFR Control

There have been significant studies through experimental research in the last few decades to characterize the deviation of AFR during engine transient operation. These studies include the use of a transfer function to simulate the mixture-formation process by Stivender [48], a detailed study of the simple phenomenological model for fuel transport in the intake port by Aquino [37], an investigation of fuel transfer characteristics during transient operation including cold start by Hires [49], and Rose *et al*. [50-52] found that the air-fuel ratio deviations were shorter than previously discovered by other researchers.

At the time of these studies, improvements to controlling fuel injection during transients had been limited by lack of quantitative information of the flow processes within the manifold and cylinders. Currently, only a few researchers have developed control strategies for gasoline SI engines that are designed specifically to address and improve the transient AFR control problem. These research efforts include a control strategy that involves a model that takes account of manifold filling and the delays in transport of fuel from the injectors to the cylinder by Hu [53], a simple linear control approach using least squares estimation by Ye [54], and a control strategy that combined the modified Elman neural network and the traditional PI controller by Yao [55]. Ultimately, there has not been much research dedicated to transient AFR control within the last decade few years and thus the need of the optimal LQ transient discussed in this chapter.

3.3 Conventional Feedforward AFR Control

Conventional feedforwad AFR control is based on inverse fueling dynamics, where it is primarily derived from the estimated cylinder air charge divided by the desired stoichiometric ratio of the air and fuel as discussed in Chapter 1. Although the use of feedforward control can significantly improve the transient response of AFR, there is certain room for improvement.

An alternative approach of designing a feedforward AFR control is to use the measured air flow at the engine throttle and its transport delay between engine throttle and cylinder to track the desired AFR during engine transient operations. This control is expected to reduce the AFR tracking error during engine transients.

3.4 AFR Control Problem

The control problem of this chapter is to adjust the port fuel injection rate ω_{PFI} so that the engine AFR deviation from the desired level (e.g., stoichiometry) is minimized during engine transient operations. A control oriented model of the fuel and air flow dynamics is used for AFR control design and evaluation. The fuel flow model includes the wall wetting dynamics of a PFI delivery system; and the air flow model includes throttle dynamics, transport delays, and manifold filling dynamics. A finite horizon linear quadratic (LQ) tracking AFR controller is designed to track the desired AFR using the estimated air flow into the engine cylinder as an input during engine transient operations. The finite horizon LQ tracking control law is updated at every control step, and only the updated first control signal is used for real-time control.

3.5 Air flow and Fuel Flow Model

To begin the design of a control oriented air flow and fuel flow model for the LQ tracking AFR controller, a more complex control oriented hardware-in-the-loop (HIL) four cylinder dual-fuel mean-value engine model developed based upon [1] and modified from [38] was studied extensively to understand the dynamics of air flow and fuel flow system of a typical IC engine. The term “mean-value” indicates that the previously developed engine model neglects the reciprocating behavior of the engine, assuming all processes and effects are spread out over the engine cycle. During HIL simulations, this model describes the input-output behavior of the physical engine systems with reasonable simulation accuracy using relatively low computational throughput. Guzzella [45] provides a good overview of engine modeling, and most of dynamic equations used in the four cylinder model are from this reference book. This engine model also includes all engine transient dynamics. Figure 3-1 shows the overall mean-valve engine model architecture, along with main sub-system models, such as air-to-fuel ratio, manifold air pressure (MAP), brake mean effective pressure (BMEP), engine torque, exhaust temperature, etc.

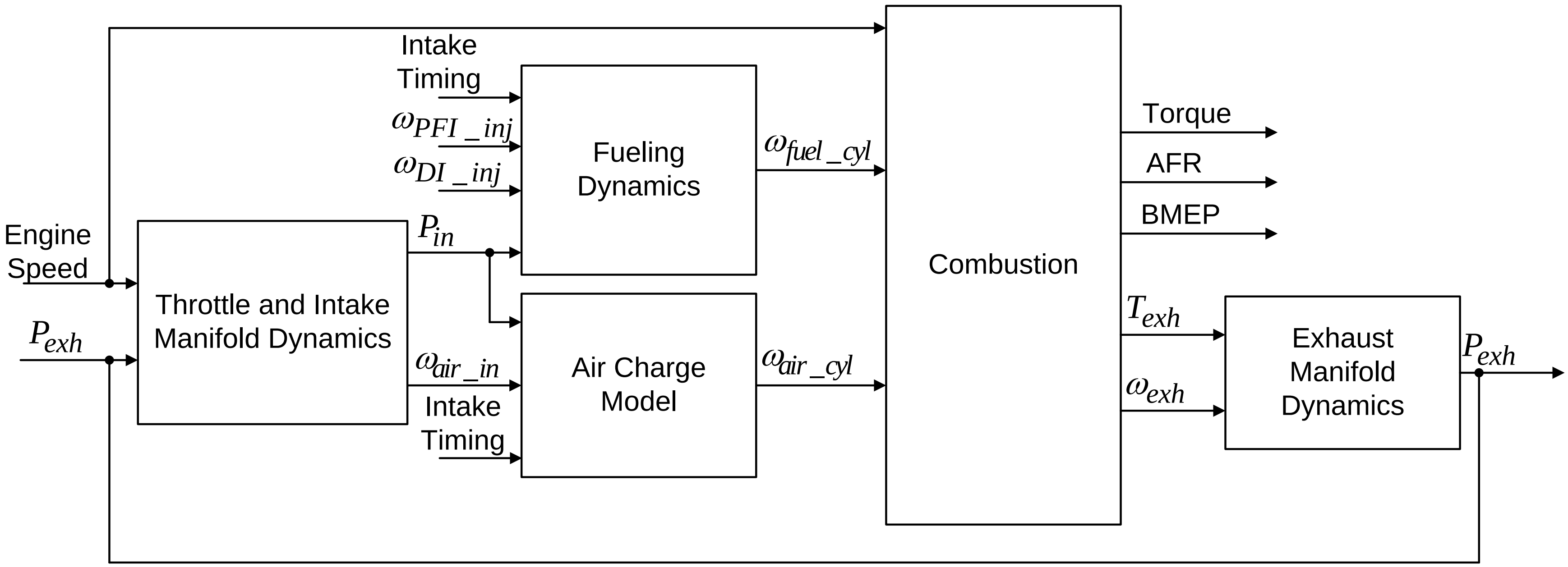

Figure 3-1: Model structure of mean value engine model

The subsystems from Figure 3-1 that were used for the design of the control oriented air flow and fueling model of this work were the throttle and intake manifold dynamics model, fueling dynamics model, air charge model, and engine combustion AFR calculation. The equations used to describe these dynamics and calculations were simplified for controller design purposes, and a linear air and fuel flow model was created as follows.

The engine throttle plate and electrical actuator dynamics are approximated by the following first order transfer function,

$$\omega_{throttle} = \frac{1}{\tau_1 s + 1}\omega_{air}, \tag{59}$$

where τ_1 is the throttle dynamics time constant and is chosen to be 0.03 in this model. The state space representation of the throttle dynamics is,

$$\begin{aligned} \dot{x}_{throttle} &= -\frac{1}{\tau_1}x_{throttle} + \frac{1}{\tau_1}\omega_{air} \\ z_{throttle} &= x_{throttle} \end{aligned} \tag{60}$$

The isothermal model of the filling dynamics of an engine intake manifold can be approximated by a first order transfer function as,

$$\omega_{manifold} = \frac{1}{\tau_2 s + 1}\omega_{throttle}, \tag{61}$$

where τ_2 is chosen to be 0.05 in this model. The air flow travel delay from engine throttle to cylinder, typically a function of engine speed, is approximated as a pure transport delay and is chosen to be 100ms at 1500 RPM.

The fuel flow wall-wetting dynamics from the port injector is modeled by the following transfer function,

$$\omega_{PFI} = \frac{\alpha s + 1}{\beta s + 1}, \quad (62)$$

where α and β are selected to be 0.5 and 0.8 at 1500 RPM, respectively, in this model. The fuel flow wall-wetting model for discrete time dynamics proposed by Aquino in [37] was modified for use as the continuous time model in (62). In addition to the wall-wetting dynamics, there is an average PFI fuel injection delay of 50ms, which is approximated by a unitary gain first order transfer function, similar to (59) and (61). The state space representation for the complete PFI fueling dynamics is,

$$\begin{aligned} \dot{x}_{fuel} &= \begin{bmatrix} -\frac{1}{\tau_2} & 0 \\ \frac{1}{\beta}\left(1 - \frac{\alpha}{\beta}\right) & -\frac{1}{\beta} \end{bmatrix} x_{fuel} + \begin{bmatrix} \frac{1}{\tau_2} \\ 0 \end{bmatrix} u_{fuel} \\ y_{fuel} &= \begin{bmatrix} \frac{\alpha}{\beta} & 1 \end{bmatrix} x_{fuel} \end{aligned} \quad (63)$$

where u_{fuel} is the input to the PFI injector and y_{fuel} is the fuel injected by the PFI injector. Also note that $y_{fuel} = \omega_{PFI}$.

Due to the three way catalyst used for emission control, most engines are designed to achieve a target A/F ratio around stoichiometric to maximize the conversion efficiency. For this study, we use a normalized target A/F ratio, λ_{target}, which is defined as desired air-to-fuel ratio divided by stoichiometric air-to-fuel ratio. Note that at stoichiometry the normalized target A/F ratio is equal to one. The normalized A/F ratio can be calculated as,

$$\lambda = \frac{\omega_{cyl}}{14.6 \cdot \omega_{PFI}}. \quad (64)$$

A schematic diagram of the AFR control scheme is shown in Figure 3-2 and the details of the LQ tracking controller will be discussed in detail in the following section.

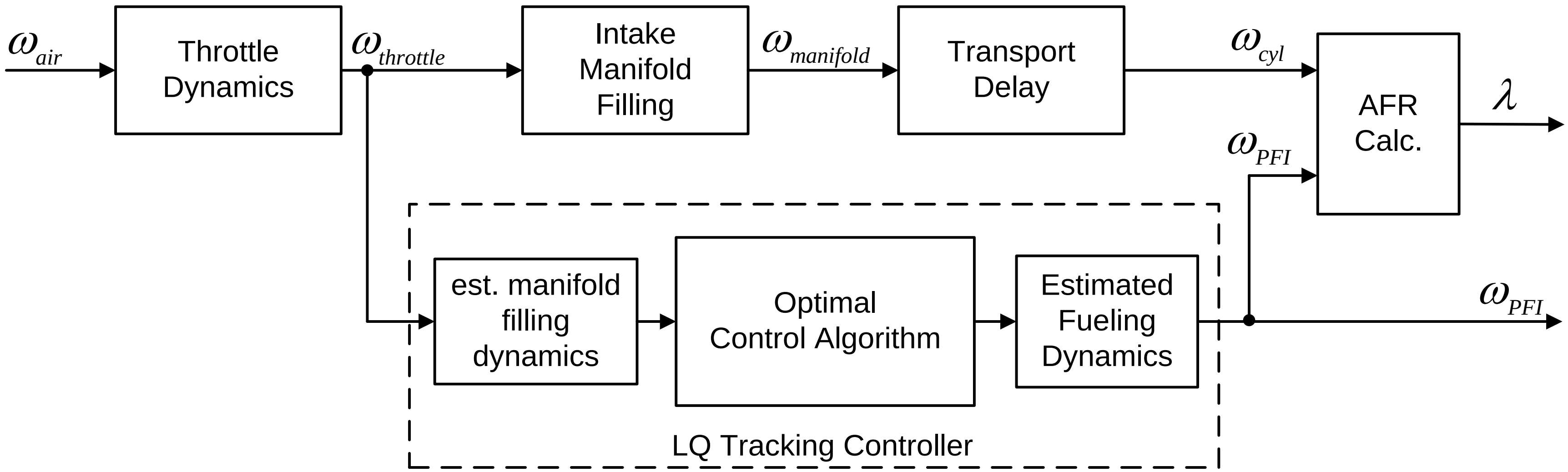

Figure 3-2: Schematic diagram of the AFR control problem

3.6 Linear Quadratic Tracking Controller Design

In this section, a finite horizon linear quadratic (LQ) tracking AFR controller is designed based on the model previously described to track the desired normalized air-to-fuel ratio during engine transients. More specifically, the control objective is for y_{fuel} to optimally track λ_{target} over a given time interval. Later, the optimal control problem will be transferred to an equivalent optimal control problem to minimize the tracking error between the measured air flow and the product of fuel flow and desired air-to-fuel ratio.

The continuous time system in (63) is discretized at a sample rate of 10 ms. Thus it becomes a linear, time-invariant system described below,

$$\begin{aligned} x_{fuel}(k+1) &= Ax_{fuel}(k) + Bu_{fuel}(k) \\ y_{fuel}(k) &= Cx_{fuel}(k) \end{aligned} \tag{65}$$

The values for the matrices of discrete time system (65) are,

$$\begin{aligned} A &= \begin{bmatrix} 1.7664 & -0.887 \\ 0.887 & 0 \end{bmatrix}; \quad B = \begin{bmatrix} 1 \\ 0 \end{bmatrix}; \\ C &= \begin{bmatrix} 0.13825 & -0.1545 \end{bmatrix} \end{aligned}$$

Similarly, the output of the continuous time system in (60) is discretized at a sample rate of 10 ms.

For notational simplicity, x_k, u_k, y_k, *and* z_k will be used to denote the system state, control, output, and reference air flow vectors, respectively at time k, i.e. $x(k)$, $u(k)$, $y(k)$ and $z(k)$. Consider the discrete-time, linear time-invariant system in (65) and define the performance cost function to be minimized as,

$$\begin{aligned} J(k) &= \frac{1}{2}\left[Cx_{k_f} - z_{k_f} \right]^T F \left[Cx_{k_f} - z_{k_f} \right] \\ &+ \frac{1}{2}\sum_{k=k_0}^{k_f-1} \left\{ \left[Cx_k - z_k \right]^T Q \left[Cx_k - z_k \right] + u_k^T R u_k \right\} \end{aligned} \tag{66}$$

where, x_k, u_k, y_k, and z_k are n, r, n, and n-dimensional vectors, respectively. Also F *and* Q are $n{\times}n$ positive semidefinite symmetric matrices and R is an $r{\times}r$ positive definite symmetric matrix. The initial state is x_{k0} and the final state x_{kf} is free with k_f fixed, thus this is a finite horizon linear quadratic (LQ) control problem. The performance cost function (66) is chosen such that the error,

$$\begin{aligned} e(k) &= y_{fuel}(k) - z_{throttle}(k) \\ &= y_k - z_k \end{aligned} \tag{67}$$

is as small as possible with minimum control effort.

3.6.1 Hamiltonian Equation

To begin the methodology of obtaining the solution for the optimal tracking system, we first define the Lagrangian function as,

$$L(x_k, u_k) = \frac{1}{2}\sum_{k=k_0}^{k_f-1} \left\{ \left[Cx_k - z_k \right]^T Q \left[Cx_k - z_k \right] + u_k^T R u_k \right\} \tag{68}$$

and formulate the Hamiltonian as,

$$\begin{aligned} H(x_k, u_k, p_{k+1}) &= L(x_k, u_k) + p_{k+1}^T \left[Ax_k + Bu_k \right] \\ &= \frac{1}{2}\sum_{k=k_0}^{k_f-1} \left\{ \left[Cx_k - z_k \right]^T Q \left[Cx_k - z_k \right] + u_k^T R u_k \right\} + p_{k+1}^T \left[Ax_k + Bu_k \right] \end{aligned} \tag{69}$$

where p_{k+1} is the costate.

3.6.2 State and Costate Equations

From [56], the optimal state equation for the tracking system can be found by taking the partial derivative, with respect to the costate p_{k+1}, of the Hamiltonian equation in (69), as shown below,

$$x_{k+1}^{*} = \frac{\partial H(x_k, u_k, p_{k+1})}{\partial p_{k+1}^{*}} = Ax_k^{*} + Bu_k^{*} \tag{70}$$

Similarly, the optimal costate equation can also be found by taking the partial derivative, with respect to the state x_k, of the Hamiltonian equation in (69), as shown below,

$$p_k^{*} = \frac{\partial H(x_k, u_k, p_{k+1})}{\partial x_k^{*}} = A^T p_{k+1}^{*} + C^T QCx_k^{*} - C^T Qz_k, \tag{71}$$

noting that in the above equations "*" denotes the optimal trajectories of the corresponding vectors. The boundary condition or final condition for the costate is,

$$p_{k_f} = C^T FCx_{k_f} - C^T Fz_{k_f}. \tag{72}$$

3.6.3 Open Loop Optimal Control Equation

The control equation for the tracking system can be found by setting the partial derivative, with respect to the control u_k, of the Hamiltonian equation in (69) equal to zero and then solving for the optimal control, as shown below,

$$\frac{\partial H(x_k, u_k, p_{k+1})}{\partial u_k^{*}} = 0 \Rightarrow u_k^{*} = -R^{-1} B^T p_{k+1}^{*}. \tag{73}$$

Notice that at this point, (73) is an open loop optimal control. By substituting this control into the state and costate equations in (71) and (72), respectively, the following system is obtained

$$\begin{bmatrix} x^*_{k+1} \\ p^*_k \end{bmatrix} = \begin{bmatrix} A & -E \\ V & A^T \end{bmatrix} \begin{bmatrix} x^*_k \\ p^*_{k+1} \end{bmatrix} + \begin{bmatrix} x^*_k \\ p^*_{k+1} \end{bmatrix} z_k \tag{74}$$

where, $E=BR^{-1}B^T$ and $V=C^TQC$.

3.6.4 Riccati and Vector Difference Equations

To obtain a closed loop form for the optimal control in (73), we assume that the final condition in (72) is of the form,

$$p^*_k = K_k x^*_k - g_k \tag{75}$$

where the matrix K_k and g_k will be determined by using (75) to eliminate the costate from the system in (74). First consider the substitution of (75) into the state equation of (74), which becomes

$$x^*_{k+1} = Ax^*_k - EK_{k+1}x^*_{k+1} + Eg_{k+1}. \tag{76}$$

Solving for x^*_{k+1} yields,

$$x^*_{k+1} = \left(I + EK_{k+1}\right)^{-1}\left(Ax^*_k + Eg_{k+1}\right). \tag{77}$$

Next, consider the substitution of (75) and (77) into the costate equation of (74), which becomes,

$$\begin{gathered} \left[-K_k + A^T K_{k+1}\left(I + EK_{k+1}\right)^{-1} A + V\right]x_k + \\ \left[g_k + A^T K_{k+1}\left(I + EK_{k+1}\right)^{-1} Eg_{k+1}\right] - A^T g_{k+1} + Wz_k = 0 \end{gathered} \tag{78}$$

The above equation must hold for all values of the optimal state x^*_{k+1}. Therefore, the coefficient of x_k and the remaining terms must individually vanish. That is,

$$K_k = A^T K_{k+1}\left(I + EK_{k+1}\right)^{-1} A + V \tag{79}$$

and,

$$g_k = A^T T g_{k+1} + C^T Q z_k \tag{80}$$

where,

$$T = I - \left(K_{k+1}^{-1} + E\right)^{-1} E. \tag{81}$$

The corresponding boundary conditions for (79) and (80) respectively, are,

$$K_{k_f} = C^T F C \tag{82}$$

$$g_{k_f} = C^T F z_{k_f} \tag{83}$$

Note that (79) is a nonlinear matrix difference Riccati equation to be solved backwards using the final condition (82), and the linear vector difference equation (81) is also solved backwards using the final condition (83).

3.6.5 Closed Loop Optimal Control Equation

Once the Ricatti and vector difference equations have been solved, they can be substituted into the open loop optimal control equation in (73) and it can be rewritten as,

$$u_k^* = -R^{-1} B^T K_{k+1} x_{k+1} + R^{-1} B^T g_{k+1}. \tag{84}$$

Substituting for the state from (70),

$$u_k^* = -R^{-1} B^T K_{k+1}\left(A x_k^* + B u_k^*\right) + R^{-1} B^T g_{k+1}. \tag{85}$$

Multiplying (85) by R and solving for the optimal control results in,

$$u_k^* = -L1_k\, x_k^* + L2_k\, g_{k+1} \tag{86}$$

where $L1$ and $L2$ are the feedback and feedforward gains, respectively. They are defined as,

$$L1_k = \left(R + B^T K_{k+1} B\right)^{-1} B^T K_{k+1} A \tag{87}$$

$$L2_k = \left(R + B^T K_{k+1} B\right)^{-1} B^T \tag{88}$$

Note that optimal control equation in (86) requires the state x, which is used as feedback from the estimated fueling dynamics. Therefore, (86) is a closed loop optimal control. Lastly, the optimal state trajectory in (70) can now be rewritten using (86) as,

$$x_{k+1}^* = \left(A - B \cdot L1_k\right) x_k^* + B \cdot L2_k\, g_{k+1}. \tag{89}$$

Thus, all components of the design of the LQ tracking controller have been derived and its implementation will be discussed in the next section.

3.6.6 Implementation of LQ Tracking Controller

The implementation of the discrete time LQ tracking controller begins by discretizing the estimated intake manifold filling dynamics in equation (61) are also discretized at a sample rate of 10 ms, resulting in the following,

$$\begin{aligned} x_m(k+1) &= A_m x_m(k) + B_m z_{throttle}(k) \\ y_m(k) &= C_m x_m(k) \end{aligned} \tag{90}$$

where the values for the matrices of (90) are,

$$\begin{aligned} A_m &= 0.8187; \quad B_m = 0.009063; \\ C_m &= 20. \end{aligned}$$

Notice that the input of the system in equation (90) is the output of the throttle plate and electrical actuator dynamics, $z_{throttle}$, approximated in equation (59), discretized at a sample rate of 10 ms.

Figure 3-3 shows the details of the implementation of the LQ tracking control scheme and will be described as follows. First, the estimated air flow measured by the mass air flow sensor is used to estimate the manifold filling dynamics of (90).

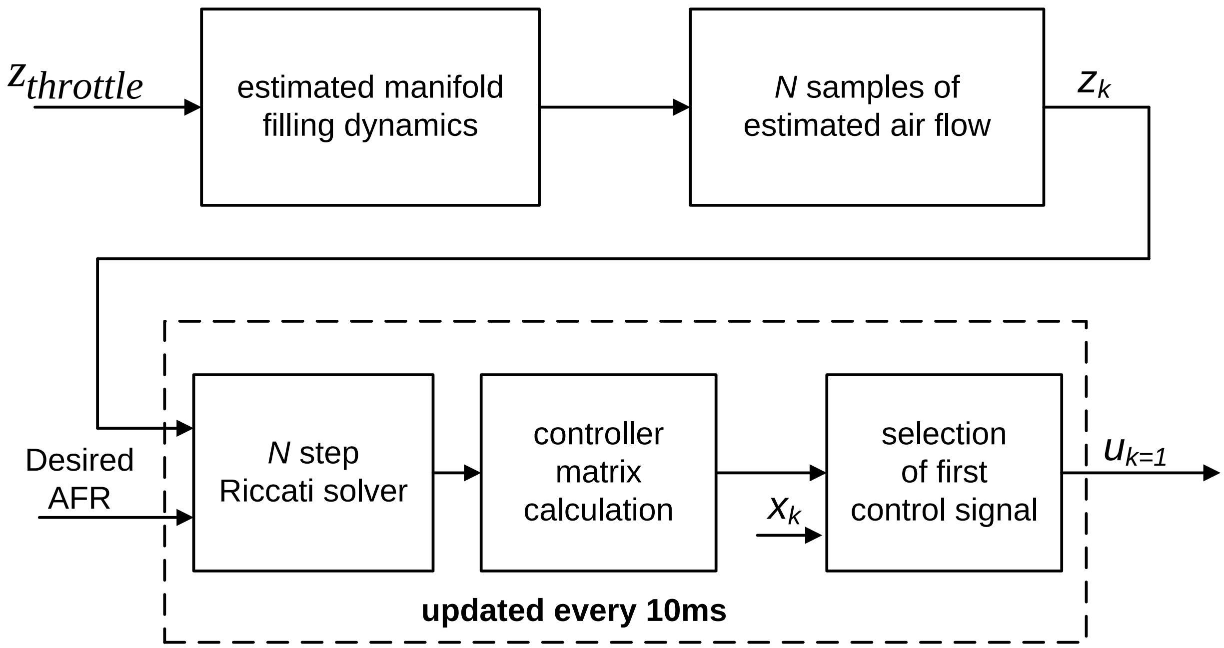

Figure 3-3: Schematic of LQ tracking controller

Next, this estimated air flow must be sampled every 10 ms and indexed and stored in memory for a fixed number of sample times, N. These N samples are used as the reference vector z, thus z has length N. This is done so that for every control step of 10ms, the control gain matrices and Riccati difference equations can be solved for each of the given N samples. As previously discussed, the Riccati difference equations (79) and (80) are solved backwards for N steps and are updated every 10 ms, where $k_0 = 0$ and $k_f = N$. Similarly, the controller matrices (87) and (88) are calculated during the same control step and the closed loop optimal control (86) is obtained. Consequently, at the next control step only the first control signal out of all N control signals calculated is used for controlling the PFI injector and in the next step, the N

control signals will be recalculated by following the same procedure and using the updated air flow estimation. For this study, N was set equal to 10, and thus the controller requires 10 samples of estimated air flow to solve the Riccati equations and to determine the controller matrices at every control step, which equates to 100 ms of real-time simulation. Due to the air flow transport delay, there is sufficient time to calculate the optimal fueling based upon the predicted air flow into the engine cylinder.

Figure 3-4 shows a simple schematic of the timing of the overall AFR control scheme. Notice that a step increase in the air flow is measured by the MAF sensor, and this air flow first travels through the throttle. Several sample times later, the same air flow travels to the intake manifold and this is taken as a pure transport time delay. The LQ tracking controller updates the controller matrices and determines the fuel injection signal, and after a fuel time delay, the fuel is injected by the injector.

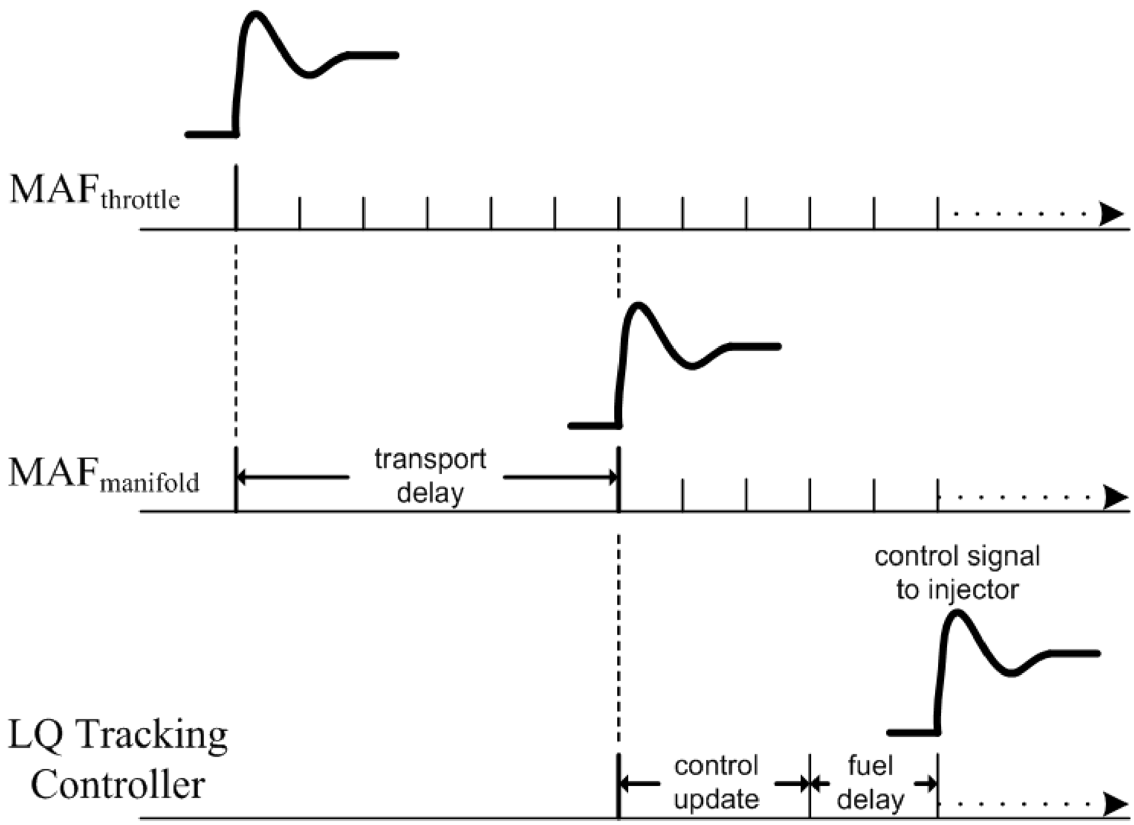

Figure 3-4: Timing of LQ tracking control scheme

3.7 Inverse Fueling Dynamics Controller

Since typical feedforward AFR control is achieved by using inverse fueling and the estimated cylinder air charge divided by the desired stoichiometric ratio of the air and fuel, a baseline inverse fueling dynamics controller was developed for comparison purposes to the LQ tracking controller. The controller uses the inverse wall wetting dynamics of the PFI injector and the estimated air flow measured by the mass air flow sensor to determine the desired stoichiometric ratio of the air and fuel. In conventional inverse fueling dynamics control, the inverse of the fuel injection time delay is used and contains a non-minimum phase zero when it is approximated by the follow transfer function

$$e^{-\tau s} \approx \frac{1-\frac{\tau}{2s}}{1+\frac{\tau}{2s}}. \tag{91}$$

Instead of using the inverse of the fuel injection time delay, only the inverse of the wall wetting dynamics is used in this baseline controller. The baseline controller also includes the estimated manifold filling dynamics, having the similar structure as (90), and a pure delay to match the physical transport delay of the air flow from the throttle to the engine cylinder. See Figure 3-5 for the schematic of the baseline inverse fueling dynamics controller.

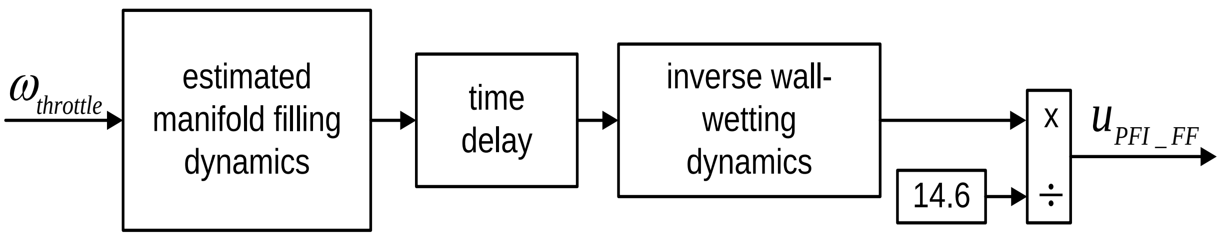

Figure 3-5: Schematic of baseline inverse fueling dynamics controller

3.8 Simulation Results

Simulations of the LQ tracking controller under different throttle opening changes were conducted and compared to the inverse fueling dynamics controller. The performance cost function matrices were tuned each simulation such that the transient response was acceptable and were selected below as

$$F = Q = \begin{bmatrix} 100 & 0 \\ 0 & 100 \end{bmatrix}; R = 0.000000001.$$

Selection of the weighting matrices *F*, *Q*, and *R* indicates that less emphasis is placed on the control effort, *u*, in the performance cost function of (66). Or equivalently, minimizing the tracking error (67) is most important regardless of the amount of control effort. This is suitable since the overall control problem is to minimize the engine AFR deviation from a desired level during engine transient operations, which in general will improve engine fuel efficiency and reduce engine emissions. Placing more emphasis on minimizing the tracking error from the selection of these matrices was found to be acceptable because there was no singularity in the solution of the Riccati equations and also the fueling input was not saturated.

3.8.1 Simulation 1

A constant air flow of 0.5 grams/s was used to begin simulation 1. Figure 3-6 shows the response of the inverse fueling dynamics controller and the LQ tracking controller for simulation 1. The simulation adds 2% sensor noise to the estimated air flow across the throttle to account for throttle estimation inaccuracy, and adds a step increase of 25% air flow at the 5th second. At the 10th second a decrease of 15% air flow was applied. The upper plot of Figure 3-6 shows the air flow into the cylinder and its relative fuel flow, and the lower plot shows the AFR response to the throttle changes. The LQ tracking controller maintains the maximum AFR deviation from stoichiometry to fewer than 2%, whereas the inverse fueling dynamics controller only maintains the maximum AFR deviation to 6%.

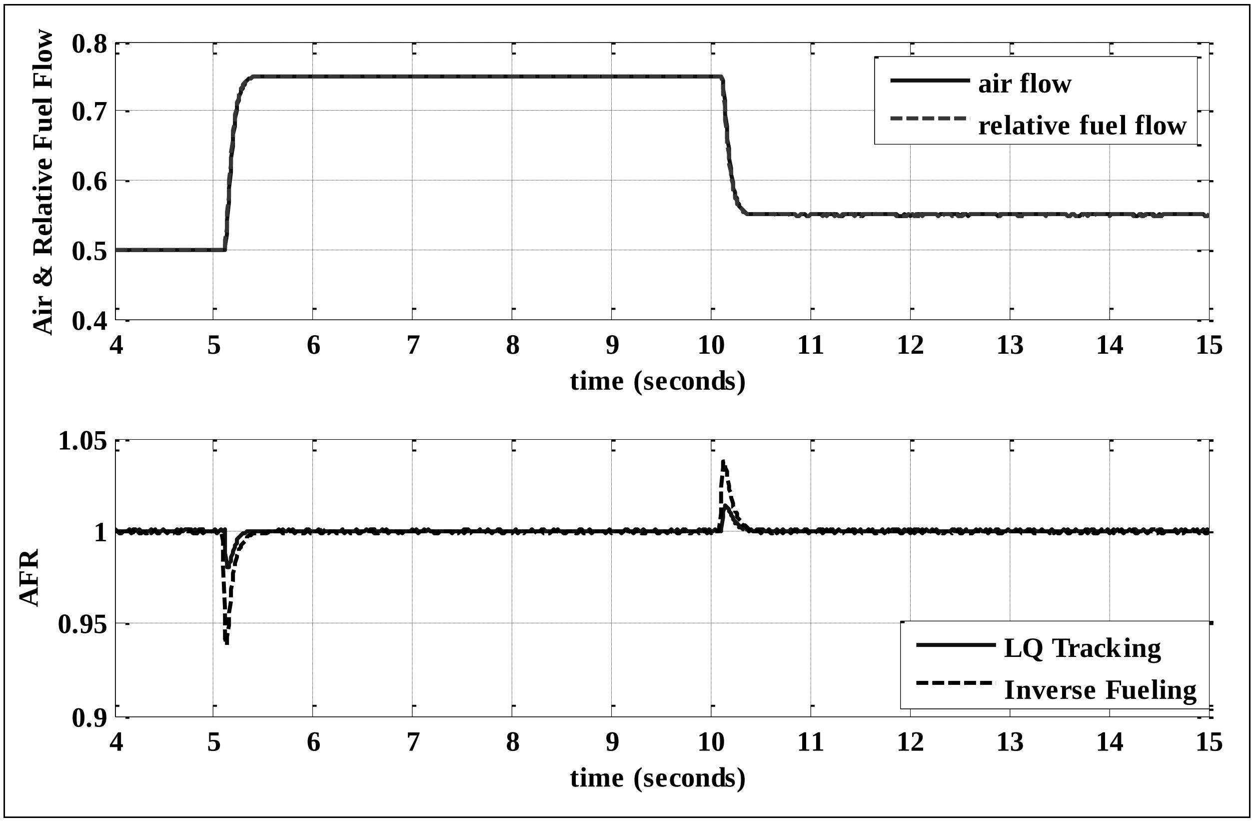

Figure 3-6: Response of simulation 1

3.8.2 Simulation 2

To further validate the LQ tracking controller, the four cylinder mean value model, discussed in the beginning of the air flow and fuel flow modeling discussion in section 3.5, was used in simulations 2 and also in simulation 3. A constant throttle opening of 40% was used to begin simulation 2. Figure 3-7 shows the response of the inverse fueling dynamics controller and the LQ tracking controller for simulation 2. Similar to simulation 1, this simulation also adds 2% sensor noise to the estimated air flow across the throttle, and adds a step increase of 25% to the throttle opening at the 5th second. At the 10th second a decrease of 15% to the throttle opening was applied. The upper plot of Figure 3-7 shows the air flow into the cylinder and its relative fuel flow, and the lower plot shows the AFR response to the throttle changes.

Again, the LQ tracking controller maintains the maximum AFR deviation from stoichiometry to fewer than 2%, whereas the inverse fueling dynamics controller only maintains the maximum AFR deviation to 9%. This simulation is significant because it validates the LQ tracking controller on a more complex engine model, showing that it has potential to be implemented on a real engine.

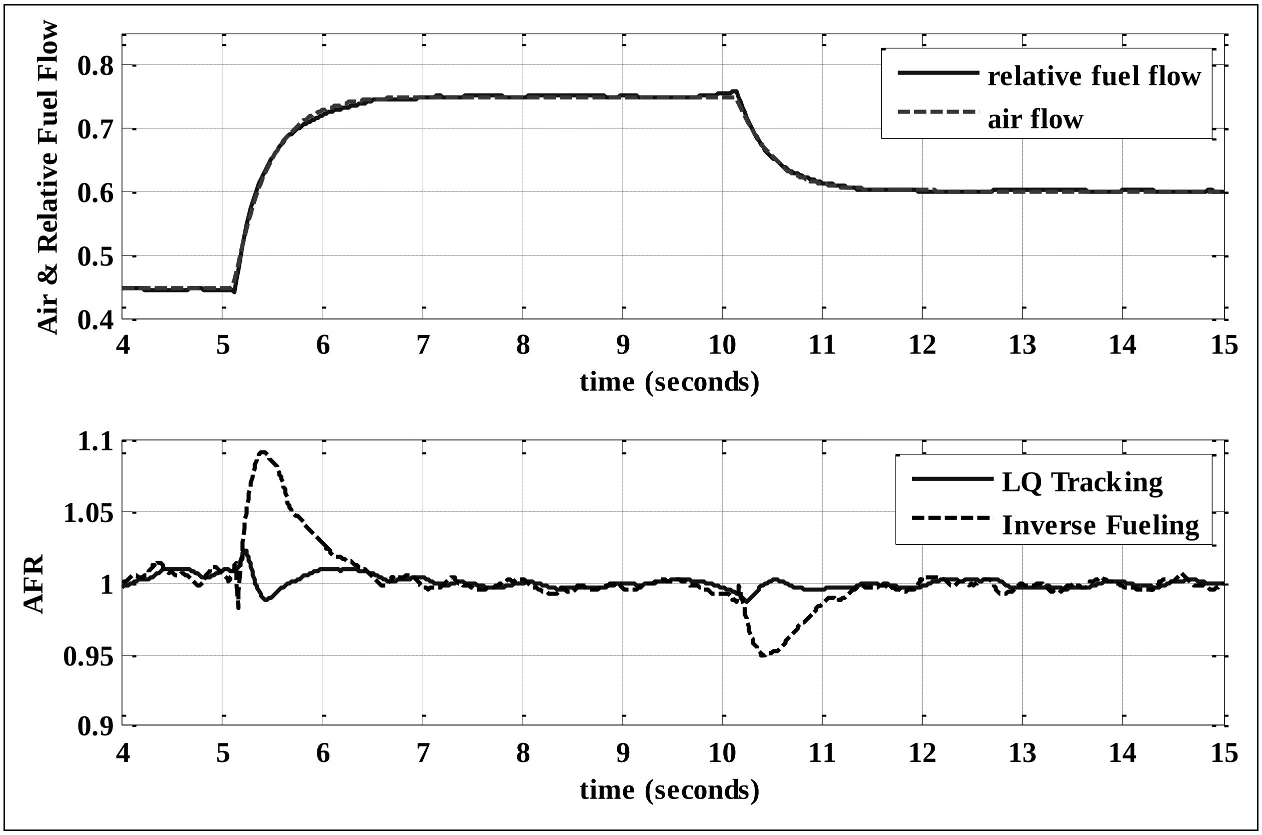

Figure 3-7: Response of simulation 2

3.8.3 Simulation 3

For the previous simulations, a constant target relative AFR of 1 was used. In simulation 3, it begins with a target relative AFR of 1 and a constant engine throttle opening of 40%. At the 5th second the simulation adds both a step decrease of 0.05 to the relative AFR and a step increase 25 % to the throttle opening the. At the 10th second both an increase back to unity AFR and a decrease of 15% to the throttle opening is achieved. This is to simulate the step-throttle engine operation where the reference air-to-fuel ratio is reduced to improve engine knock tolerance. Figure 3-8 shows the response of simulation 3 under the throttle changes and engine relative AFR changes. As seen in the lower plot of Figure 3-8, the LQ tracking controller maintains the deviation of the AFR from stoichiometry to fewer than 2%. The inverse fueling dynamics controller has an AFR deviation of 5%.

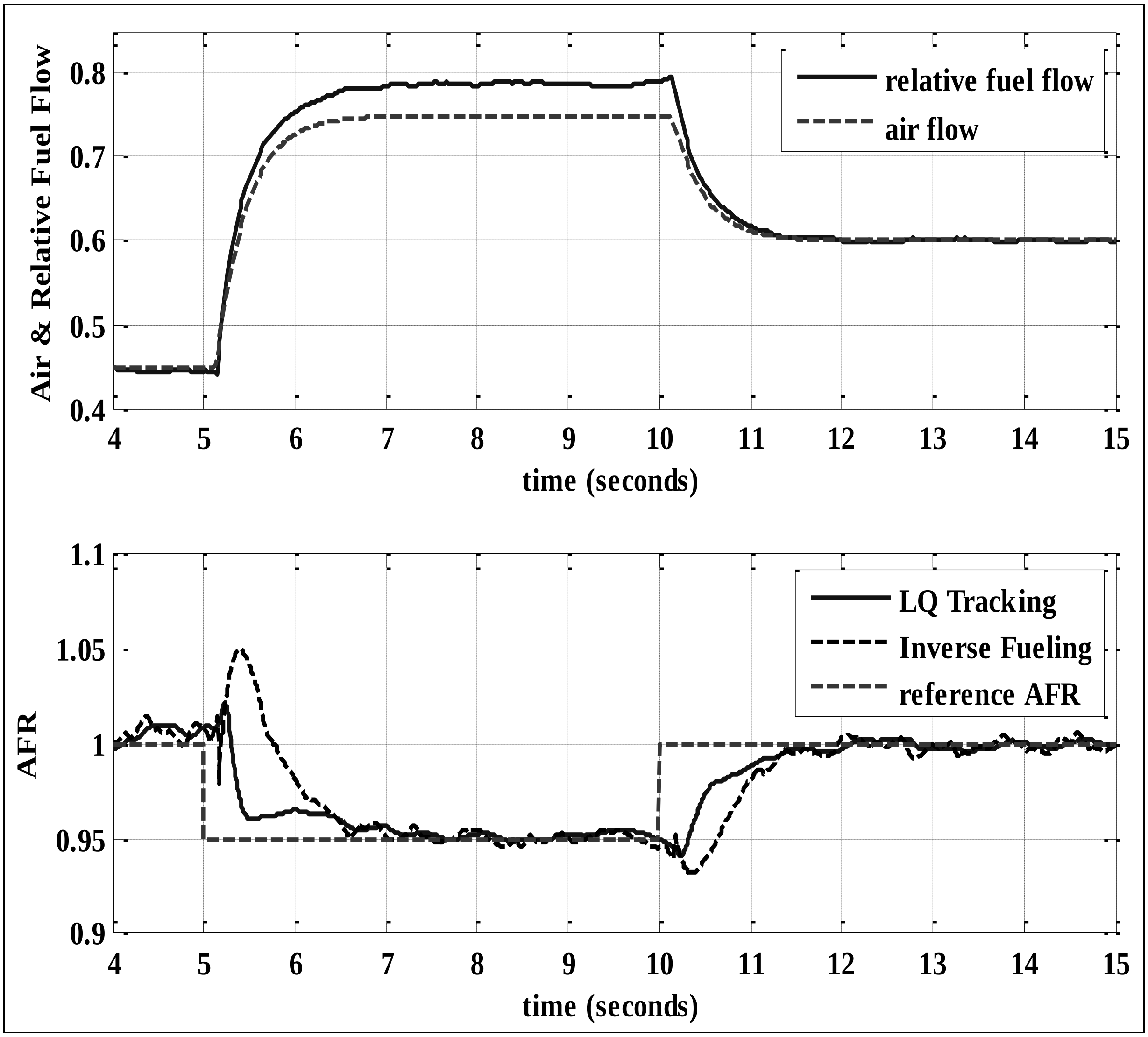

Figure 3-8: Response of simulation 3

3.8.4 Simulation 4

Since the wall-wetting dynamics of the port fuel injector can be influenced by various engine conditions, simulation 4 was conducted to show the controllers performance for various coolant temperatures. The mean value engine model takes into account the coolant temperature in its wall-wetting parameters and has the capability to change the coolant temperature. In simulations 2 and 3, the coolant temperature was 353 Kelvin (K) degrees and was constant throughout each simulation. Simulation 4 conducts three separate simulations for 3 different coolant temperatures, 360K, 310K, and 260K. Each of the conditions in simulation 4 are very similar to simulation 3, beginning with a target relative AFR of 1 and a constant engine throttle opening of 40%. At the 5th second, the simulation adds both a step decrease of 0.05 to the relative AFR and a step increase of 25% to the throttle opening the. At the 10th second, both an increase back to unity AFR and a decrease of 15% to the throttle opening is achieved. Figure 3-9 shows the response of simulation 4 for the three different coolant temperatures. Notice that for each temperature, the LQ tracking controller is able to maintain the AFR deviation to less than 3% during engine transients.

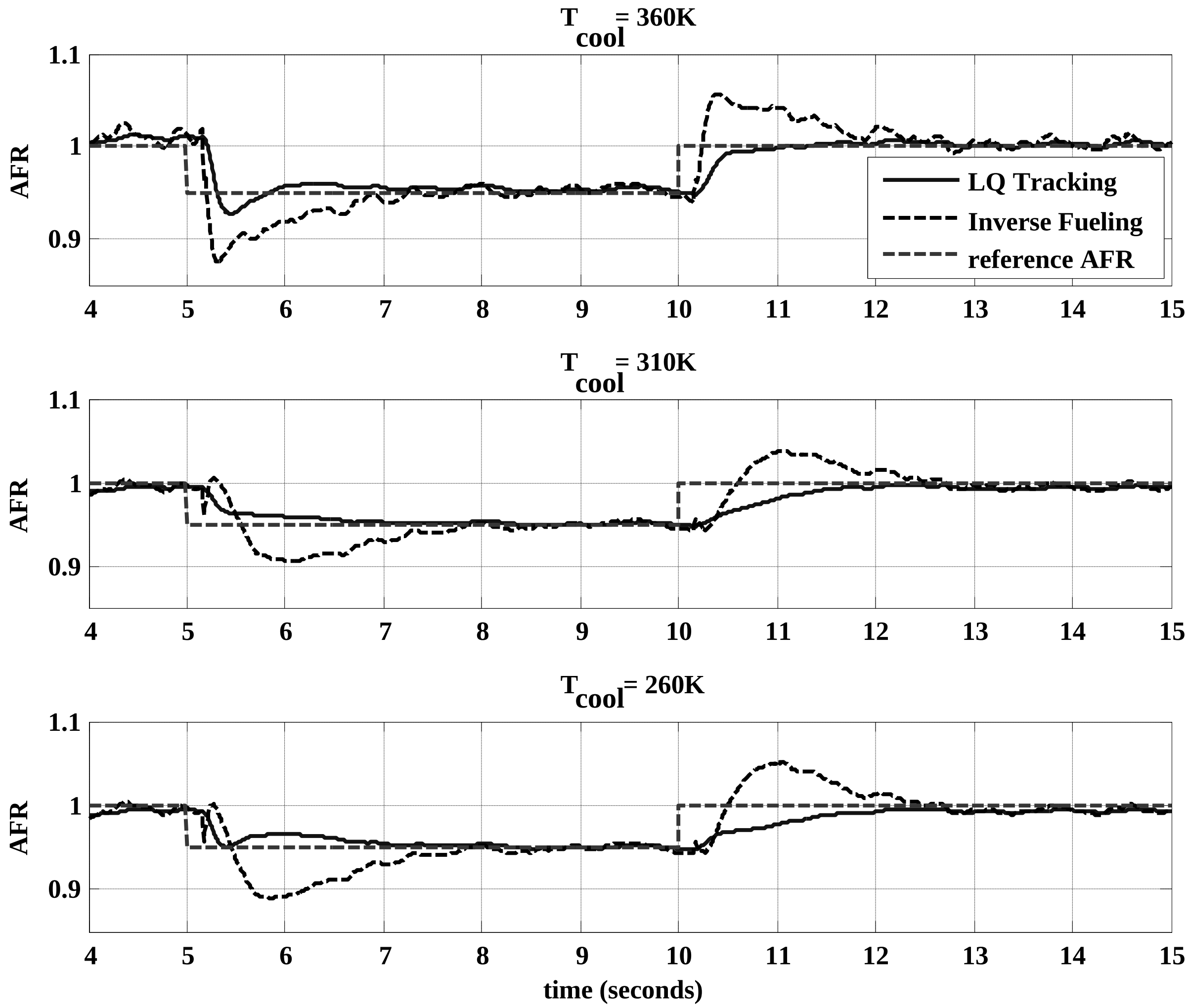

Figure 3-9: Response of simulation 4

3.8.5 Simulation 5

Recall the selection of the weighting matrix R, where it is chosen such that less emphasis is placed on the control effort, u, in the performance cost function of (66). For simulation 5, R is varied, indicating that the matrix does not have the same value for each control step. For case 1, let R be chosen as

$$R_k = \begin{bmatrix} 10^{-11} & 10^{-11} & 10^{-11} & 10^{-5} & 10^{-5} & 10^{-5} & 10^{-5} & 10^{-5} & 10^{-5} & 10^{-5} \end{bmatrix} \quad (92)$$

and note that N = 10. Therefore R is much smaller at the beginning of the calculation of the Riccati equations and controller matrices than it is at the end. Since in the implementation of the LQ tracking controller only the first control signal out of all N that are calculated is used to control the PFI injector, varying R_1 affects the performance of the LQ tracking controller. These effects can be seen in Figure 3-10, where the relative fuel flow is tracking the estimated reference air flow. Notice that as R_1 increases, the tracking performance decreases significantly.

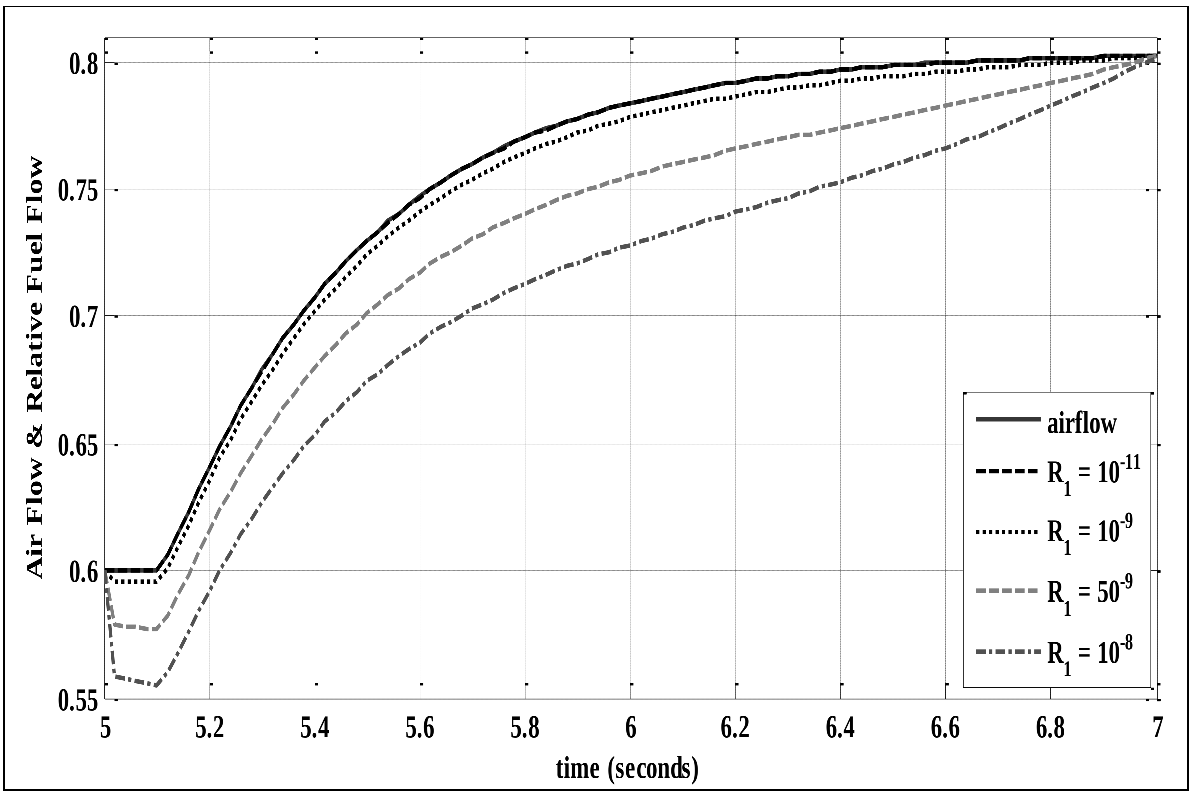

Figure 3-10: Response of simulation 5 case 1

For case 2, let R be chosen as

$$R_k = \begin{bmatrix} 10^{-5} & 10^{-5} & 10^{-5} & 10^{-5} & 10^{-5} & 10^{-5} & 10^{-5} & 10^{-11} & 10^{-11} & 10^{-11} \end{bmatrix} \quad (93)$$

and again note that $N = 10$. Therefore R is much larger at the end of the calculation of the calculation of the Riccati equations and controller matrices than it is at the beginning. In this case, when R_{10} is varied, it has no effect on the LQ tracking controller's performance as shown in Figure 3-11

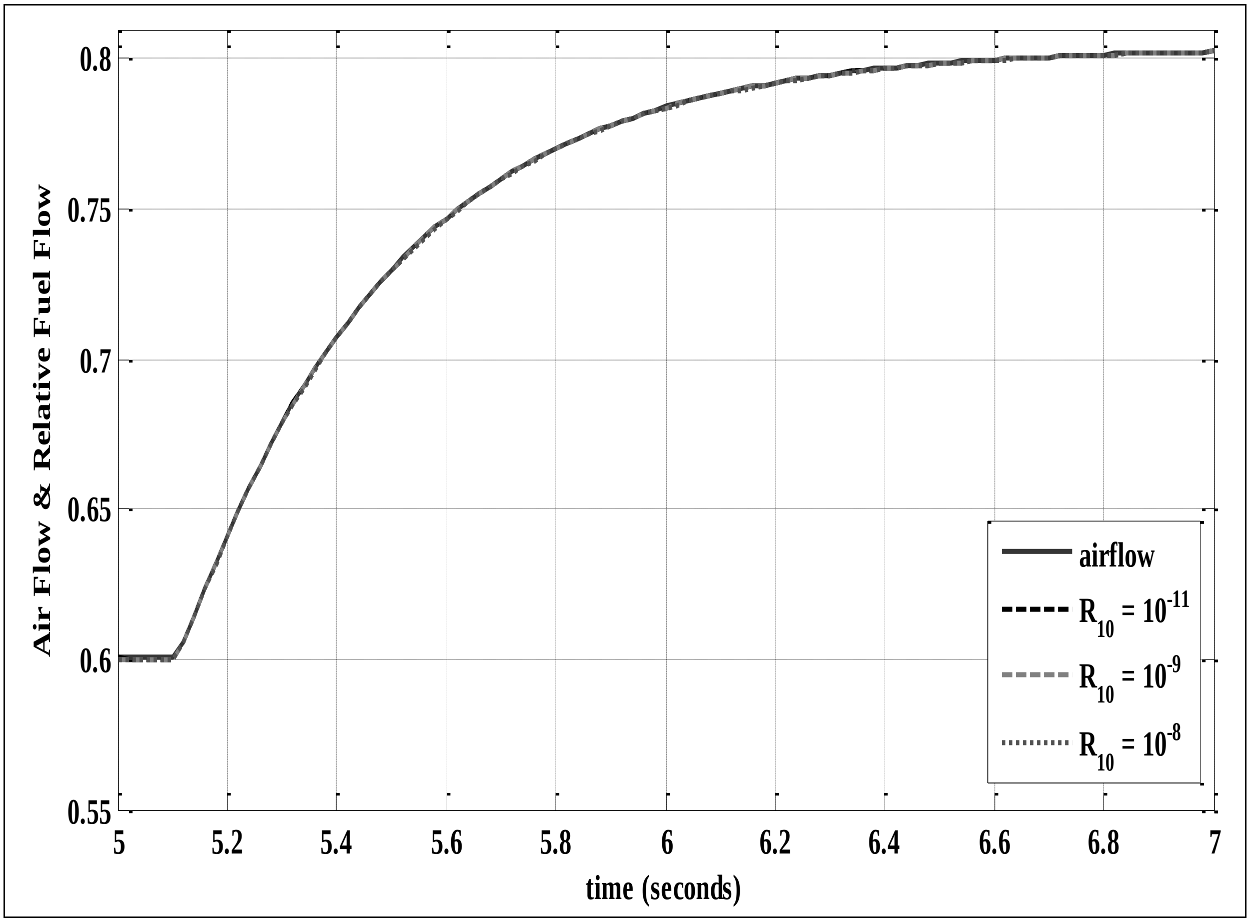

Figure 3-11: Response of simulation 5 case 2

Chapter 4: Experimental Engine Tests of Air-to-fuel Ratio Control

4.1 Experimental Setup

The Linear Quadratic (LQ) tracking controller was implemented and tested on engine dynamometer (dyno). The engine used for all experimental tests was a 0.4 liter single cylinder direct injection engine equipped with variable valve timing (VVT). Table 4-1 lists the engine specifications.

Number of Cylinders	1
Total Displacement	0.4 liter
Bore	83 mm
Stroke	73.9 mm
Rod	225 mm
Compression Ratio	12:1

Table 4-1: Engine specifications

The maximum engine indicated mean effective pressure (IMEP) for the LQ tracking controller tests was 13 bar (non-boosted at 1500 RPM), and the VVT position was fixed during all tests. Spark timing for all experiments was chosen such that combustion was stable and the coefficient of variation (COV) was less than 5 percent. The single cylinder test engine on the engine dynamometer is shown in Figure 4-1. Since the engine was equipped with a DI injector, wall wetting dynamics were added to the output of the fuel injection pulse width signal to emulate a PFI injector. Engine test were conducted and will be discussed for two cases, the first for the DI injector without wall wetting dynamics and the second for the DI injector with the wall wetting dynamics.

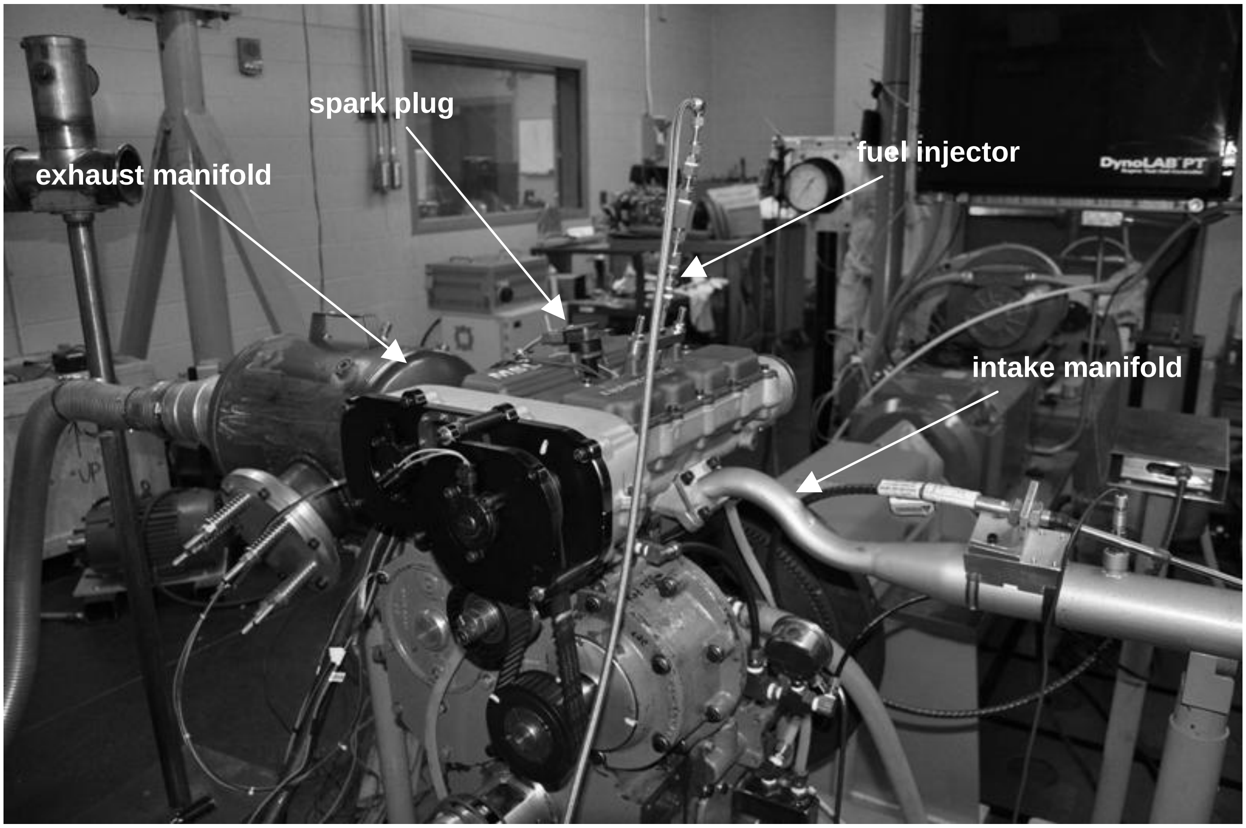

Figure 4-1: Single cylinder test engine shown on engine dyno

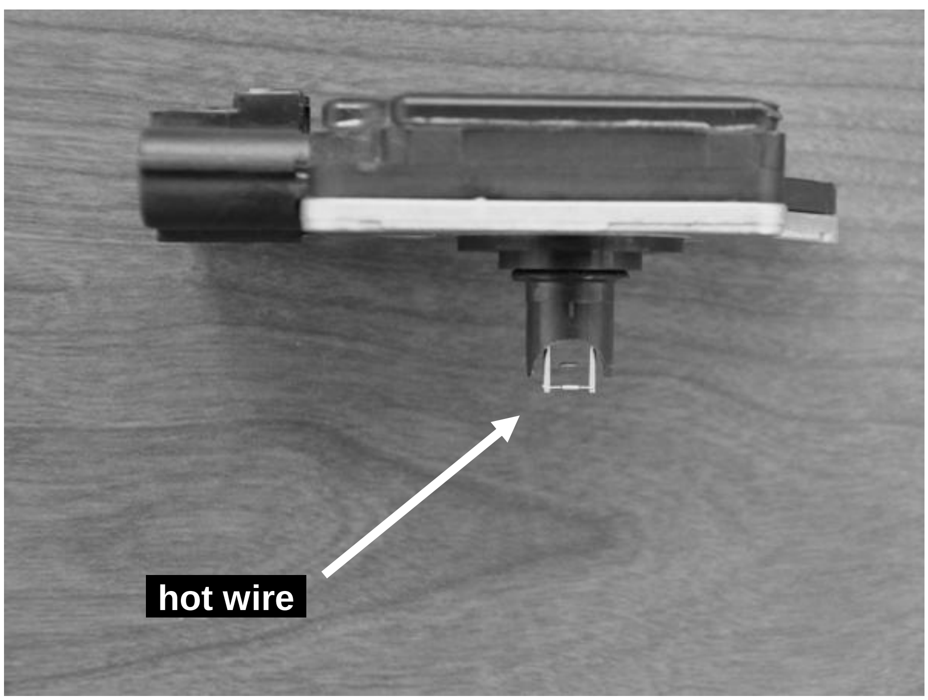

Figure 4-2: MAF sensor hot wire

4.1.1 Mass Air Flow Sensor Modification

The mass air flow sensor (MAF) for this experimental setup was used to measure the quantity of air flowing through the engine throttle and ultimately into the engine cylinder. A "hot-wire" MAF sensor from a 1996 Ford Ranger was modified and installed on the single cylinder engine. The "hot-wire" mass air flow sensor operates by heating a small piece of wire with an electric current that is suspended in a pipe in which the engine's air is flowing. The electrical resistance of the wire increases as the wire temperature increases, which limits electrical current flowing through the closed circuit. When air flows across the wire, the wire cools, decreasing its resistance, and allows more current to flow through the circuit. The amount of current required to maintain the wire temperature is directly proportional to the mass of air flowing past the wire and the integrated circuit converts the current measurement into a voltage signal, which is the output of the MAF sensor. The hot wire of the MAF sensor is shown in Figure 4-2. The MAF sensor was modified from its original 70 millimeter pipe to a smaller 1.5 inch pipe so that it could fit on the upstream side of the intake manifold, adjacent to the engine throttle. Figure 4-3 shows the MAF sensor being placed in the 1.5 inch diameter pipe and the complete assembly is shown in Figure 4-4.

4.1.2 Mass Air Flow Sensor Calibration

Since the MAF sensor output was originally designed to measure the air flow on a much larger engine than the one used in the experimental setup, it had to be calibrated so that its voltage output corresponds to the correct air flow measurement for the single cylinder engine. To accurately determine the amount of air that flows across the MAF sensor, an orifice with a 2 millimeter diameter hole was placed at the beginning of the 1.5 inch diameter pipe that in which the MAF sensor was inserted and sealed. Bernoulli's principle was then used to determine the incompressible steady state flow through the orifice. The pressure difference across the orifice, ΔP, was measured and the steady state output voltage of the MAF sensor was recorded as shown in Table 4-2. From this data, the air flow can be calculated using the following equation [57]

$$Q = CA_2\sqrt{2(P_1 - P_2)/\rho} \tag{94}$$

where

$$C = \frac{C_d}{\sqrt{1-\beta^4}},$$

and C_d is the coefficient of discharge, β is the ratio of orifice hole diameter to pipe diameter, A_2 is the cross-sectional area of the orifice hole, P_1 and P_2 are the upstream and downstream pressures, respectively, and ρ is air density.

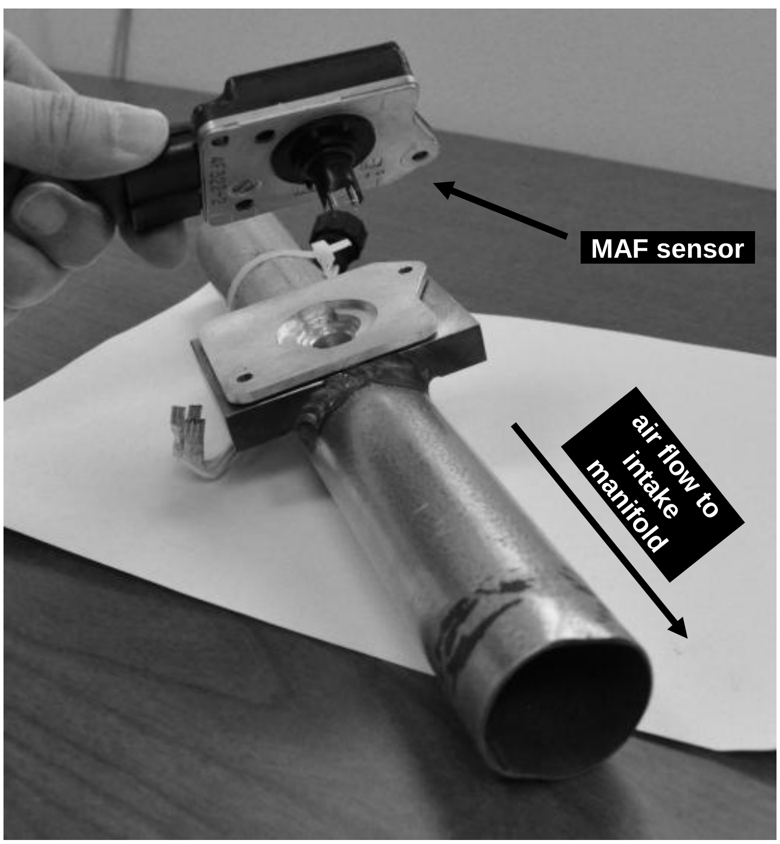

Figure 4-3: MAF sensor being placed in pipe

Figure 4-5 shows the plot of the air flow, calculated using equation (94) and measured by the MAF sensor, and the corresponding sensor output voltage. Due to the large fluctuations in the MAF sensor signal, a low pass filter that averages the signal every engine cycle was used to remove these fluctuations, and this filtered signal was used by the LQ tracking controller. Figure 4-6 shows the setup of the MAF sensor on the single cylinder engine.

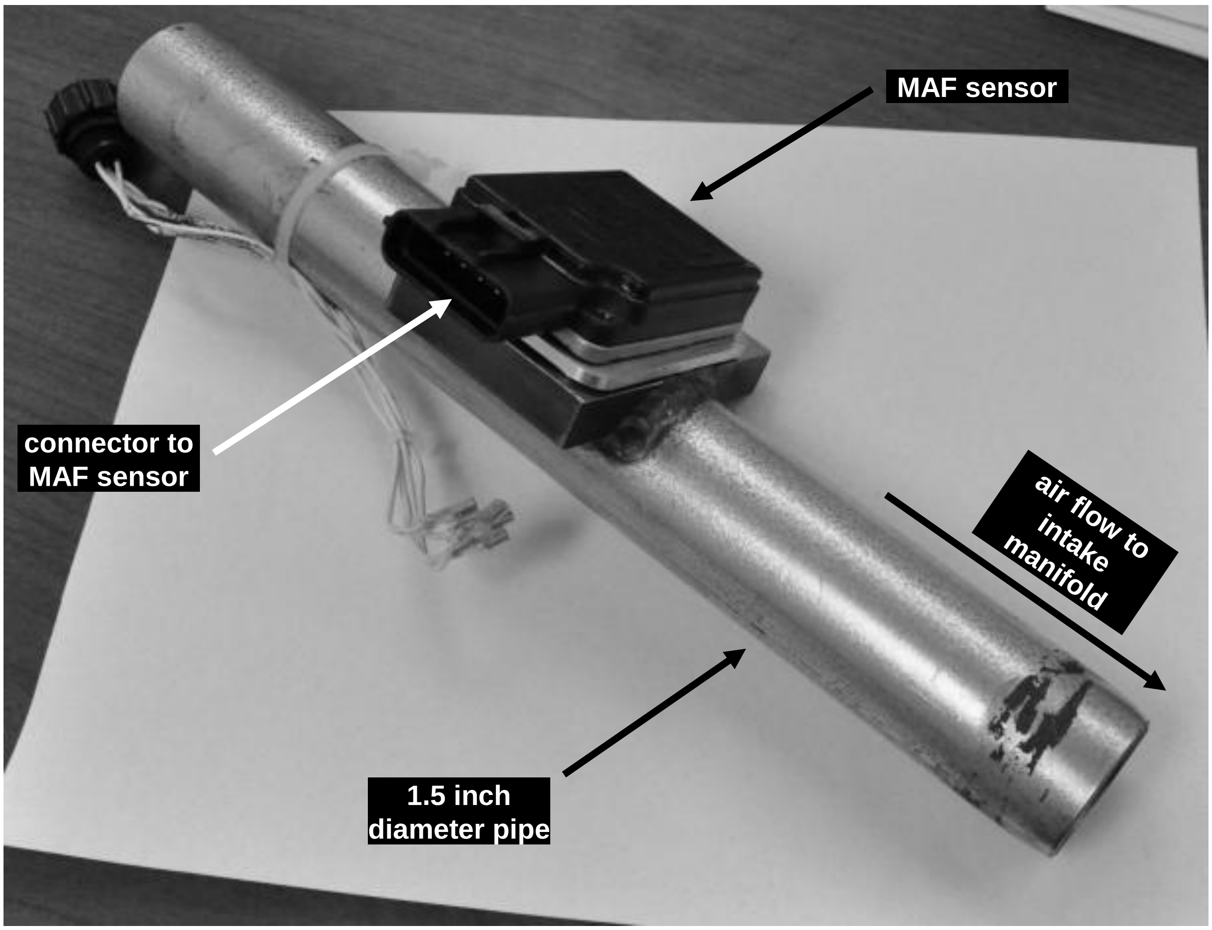

Figure 4-4: MAF sensor assembly

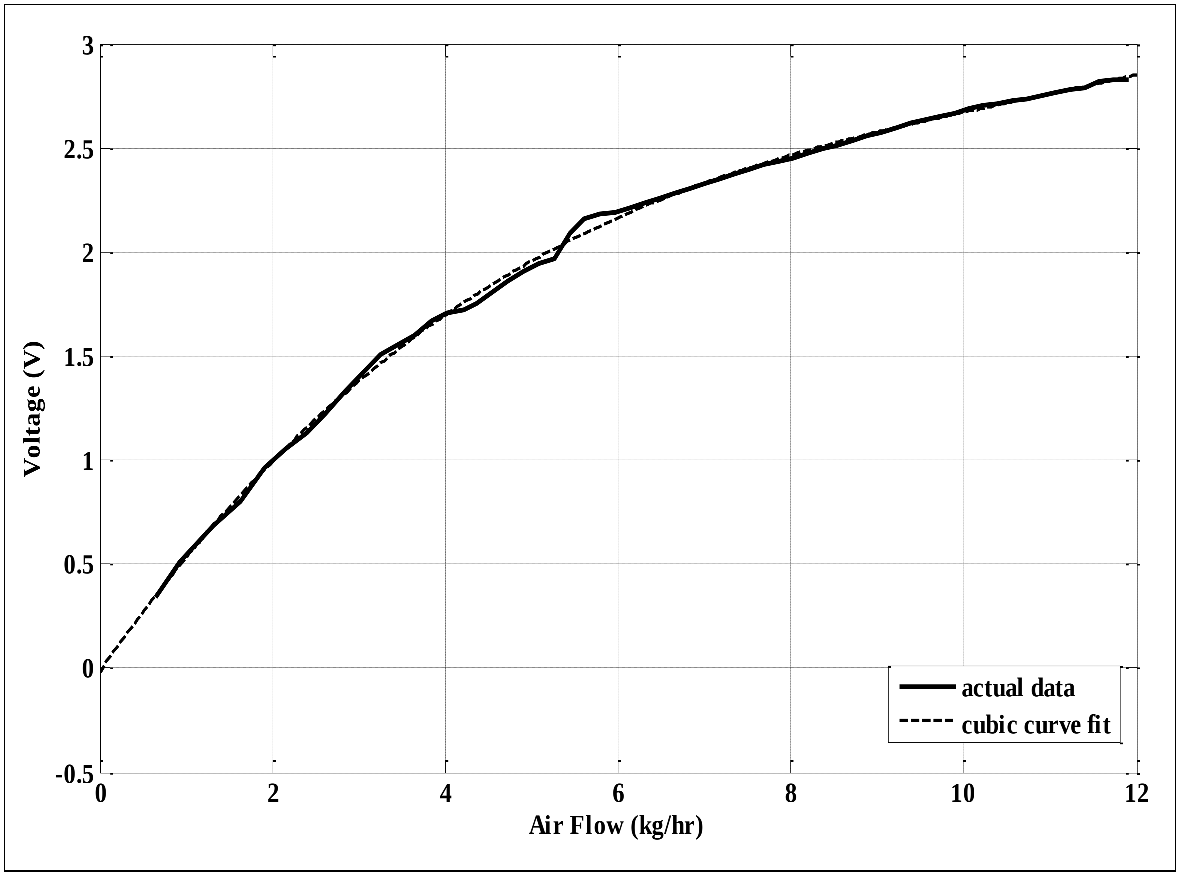

Figure 4-5: MAF air flow vs. voltage

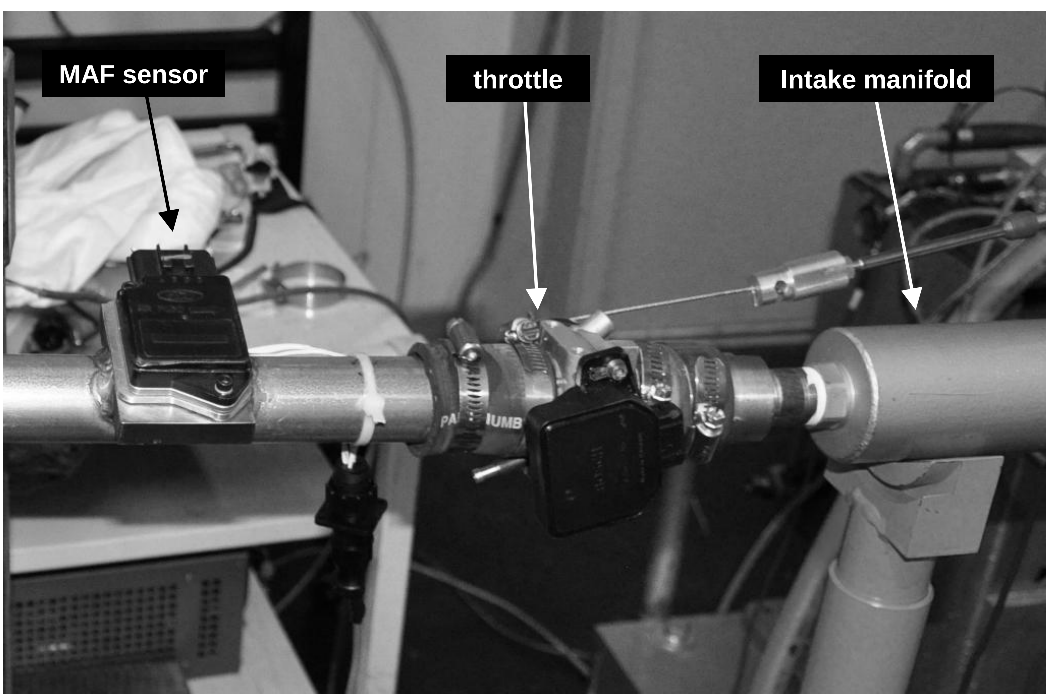

Figure 4-6: MAF sensor setup on single cylinder engine

Table 4-2: MAF sensor calibration table

ΔP (psi)	ΔP (kPa)	Voltage (V)	Flow (kg/hr)
0.5	3.4475	0.341	0.643867413
1	6.89475729	0.506	0.91874886
2	13.78951458	0.689	1.312328
3	20.68427187	0.804	1.6269035
4	27.57902916	0.964	1.9026858
5	34.47378645	1.058	2.1549225
6	41.36854374	1.130	2.391264
7	48.26330103	1.225	2.6161501
8	55.15805832	1.327	2.8324027
9	62.05281561	1.413	3.041933
10	68.9475729	1.506	3.246097
11	75.84233019	1.553	3.4458888
12	82.73708748	1.601	3.6420615
13	89.63184477	1.667	3.8351977
14	96.52660206	1.704	4.0257545
15	103.4213594	1.724	4.214101
16	110.3161166	1.752	4.357047
17	117.2108739	1.806	4.540266
18	124.1056312	1.861	4.7220273
19	131.0003885	1.903	4.9025006
20	137.8951458	1.944	5.081832
21	144.7899031	1.965	5.2601423
22	151.6846604	2.093	5.4375377
23	158.5794177	2.162	5.61411
24	165.474175	2.182	5.78994
25	172.3689323	2.194	5.9650927
26	179.2636895	2.210	6.139631
27	186.1584468	2.234	6.313611
28	193.0532041	2.259	6.4870763
29	199.9479614	2.281	6.660072
30	206.8427187	2.306	6.8326335
31	213.737476	2.330	7.0047965
32	220.6322333	2.354	7.1765885
33	227.5269906	2.377	7.3480387
34	234.4217479	2.399	7.5191717
35	241.3165052	2.417	7.690009
36	248.2112624	2.435	7.8605723
37	255.1060197	2.453	8.030876
38	262.000777	2.476	8.200943
39	268.8955343	2.494	8.370783
40	275.7902916	2.516	8.540413
41	282.6850489	2.539	8.7098465

Table 4-2 (cont'd)

ΔP (psi)	ΔP (kPa)	Voltage (V)	Flow (kg/hr)
42	289.5798062	2.558	8.879092
43	296.4745635	2.577	9.048162
44	303.3693208	2.595	9.217069
45	310.2640781	2.618	9.38582
46	317.1588353	2.633	9.554424
47	324.0535926	2.651	9.722888
48	330.9483499	2.669	9.891222
49	337.8431072	2.687	10.059429
50	344.7378645	2.702	10.22752
51	351.6326218	2.714	10.395497
52	358.5273791	2.725	10.56337
53	365.4221364	2.738	10.731138
54	372.3168937	2.751	10.898809
55	379.211651	2.769	11.066389
56	386.1064082	2.785	11.233883
57	393.0011655	2.791	11.401293
58	399.8959228	2.818	11.568624
59	406.7906801	2.824	11.735876
60	413.6854374	2.831	11.903056

4.1.3 Engine Controller Setup

The engine controller hardware that was used for the engine tests was an Opal-RT HIL engine controller [46]. It is capable of sampling engine sensor signals and updating engine control signals every millisecond, and also has the ability to send and receive crank-angle based signals. For the engine tests, only the engine oxygen sensor and MAF sensor signals are received and used by Opal-RT. Similarly, only the direct injector fuel pulse signal and ignition timing signal are used and sent by Opal-RT to the injector and spark plug, respectively. Similar to the MAF sensor signal, a low pass filter that averages the engine oxygen signal every engine cycle was used to remove the large fluctuations in the oxygen sensor signal. The discretized LQ tracking controller was implemented in Simulink and auto coded into the Opal-RT controller, and all controller matrices and signals were updated every 10 ms, as was the case in the HIL simulations in Section 3.8. Figure 4-7 shows the physical setup of the Opal-RT engine controller.

4.1.4 Data Acquisition System

The data acquisition system used to accurately monitor the engine combustion stability and the status of other engine components was the A&D Technology Inc. Combustion Analysis Software (CAS) real time data acquisition system [58]. The CAS system receives crank angle based signals every crank angle degree and also can receive time based signals every microsecond, if necessary. Figure 4-7 shows the physical setup of the CAS real time data acquisition system.

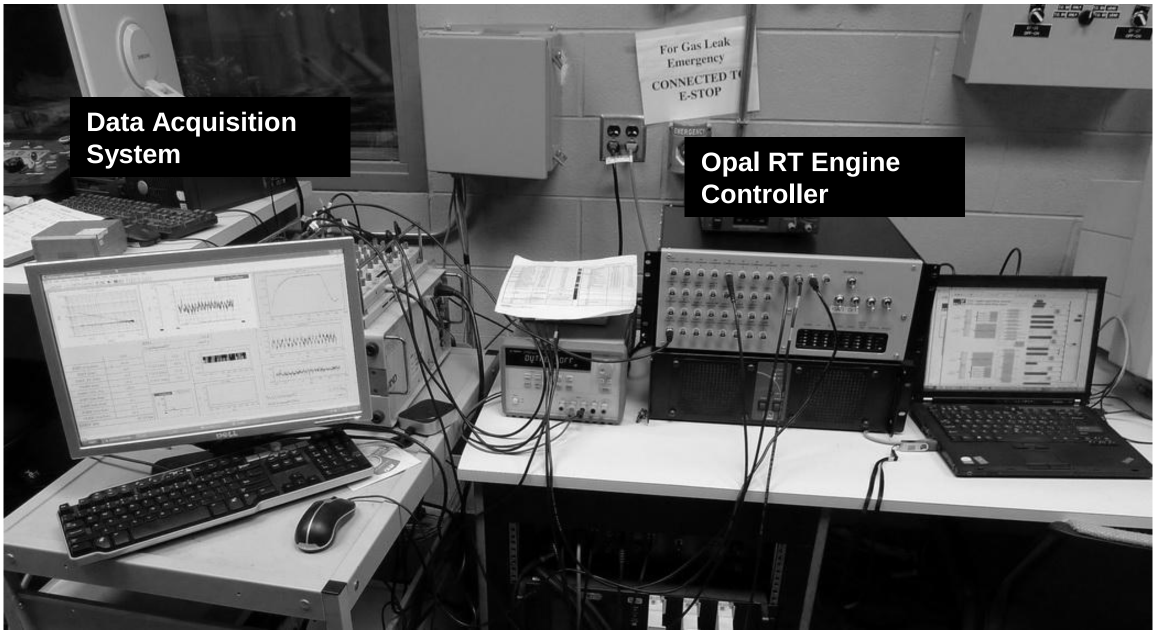

Figure 4-7: Engine controller and data acquisition setup

4.2 Air Flow and Fuel Flow Model Redesign

The model based optimal LQ transient AFR controller was validated in offline Simulink and in real time HIL simulations as shown in Section 3.8. The models used for the intake manifold filling dynamics and throttle plate dynamics were acceptable in simulations but these simplified models were redesigned due to the difference between the model and the physical engine.

First, in simulation the intake manifold filling dynamics were modeled as a first order system with a time constant $\tau_2 = 0.05$ as shown in equation (61). To improve the accuracy of the model of the intake manifold filling dynamics, a step throttle increase of the air flow into the intake manifold was measured by the intake manifold pressure sensor. From this signal, it was observed that the filling dynamics can indeed be approximated by a first order system. Consequently, a more accurate time constant of the physical system was also determined from this pressure signal. It was found that a time constant of $\tau_{\text{intake}} = 0.16$ seconds modeled the filling process more accurately, due to the large intake manifold volume size that was used on the test engine. The validation of the modeled intake manifold filling dynamics in simulation against the intake manifold filling dynamics of the physical engine is shown in Figure 4-8. The raw MAP sensor signal was filtered by taking the average of the lowest 20 pressure values out of the entire 720 values that were obtain by the CAS system every engine cycle.

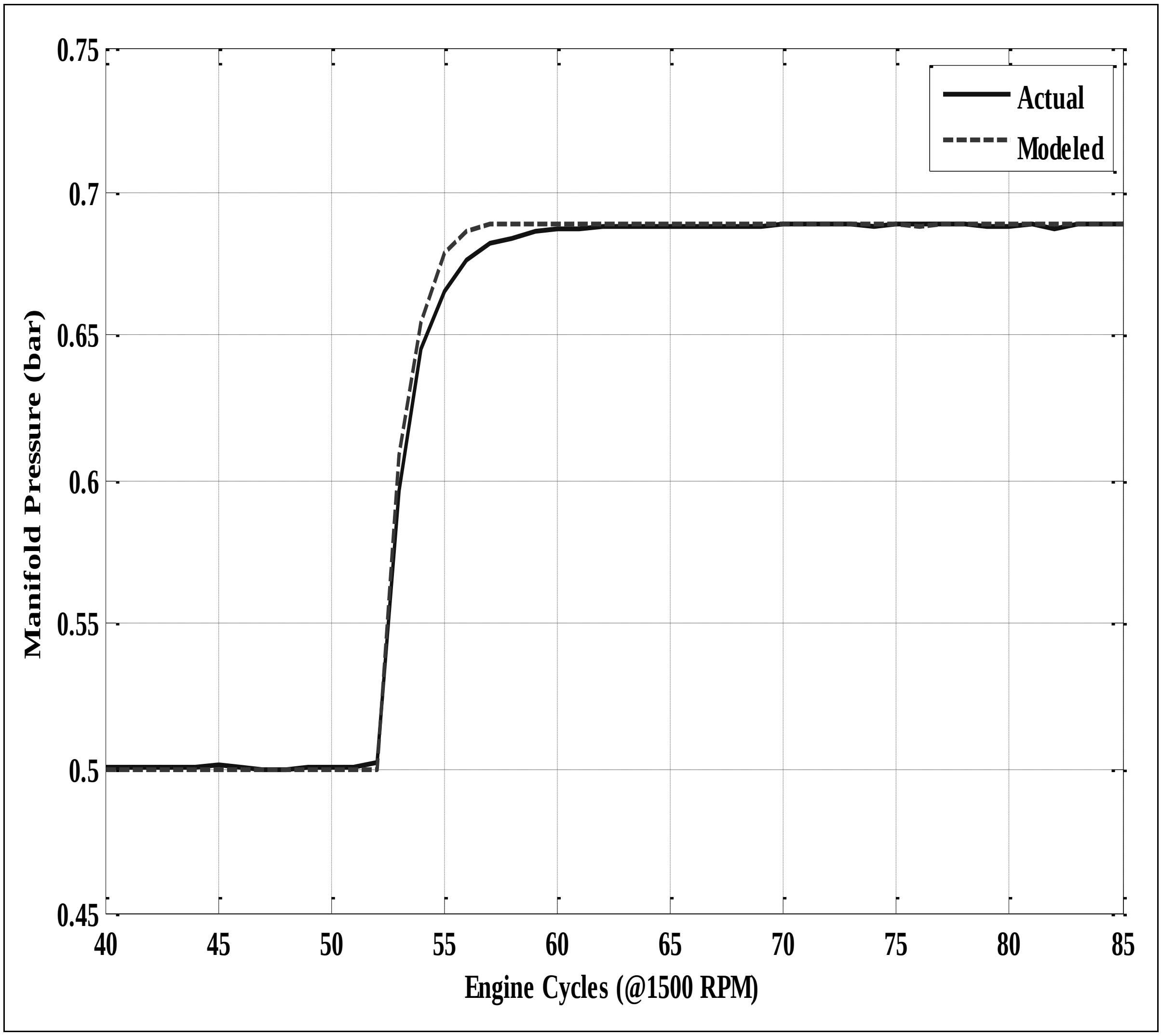

Figure 4-8: Intake manifold filling dynamics model validation

Next, the throttle dynamics that were modeled as a first order system as shown in equation (59) were accurate for simulation only. To emulate a step increase and decrease in the engine air flow on the test engine, a 2-way normally closed solenoid valve was used. A valve splitter was attached to the output side of the 2-way valve, to allow a small manually adjustable amount of air flow to enter the engine when no voltage is applied to the solenoid. When 24 volts was applied to the solenoid, the valve opened allowing a larger amount of air to be added to the small manually adjustable amount, illustrated in Figure 4-9.

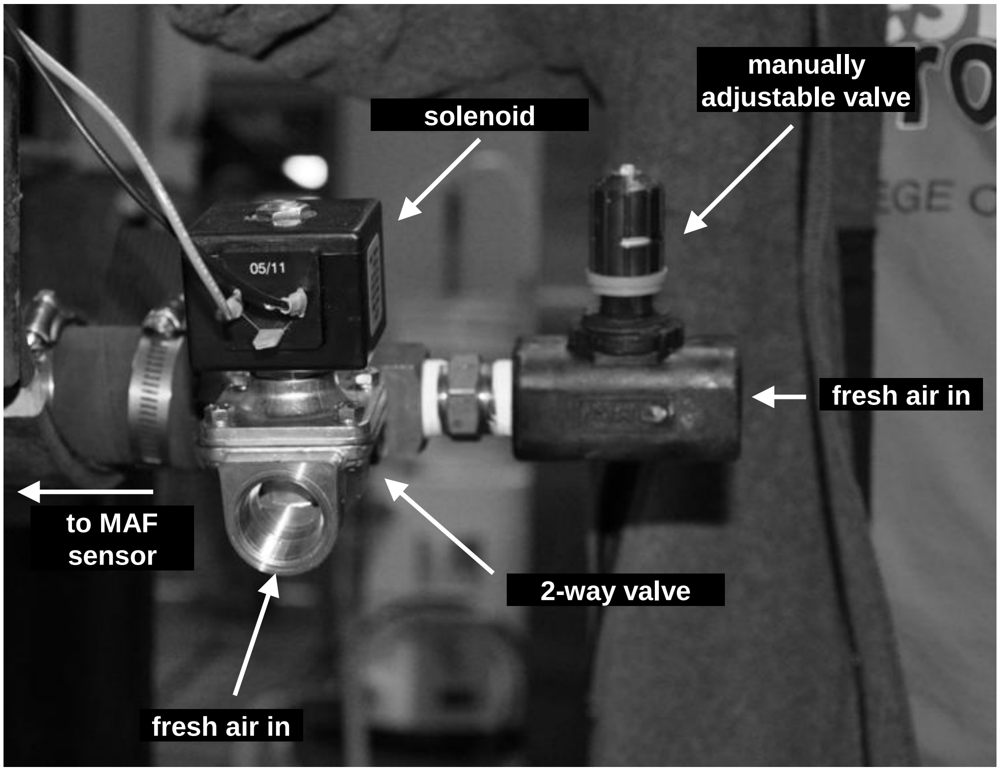

Figure 4-9: Two way solenoid valve setup on engine

Since the response of the solenoid is very fast when powered, this emulates a step increase of air flow into the engine. In order to model the aforementioned physical process of opening the throttle to increase and decrease the air flow, the first order model described in equation (59) was redesigned. A second order transfer function of the form below was used,

$$\omega_{throttle} = \frac{\omega_n^2}{s^2 + 2\varsigma\omega_n s + \omega_n^2}\omega_{air} \tag{95}$$

where the maximum percent overshoot and settling time are defined as,

$$OS\% = \exp\left(-\frac{\pi\varsigma}{\sqrt{1-\varsigma^2}}\right) \tag{96}$$

$$T_s = \frac{4}{\varsigma\omega_n}. \tag{97}$$

The values of ω_n and ς were chosen such that the transfer function very closely models the physical system. The validation of the modeled dynamics in simulation versus the physical system is shown in Figure 4-10.

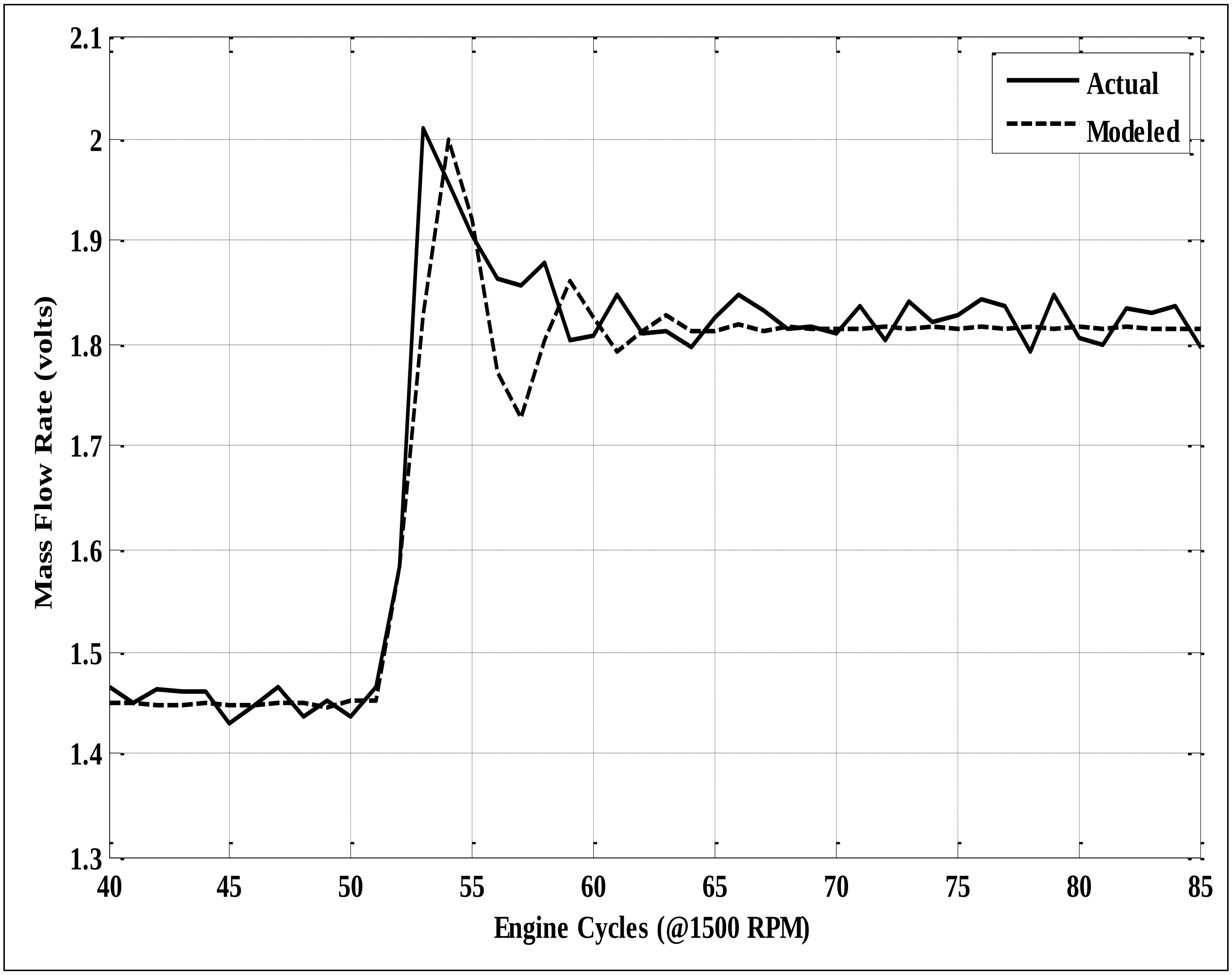

Figure 4-10: Valve dynamics model validation

4.3 State Estimator Design

Recall that the optimal control used in the LQ tracking controller given in equation (86) requires the state *x*, which is used as feedback from the estimated fueling dynamics. For the DI injector case, it is assumed that the state *x* can be obtained from the unitary gain first order transfer function that approximates the fuel injection delay. For the case when wall wetting dynamics are added to the output of the injector fuel pulse width, a state estimator is designed to obtain state information in real-time from the available measurements. The available measurements are the MAF sensor, fuel injection signal, and oxygen sensor.

Recall the linear, time-invariant system described in equation (65) that models the wall wetting dynamics of a PFI injector and the fuel injection delay. A *Luenberger state observer* design [42] is used to estimate the states of (65) in real time and has the following form,

$$\begin{aligned} \hat{x}_{k+1} &= A\hat{x}_k + Bu_k + L(\tilde{y} - \hat{y}) \\ \hat{y}_k &= C\hat{x}_k \end{aligned} \tag{98}$$

where matrix L is chosen such that the estimation error goes to zero as time goes to infinity. The estimation system equation can also be rewritten as,

$$\begin{aligned} \hat{x}_{k+1} &= \left(A - LC\right)\hat{x}_k + \begin{bmatrix} B & L \end{bmatrix} \begin{bmatrix} u_k \\ y_k \end{bmatrix} \\ \hat{y}_k &= C\hat{x}_k \end{aligned} \tag{99}$$

and the error between the actual state x_k and the estimated state $\hat{x}_k$ is governed by the following equation,

$$\begin{aligned} e_{k+1} = x_{k+1} - \hat{x}_{k+1} &= Ax_k + Bu_k - (A - LC)\hat{x}_k - \begin{bmatrix} B & L \end{bmatrix} \begin{bmatrix} u_k \\ y_k \end{bmatrix} \\ &= (A - LC)(x_k - \hat{x}_k) = (A - LC)e_k \end{aligned} \tag{100}$$

By choosing the estimation gain matrix L as,

$$L = \begin{bmatrix} 2.8579 \\ 2.6013 \end{bmatrix} \tag{101}$$

the eigenvalues of the error system matrix have magnitude less than unity and this guarantees that the state estimation error e_k will become zero as time goes to infinity. Figure 4-22 shows the architecture of LQ tracking controller with the state estimator.

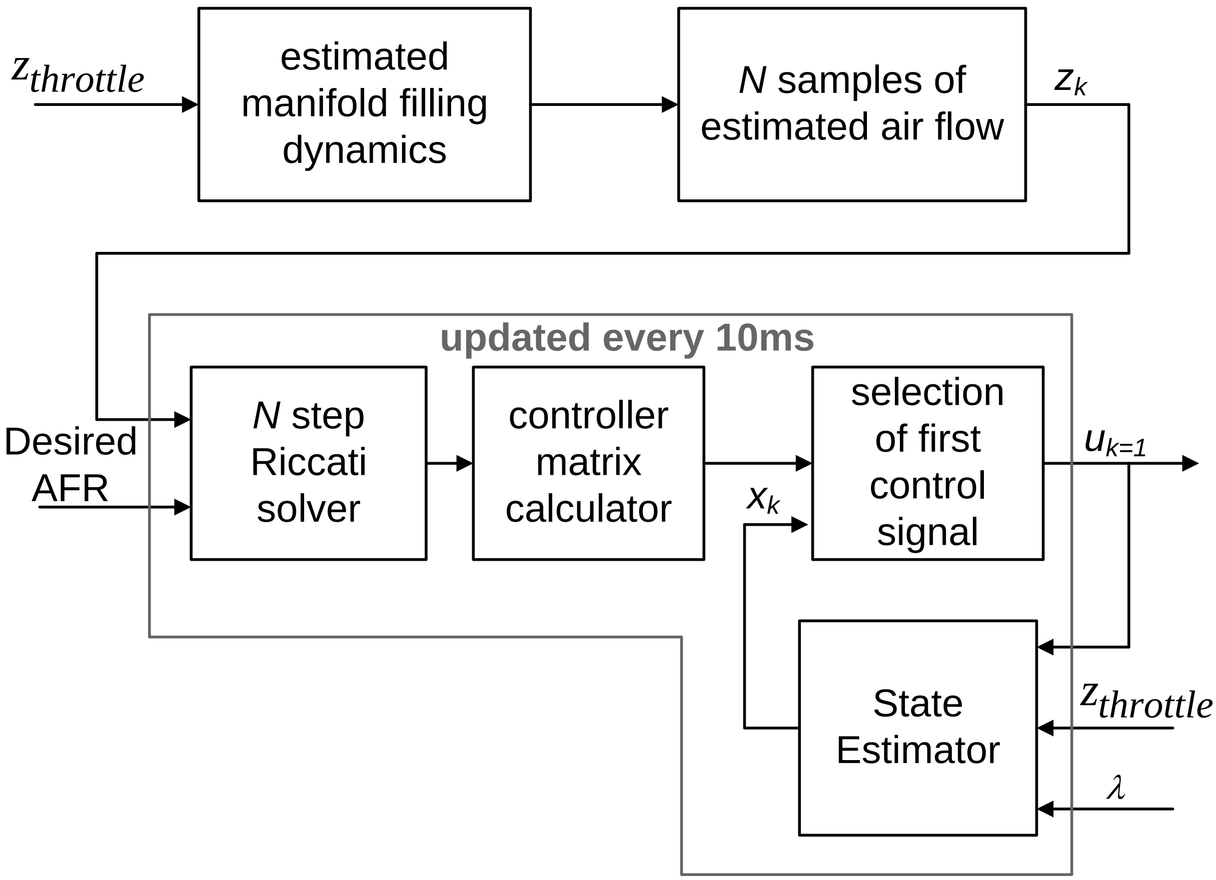

Figure 4-11: LQ tracking controller with state estimator

4.4 Engine Test Results of LQ Transient Air-to-fuel Ratio Controller for DI Injector

The engine test results for the LQ transient AFR controller will be discussed and presented for the first case, which is for the DI injector without wall wetting dynamics added to the control output of the injector fuel pulse. Several tests were conducted to show the ability of the controller to minimize deviations of the AFR from a desired value during engine transients. For all engine tests, a fixed engine speed of 1500 RPM was used and only gasoline was injected.

Two engine transients were used: an increase in air flow into the cylinder and a decrease in air flow, resulting in an increase and decrease in both the engine load and IMEP, respectively. The increase and decrease of intake manifold pressure and engine IMEP on the single cylinder engine are shown in Figure 4-12. Notice that the change in MAP is close to 0.2 bar and the change in IMEP is close to 2 bar. Therefore, this change represents a significant engine transient very well and was achieved by applying 24 volts to the solenoid valve discussed in Section 4.2.

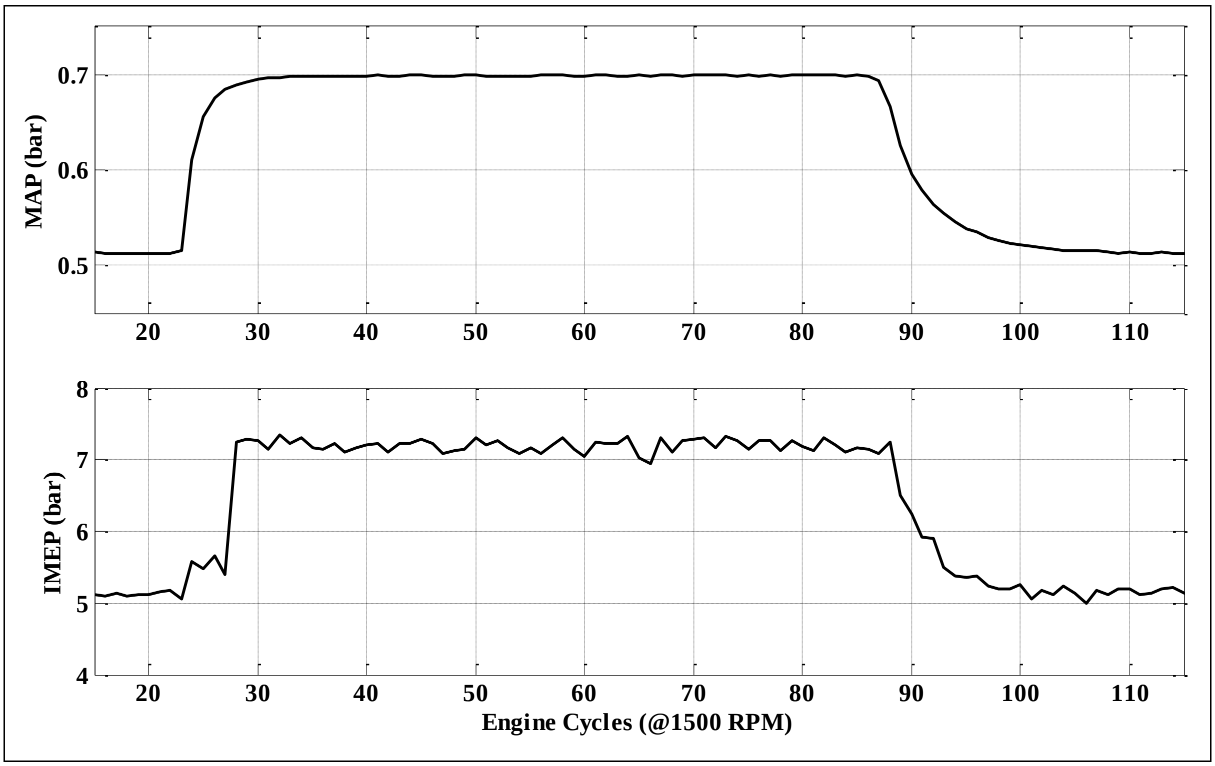

Figure 4-12: Engine transients for MAP and IMEP

4.4.1 LQ Tracking Feed Forward Control Results

To begin the engine tests, the selection of the weighting matrix *R* on the performance of the LQ tracking controller on the physical engine was investigated. As discussed in Section 3.8.5, when *R* is relatively large, the tracking performance of the controller decreases significantly. Five values of *R* were chosen for the different engine tests that applied a step increase and decrease in the air flow that is tracked by the controller. The maximum deviation of the AFR from stoichiometry for the different values of R is shown Figure 4-21. It can be seen when $R = 10^{-6}$ the maximum error for an increase (step open) and decrease (step close) in the air flow is 8.02% and 8.33%, respectively. Thus, the best choice is $R = 10^{-6}$, and this value will be used for all simulations. The AFR of the engine for the increase and decrease in air flow is shown in Figure 4-14 and Figure 4-15, respectively.

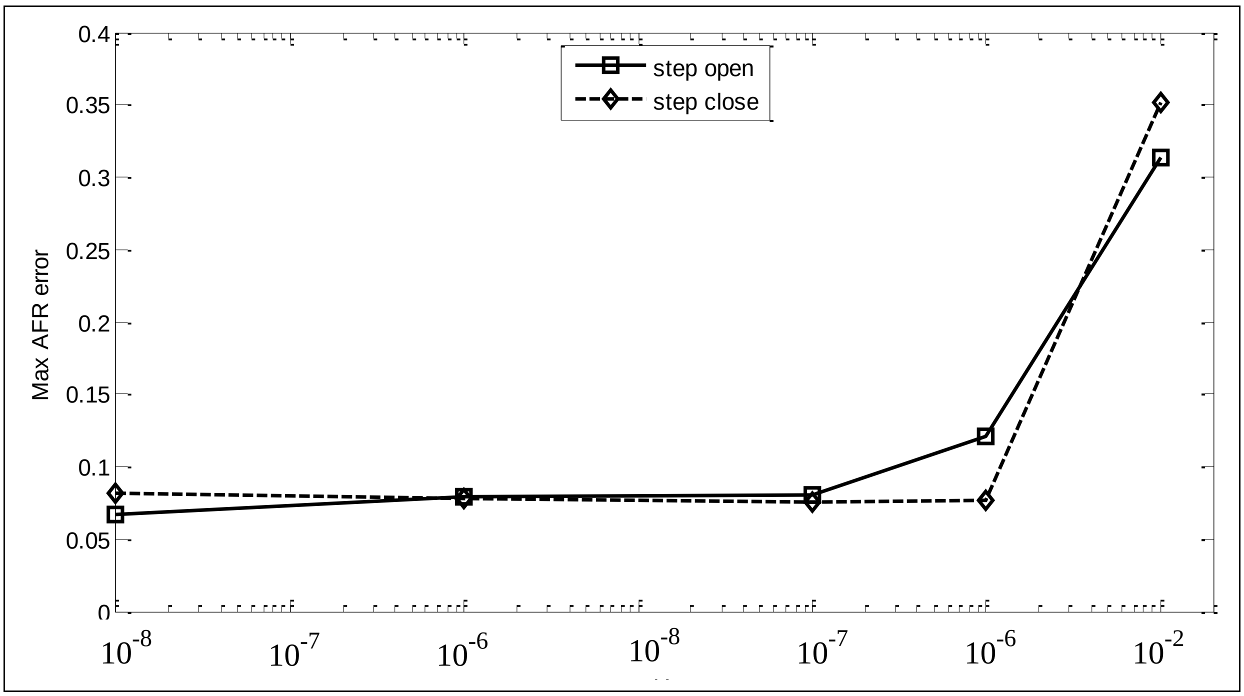

Figure 4-13: Maximum AFR error for different values of R

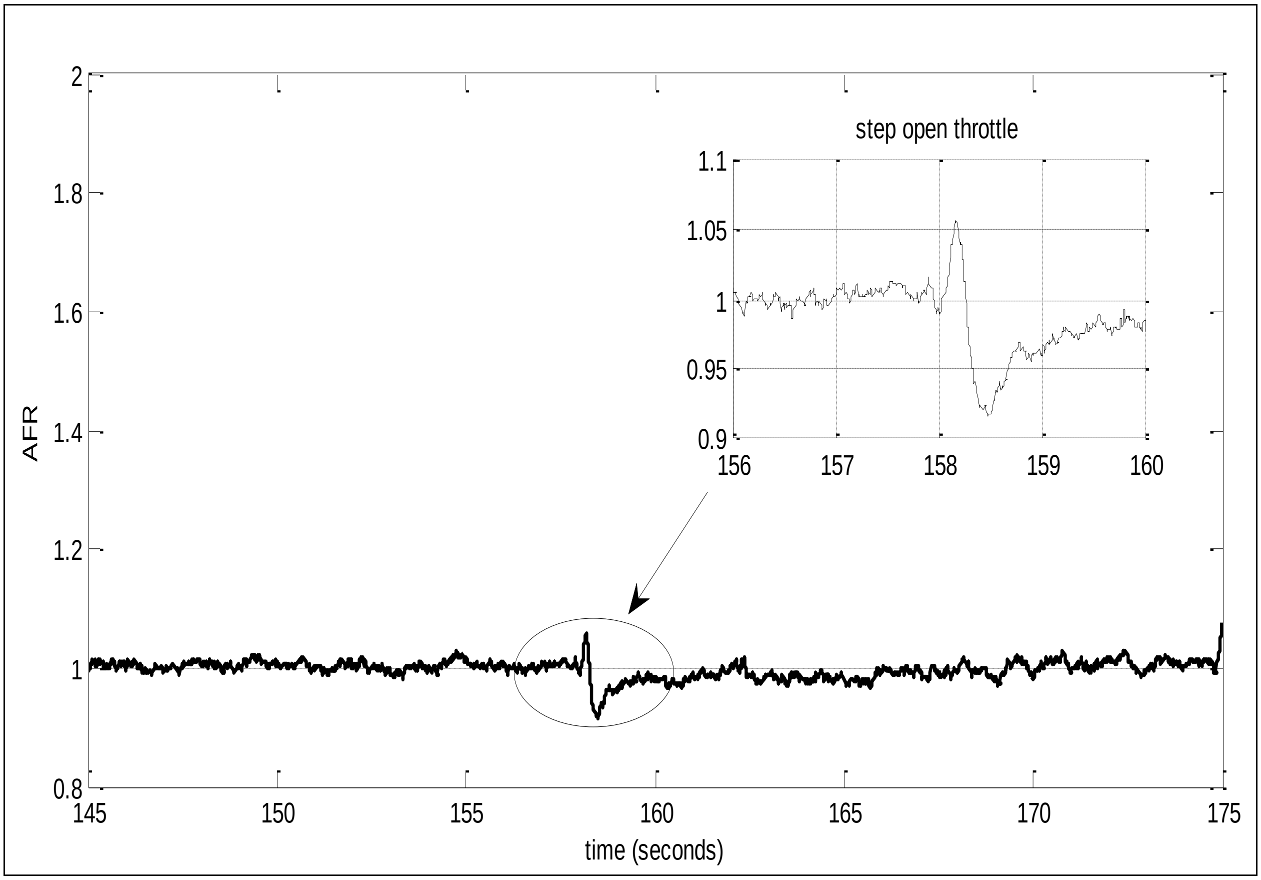

Figure 4-14: Step increase in engine air flow

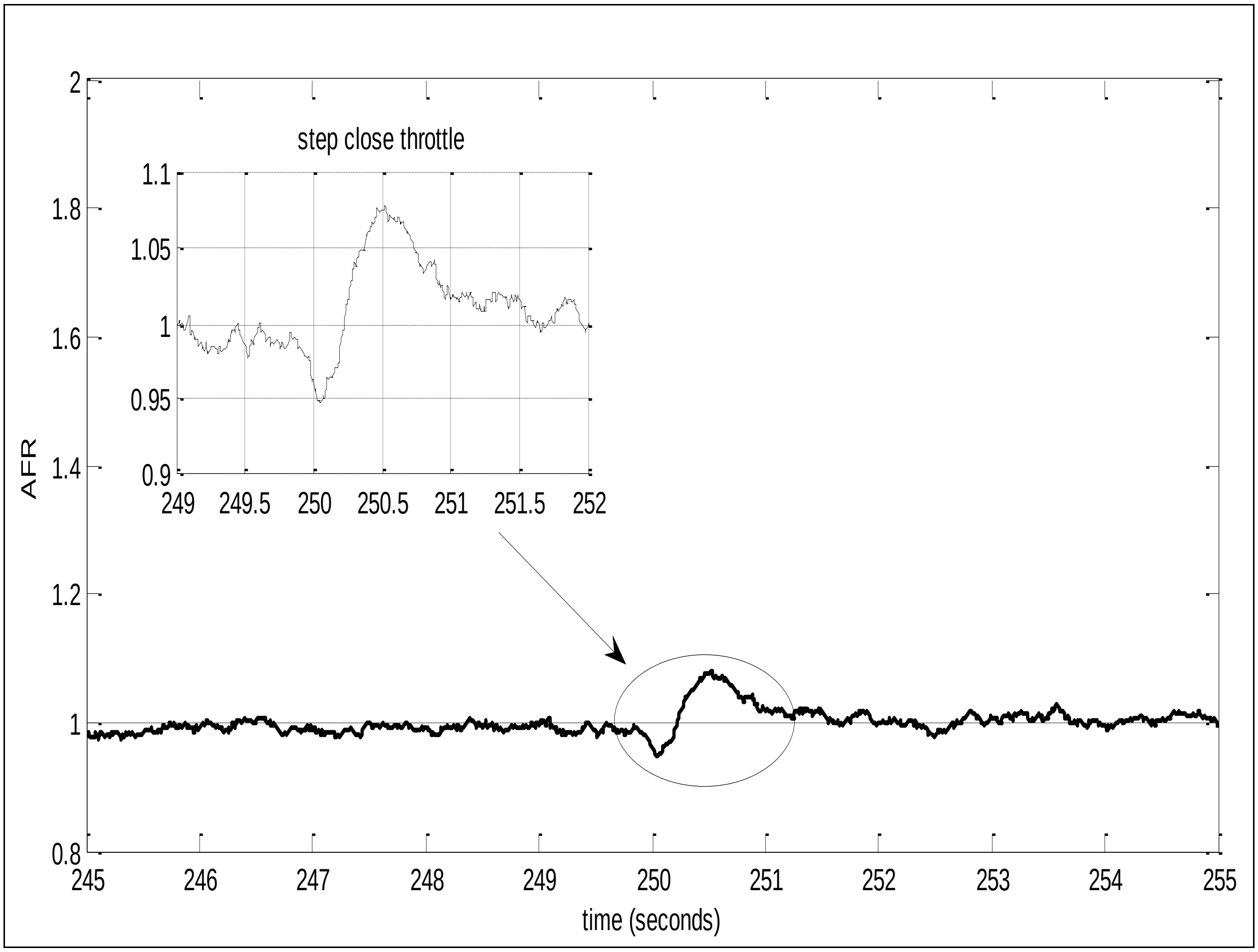

Figure 4-15: Step decrease in engine air flow

The next two engine tests were conducted for a reference AFR of 0.925 and 1.075, and the same step decrease in the air flow was used, as shown in Figure 4-16 and Figure 4-17. Notice the LQ tracking controller can maintain the AFR deviation from the desired value to less than 6% and 8% for reference AFR 0.925 and 1.075, respectively.

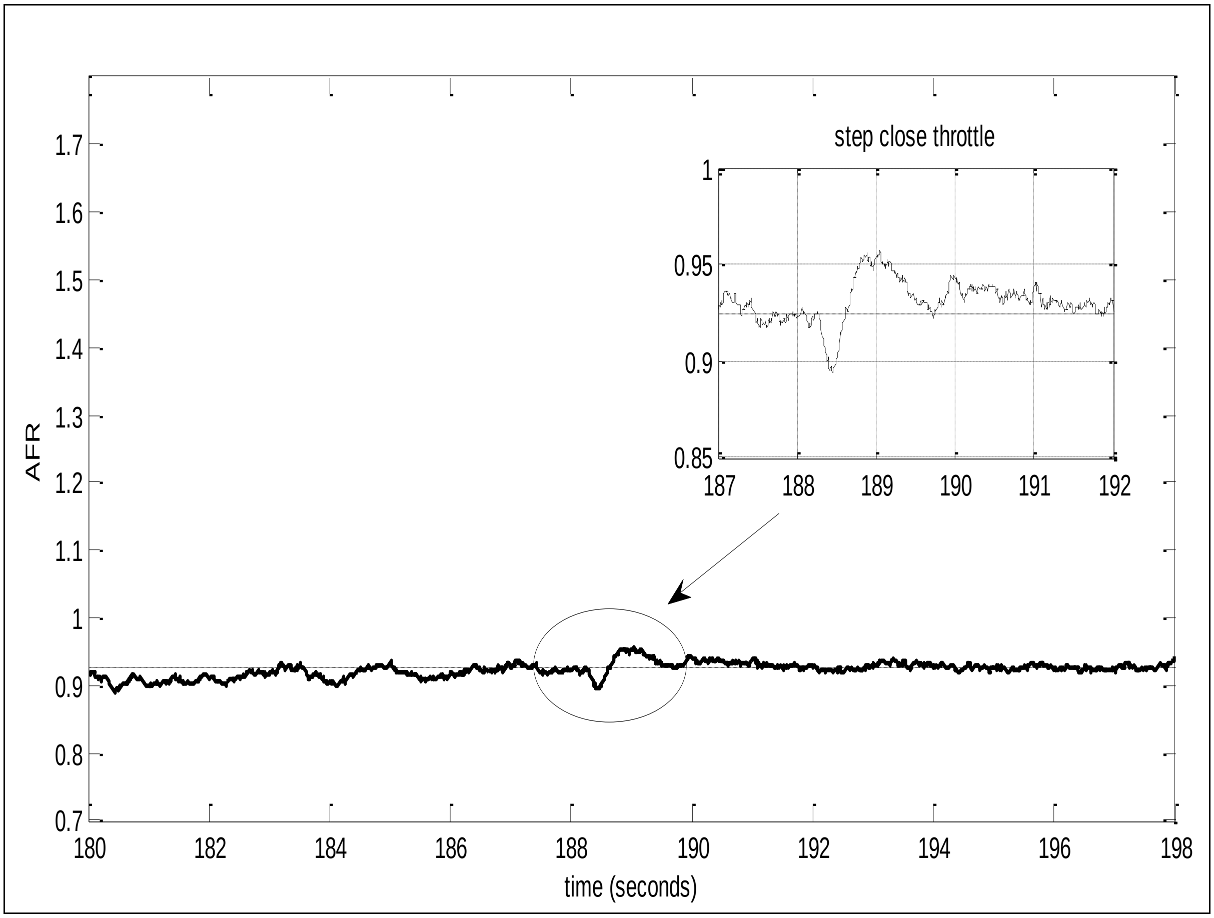

Figure 4-16: Step decrease of LQ tracking controller with reference AFR = 0.925

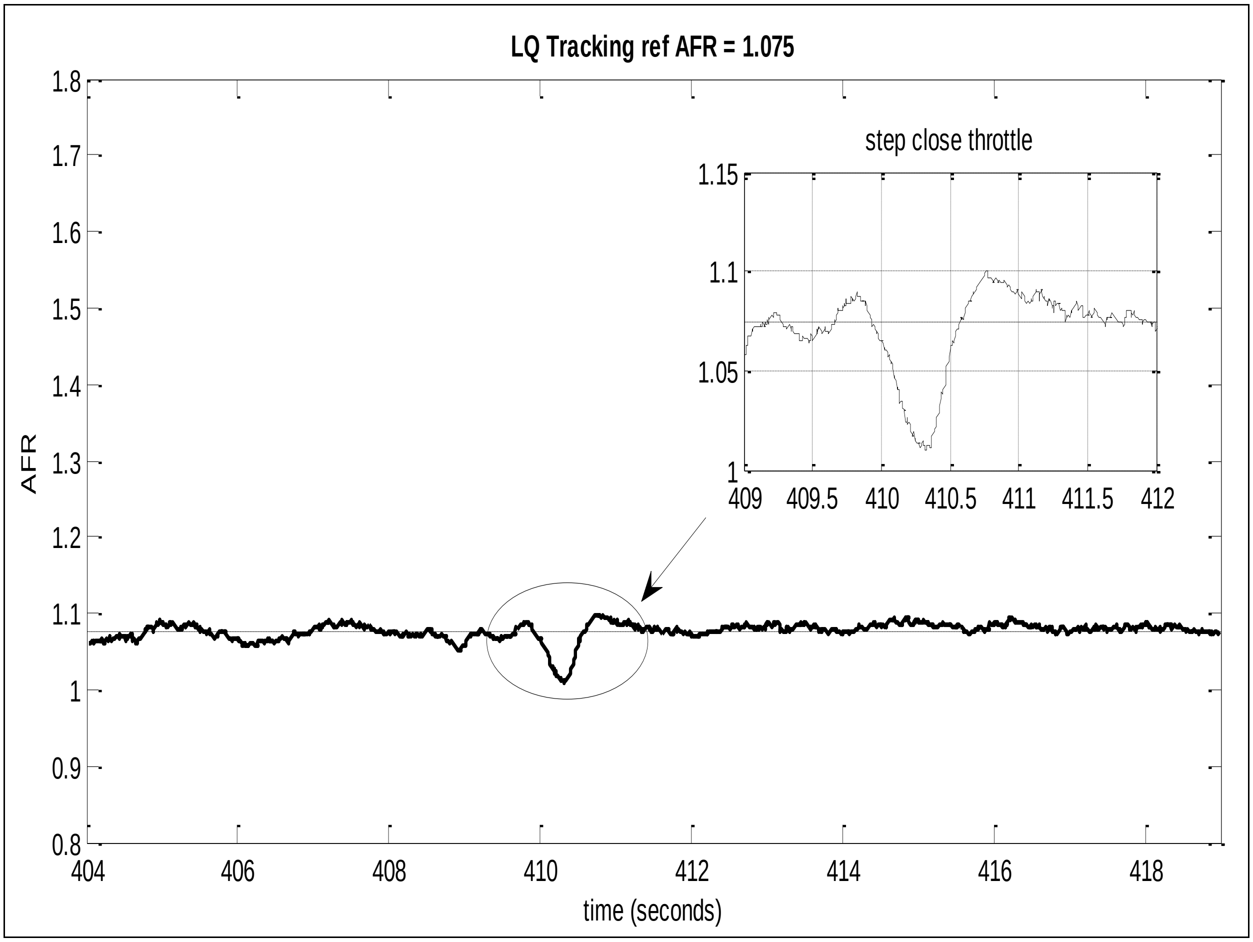

Figure 4-17: Step decrease of LQ tracking controller with reference AFR = 1.075

4.4.2 Inverse Fueling Feedfoward Control Results

Several engine tests were conducted to compare the LQ tracking controller to the conventional inverse fueling feedforward control. This controller was implemented in the Opal-RT and was sampled every 10 ms, similar to the LQ tracking controller. For this case, where the DI injector is used without the wall wetting dynamics added to the output of the fuel injection pulse, the schematic for the inverse fueling feedforward controller is shown in Figure 4-18.

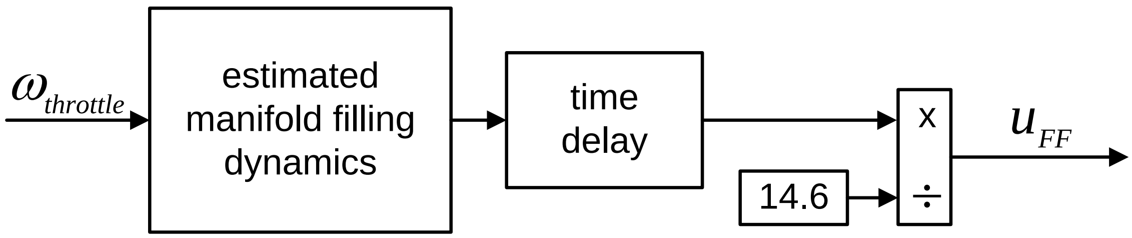

Figure 4-18: Schematic of inverse fueling feedforward controller for DI injector

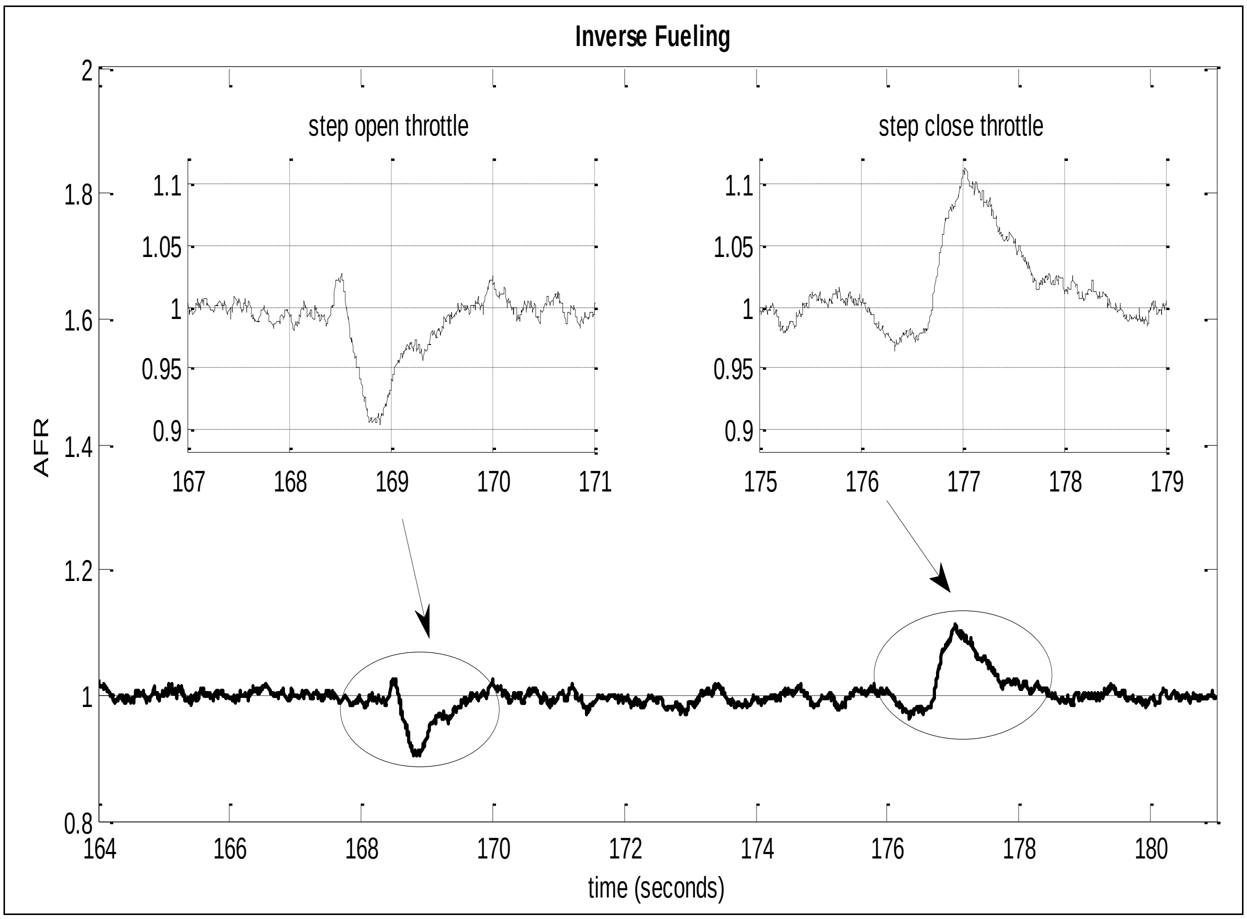

Figure 4-19: AFR response of inverse fueling feedforward controller

The engine tests that were conducted for the inverse fueling were the same as those conducted for the LQ tracking controller, where the reference AFR was stoichiometry. The AFR response of the inverse fueling feedforward controller is shown in Figure 4-19. It can be seen that the deviation of the AFR from stoichiometry is 9.03% and 10.4% for the step increase and decrease in air flow, respectively.

4.4.3 LQ Tracking Feed Forward Control with PID Feedback Control Results

In conventional AFR control systems, both feedforward and feedback control is used. The LQ tracking controller that was implemented as a feedforward control showed acceptable performance for the DI injector, but a feedback controller was added with hopes of further improving the performance of the AFR system.

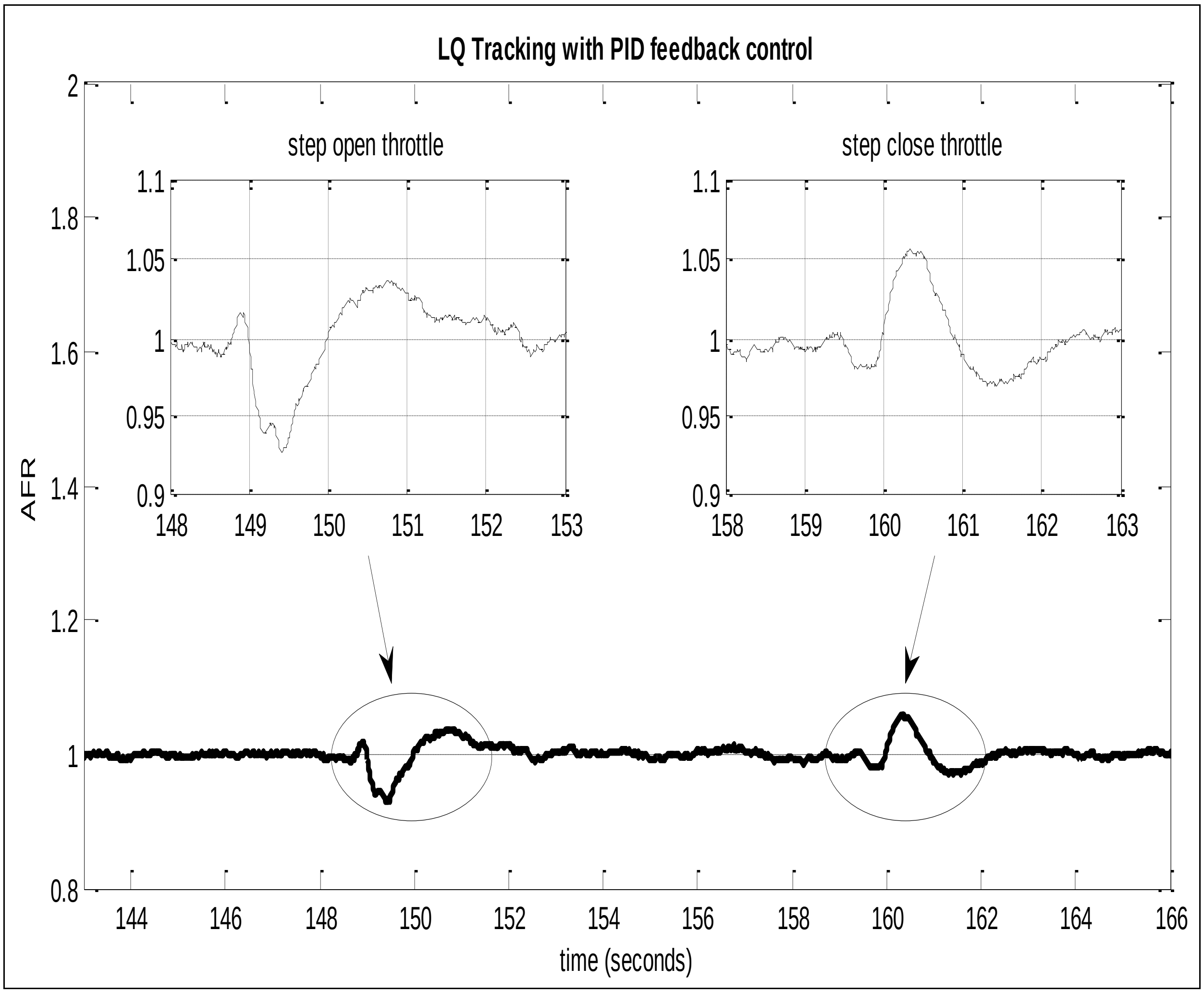

Figure 4-20: AFR response of LQ tracking with PID feedback control

K_P	0.005
K_I	0.0001
K_D	0.001

Table 4-3: PID feedback control gains used for engine tests

A PID controller that uses the oxygen sensor signal as feedback was designed and implemented with the LQ tracking controller. The controller gains were tuned online such the system maintained stability, with very little oscillations, and the transient response was acceptable. The PID gains that were used for the engine tests are shown in Table 4-3. The response of the AFR when a step increase and decrease in air flow were applied is shown in Figure 4-20. Notice that the AFR deviation from stoichiometry for the step increase and decrease in air flow is 7.22% and 5.71%, respectively. This is a significant improvement of the AFR response when the PID feedback controller is added to LQ tracking feedforward control. Although the reduction in the AFR deviation from stoichiometry was achieved by added the PID feedback controller, the settling time was slightly increased. Table 4-4 shows the performance comparison of the LQ tracking controller, inverse fueling feedforward controller, and LQ tracking control with PID feedback control.

	Maximum AFR Deviation		Settling Time	
	step increase	step decrease	step increase	step decrease
LQ Tracking	8.02%	8.33%	1.526 sec	1.699 sec
Inverse Fueling	9.03%	10.4%	1.753 sec	2.193 sec
LQ Tracking w/PID	7.22%	5.71%	2.415 sec	2.308 sec

Table 4-4: Comparison of controllers for stoichiometric reference AFR

4.5 Engine Test Results of LQ Transient Air-to-fuel Ratio Controller for PFI Injector

The engine test results for the LQ transient AFR controller discussed in Section 4.4 were for a DI injector without wall wetting dynamics added to the control output of the injector fuel pulse. In this section similar engine test will be presented and discussed for a DI injector with wall wetting dynamics added to the control output of the injector fuel pulse. These dynamics were added due to the absence of a physical PFI injector on the single cylinder engine. For all engine tests, a fixed engine speed of 1500 RPM was used and only gasoline was injected. The engine transients that were used were the same as described in Section 4.4.

4.5.1 LQ Tracking Feed Forward Control Results

For the first engine test for the LQ tracking feedforward controller, a desired AFR of stoichiometry was chosen. The wall wetting dynamics for a PFI injector were chosen as

$$\frac{\omega_{PFI\_E}(s)}{\omega_{PFI}(s)} = \frac{\alpha s + 1}{\beta s + 1}, \tag{102}$$

where α = 0.5 and β = 0.8, and were added to the control output of the injector fuel pulse. A step increase and decrease in the air flow were applied, and the results are shown in Figure 4-21. The LQ tracking controller maintains the deviation of the AFR during the step increase and decrease to less than 7.56%. Interestingly, the deviation of the AFR during the step decrease in air flow is very minimal, at less than 2.9%. Note that these results were using the fully known state feedback x, and without state estimation discussed in Section 4.3.

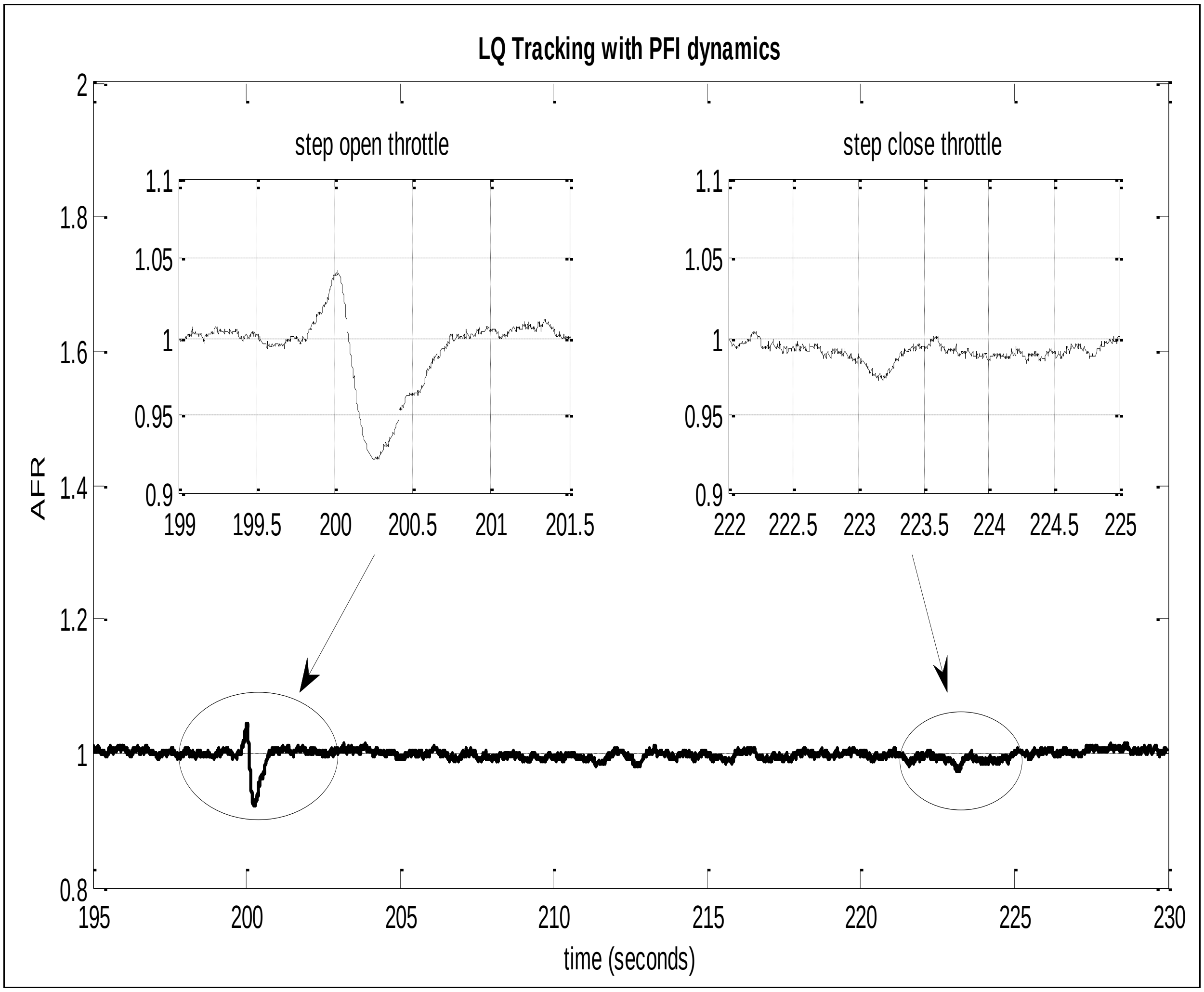

Figure 4-21: LQ tracking without state estimator for stoichiometric AFR

Now consider the state estimator design that was described Section 4.3. Engine tests were conducted using the state estimator that obtained the states from the available measurements, i.e. MAF sensor, fuel injection signal, and oxygen sensor signal. The LQ tracking controller used these estimated states, and all of the following engine test were conducted using the state estimator. A step increase and decrease in the air flow were applied and the results are shown in Figure 4-22. The LQ tracking controller maintains the deviation of the AFR during the step increase and decrease to less than 8.5%. Similar to the case when state estimation was not used, the deviation of the AFR during the step decrease in air flow is very minimal, at less than 3.5%.

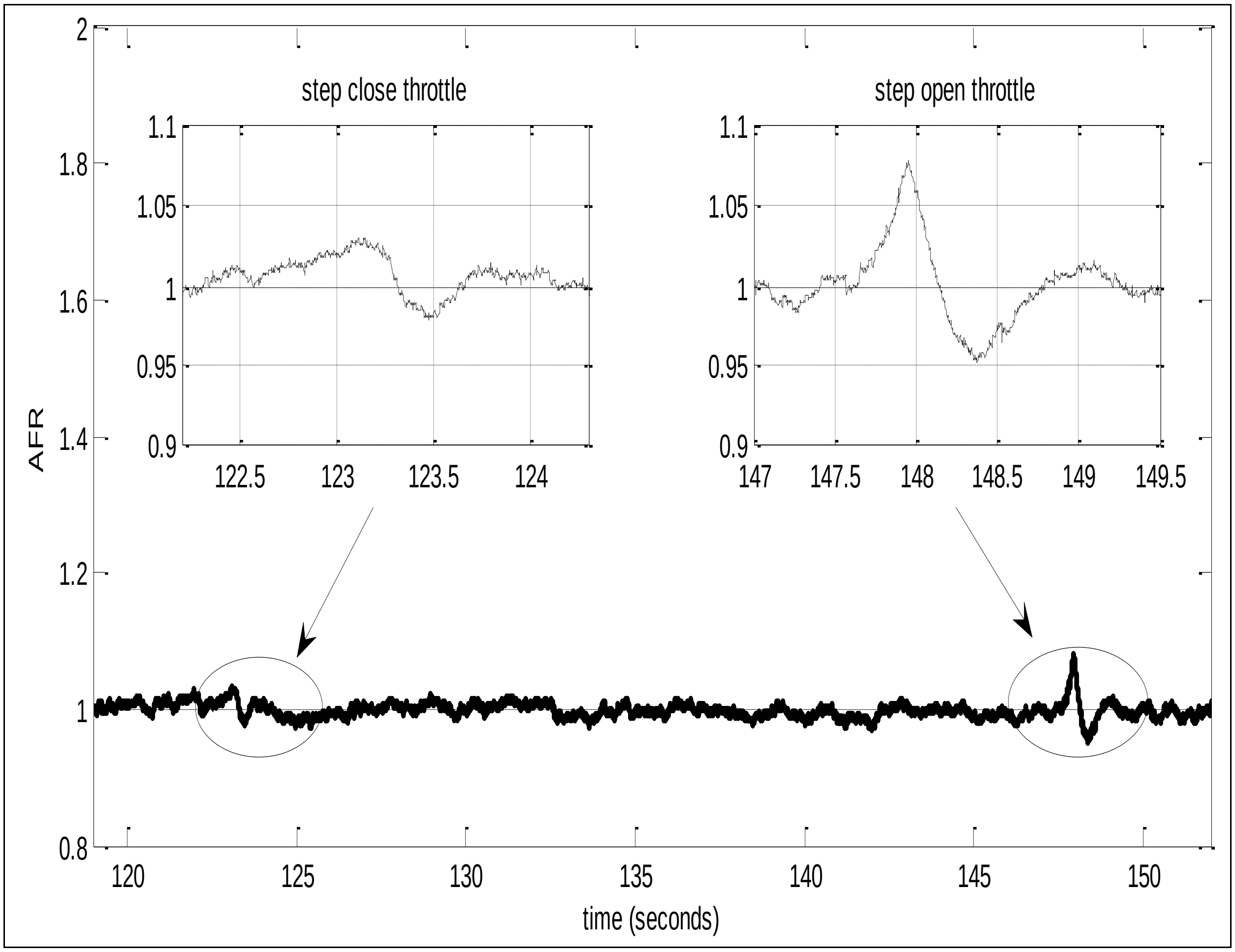

Figure 4-22: LQ tracking controller with state estimator for stoichiometric AFR

The next engine tests were conducted for a reference AFR of 0.925 and 1.075, and the same step increase and decrease in the air flow was used, as shown in Figure 4-23 and Figure 4-24. Notice the LQ tracking controller can maintain the AFR deviation from the desired value to less than 7.5% and 6% for reference AFR 0.925 and 1.075, respectively.

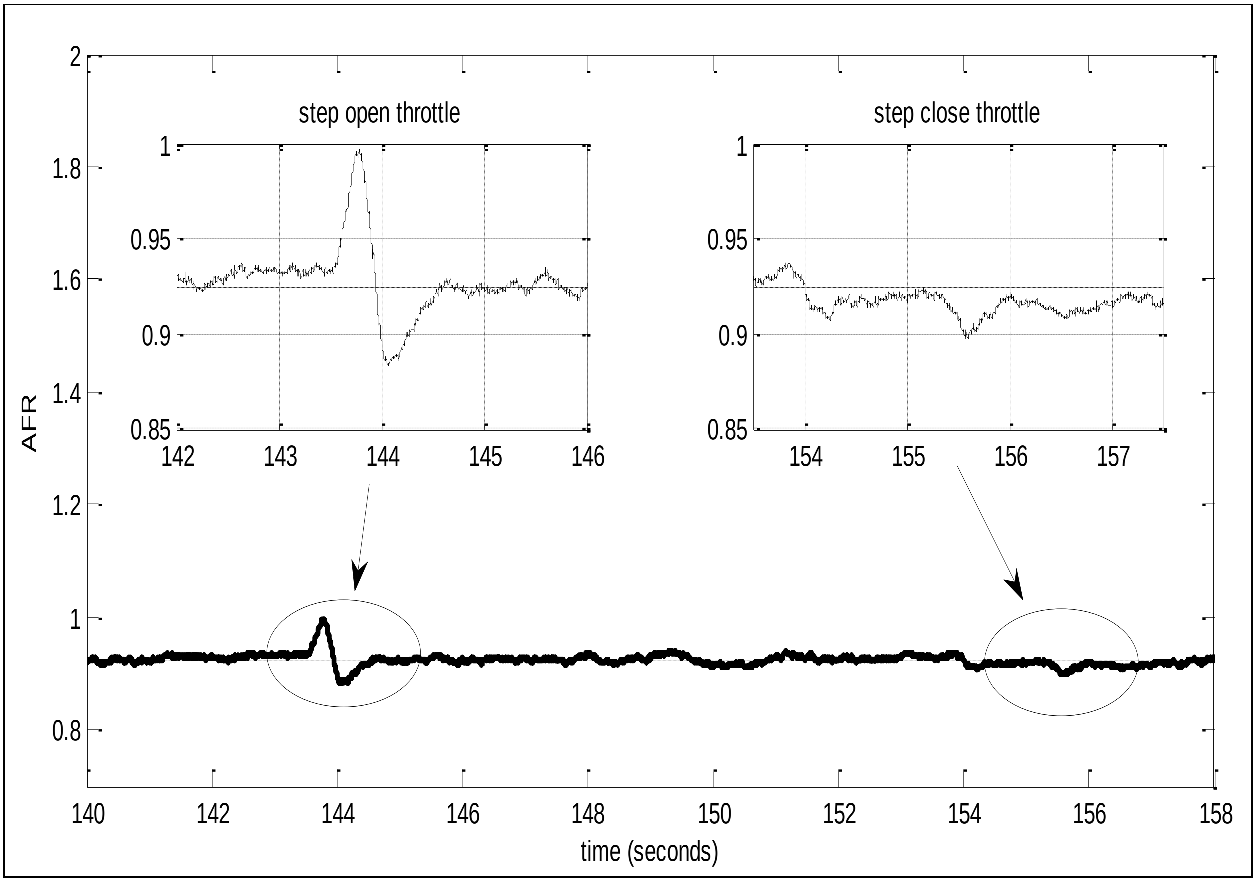

Figure 4-23: Response of LQ tracking controller with reference AFR = 0.925

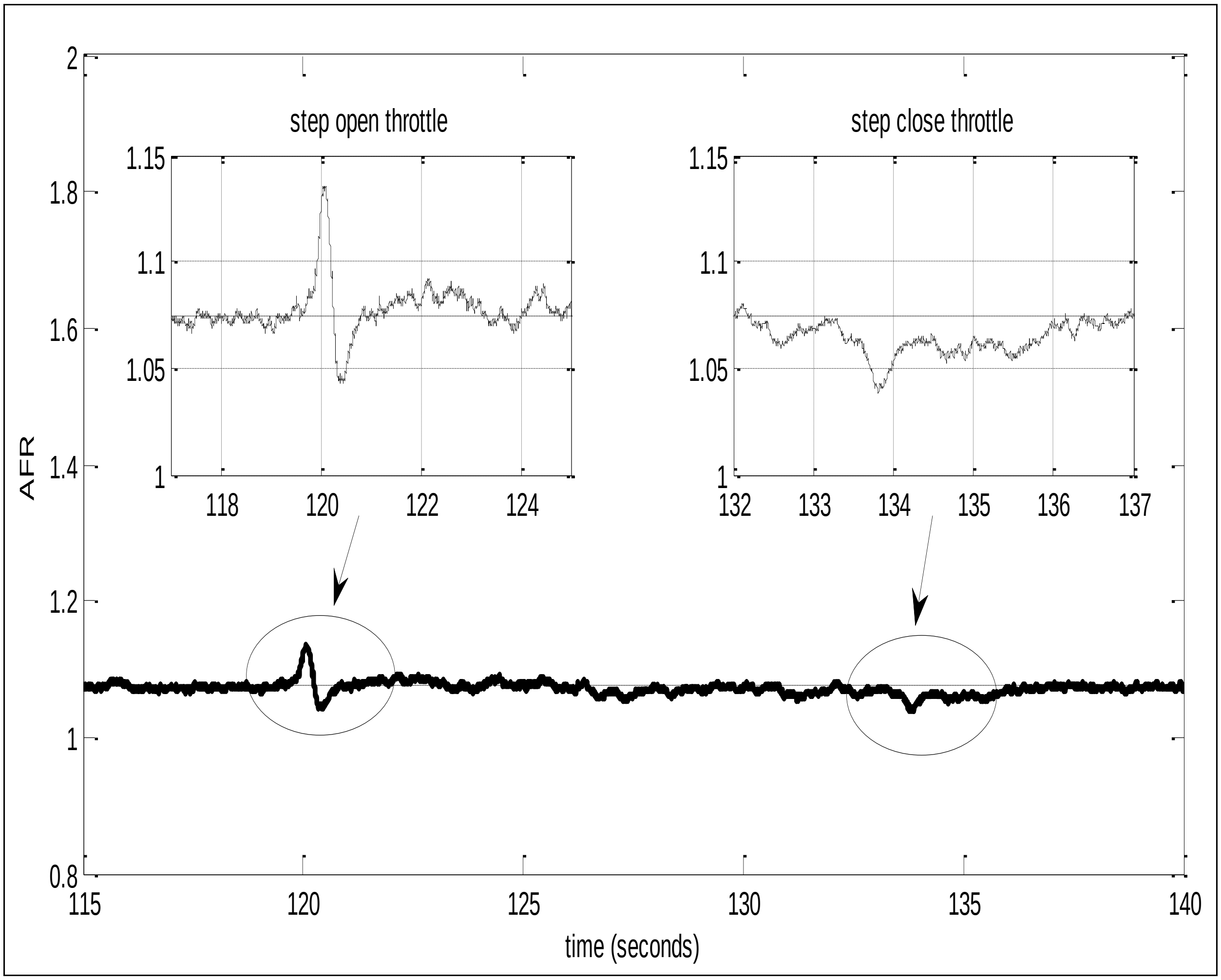

Figure 4-24: Response of LQ tracking controller with reference AFR = 1.075

The LQ tracking controller uses the same modeled wall wetting dynamics as the wall wetting dynamics that are added to the output of the injector pulse width signal. The performance of the controller is acceptable, but if the modeled wall wetting dynamics in the controller differ from the actual wall wetting dynamics of a PFI system, the performance of the controller could be different. To investigate this situation, consider new wall wetting parameters $\alpha = 0.475$ and $\beta = 0.76$. These parameter values were used in the wall wetting dynamics transfer function in equation (102) and the transfer function was added to the output of the injector pulse width signal. The performance of the LQ tracking controller with the new wall wetting parameters, Figure 4-25, shows that the LQ tracking controller is able maintain the AFR deviation from stoichiometry to less than 9% despite the variation in the modeled wall wetting parameters.

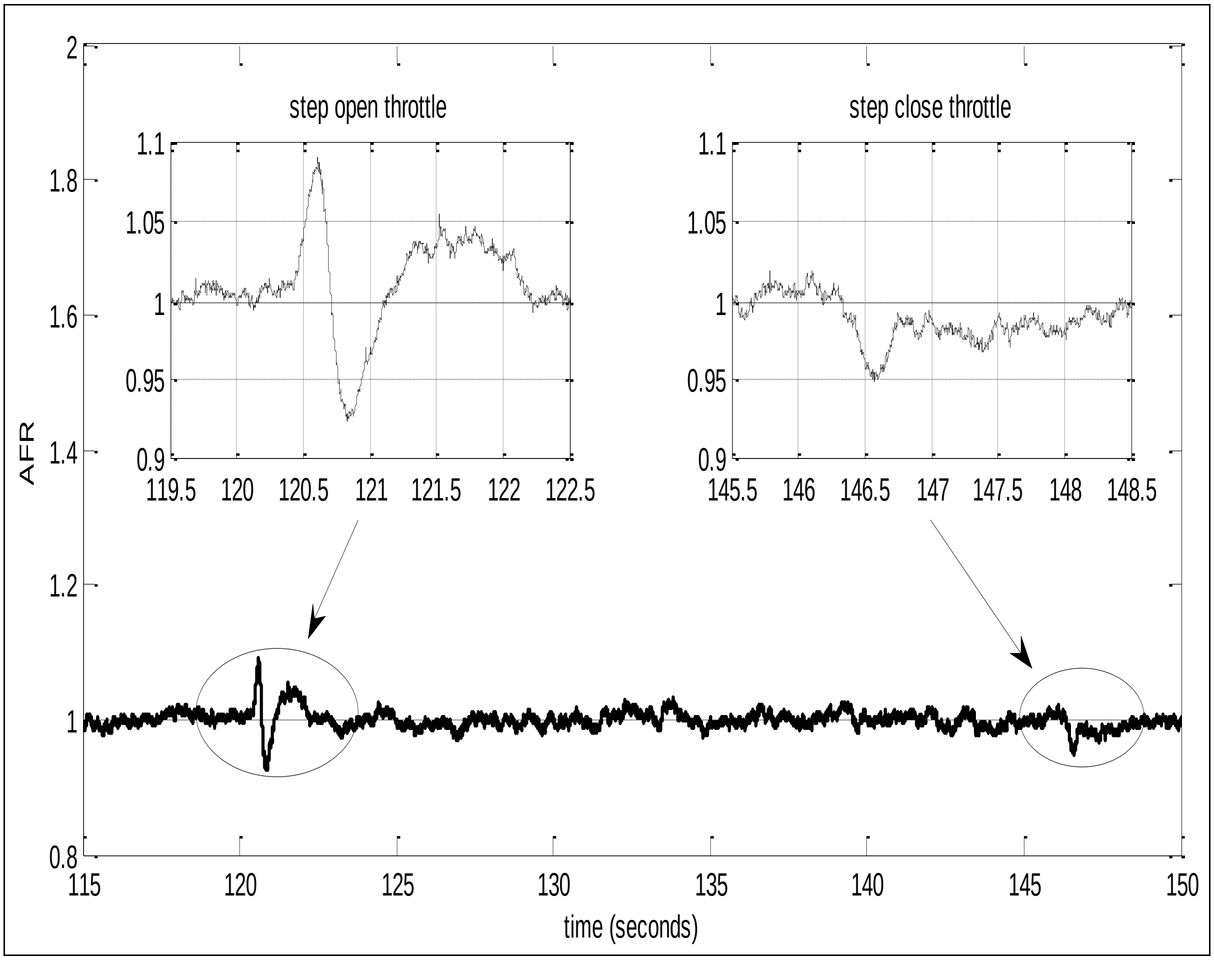

Figure 4-25: Response of LQ tracking controller with new wall wetting parameters

4.5.2 Inverse Fueling Dynamics Feedfoward Control Results

Engine tests were conducted to compare the LQ tracking controller, where the wall wetting dynamics were added to the output of the injection pulse, to the conventional inverse fueling dynamics feedforward control. This controller was implemented in the Opal-RT and was sampled every 10 ms, similar to the LQ tracking controller. For this case, where the DI injector is used with the wall wetting dynamics added to the output of the fuel injection pulse, the schematic for the inverse fueling feedforward controller is shown in Figure 4-26. The response of the inverse fueling dynamics controller is shown in Figure 4-27 and it can be seen that the deviation of the AFR from stoichiometry is 10.2% for the step increase of the air flow and 6.13% for the step decrease.

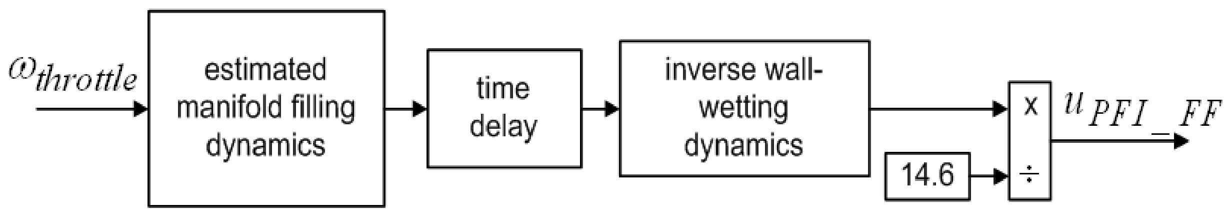

Figure 4-26: Schematic of inverse fueling dynamics feedforward controller

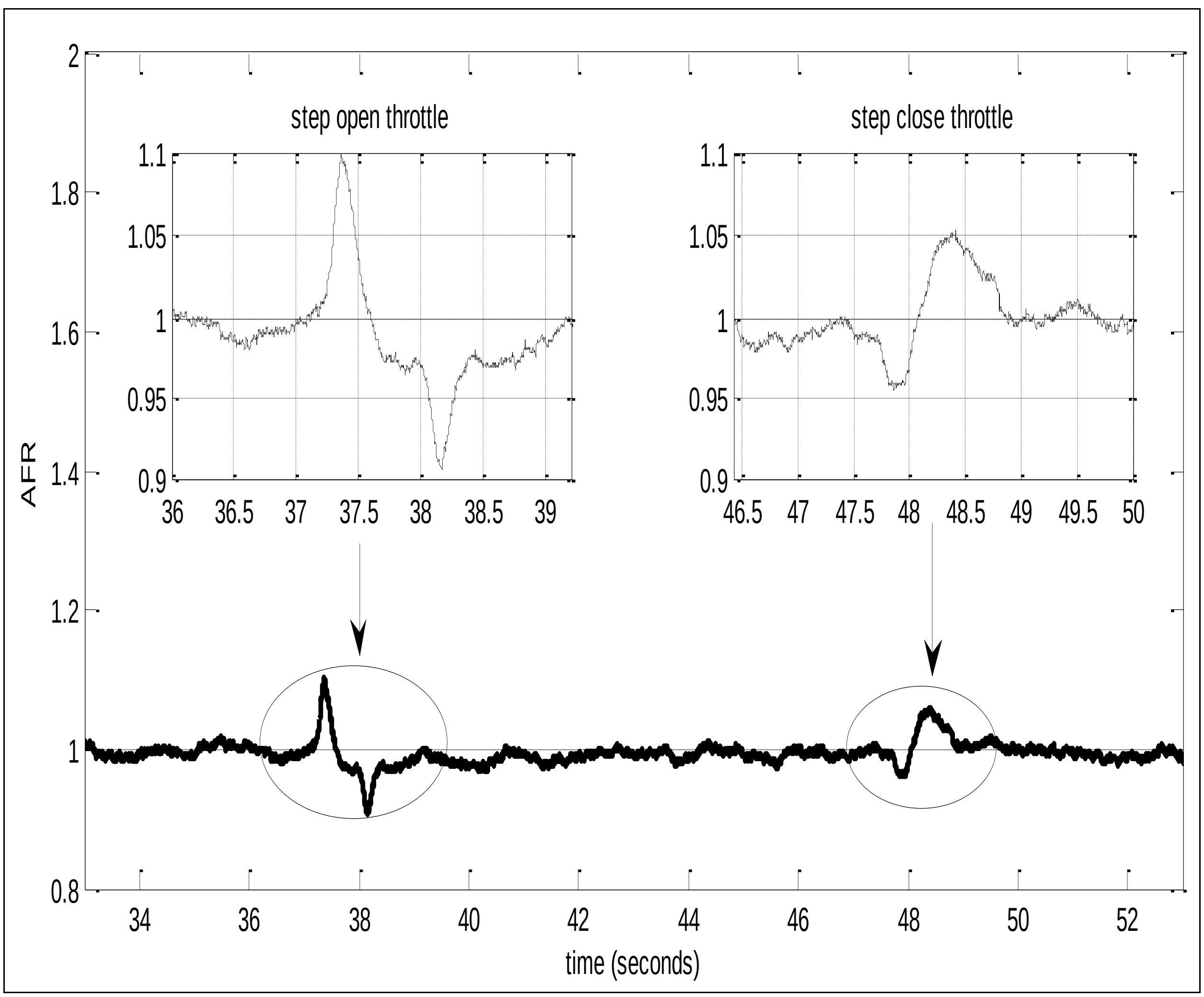

Figure 4-27: Response of inverse fueling dynamics feedforward controller

4.5.3 LQ Tracking Feed Forward Control with PID Feedback Control Results

Similar to the case without wall wetting dynamics added to the output of the fuel injection pulse width, a PID controller that uses the oxygen sensor signal as feedback was designed and implemented with the LQ tracking controller. The controller gains were tuned online in the same way as described in Section 4.4.3 such that the system maintained stability with very little oscillations, and the transient response was acceptable. The PID gains that were used for this engine test are shown in Table 4-5. The response of the AFR when a step increase and decrease in air flow were applied is shown in Figure 4-28. Notice that the AFR deviation from stoichiometry for the step increase and decrease in air flow is 4.67% and 5.78%, respectively, and the settling time is less than 1 second for both increase and decrease. Compared to the LQ tracking feedforward control without the PID feedback control added, this is an improvement of the AFR response when the PID feedback controller is added. When the PID feedback control is added, there is a slight increase in the AFR deviation from stoichiometry for the step decrease in air flow, but the settling time is less. Table 4-6 shows the performance comparison of the LQ tracking controller, inverse fueling feedforward controller, and LQ tracking control with PID feedback control.

K_P	0.01
K_I	0.0005
K_D	0.0001

Table 4-5: PID feedback control gains used for engine tests

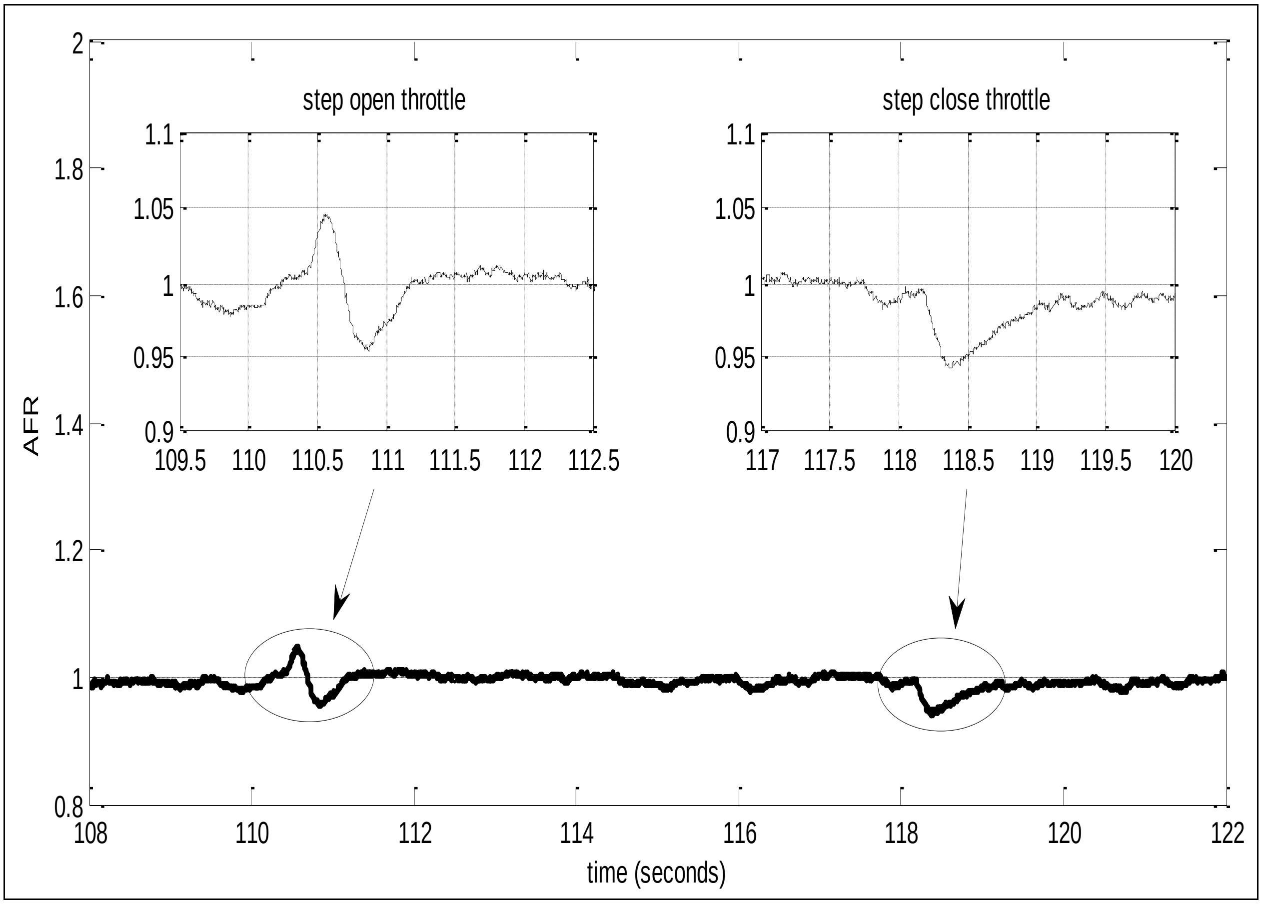

Figure 4-28: Response of LQ tracking with PID feedback controller

	Maximum AFR Deviation		Settling Time	
	step increase	step decrease	step increase	step decrease
LQ Tracking w/state est.	7.87%	3.107%	1.22 sec	0.952 sec
Inverse Fueling	10.2%	6.13%	2.77 sec	1.99 sec
LQ Tracking w/PID	4.67%	5.78%	0.836 sec	0.807 sec

Table 4-6: Comparison of controllers for stoichiometric reference AFR

4.6 Discussion of Engine Test Results

From the engine test results, it can be observed that the case when wall wetting dynamics are added to the output of the fuel injection pulse width, the performance of the LQ tracking controller is better. Without the wall wetting dynamics, the DI system physically no fueling dynamics, thus all of the fuel that is sprayed by the DI system goes into the cylinder.

Theoretically, this should be advantageous. Since the goal is to minimize the AFR deviations, it is more desirable to have the ability to inject the precise amount of fuel needed to maintain the AFR at a desired value as the air quantity in the cylinder changes. It was found that this was not the case in the experimental tests, since the injected fuel flow into the cylinder seems to be slightly faster than the air flow during engine transient operation.

On the other hand, when wall wetting dynamics are added to the output of the fuel injection pulse width, the DI system now has some fueling dynamics. Although these fuel dynamics do not physically occur, they emulate the wall wetting dynamics of a PFI injector. These dynamics improve the LQ tracking performance because the fuel flow and air flow into the cylinder match very nicely.

Figure 4-29 and Figure 4-30 shows the response of injection pulse width for the DI system with and without the wall wetting dynamics, respectively, for engine transient operations when air flow increases and decreases. Notice that the response of injection pulse width is slightly different for both cases. More specifically, when there is an increase in the air flow, corresponding to an increase in the injection pulse width, the pulse width settles more smoothly, resulting from the additional wall wetting dynamics. This causes the AFR deviation to decrease and the smoother settling of the injection pulse width can be seen when comparing the two figures.

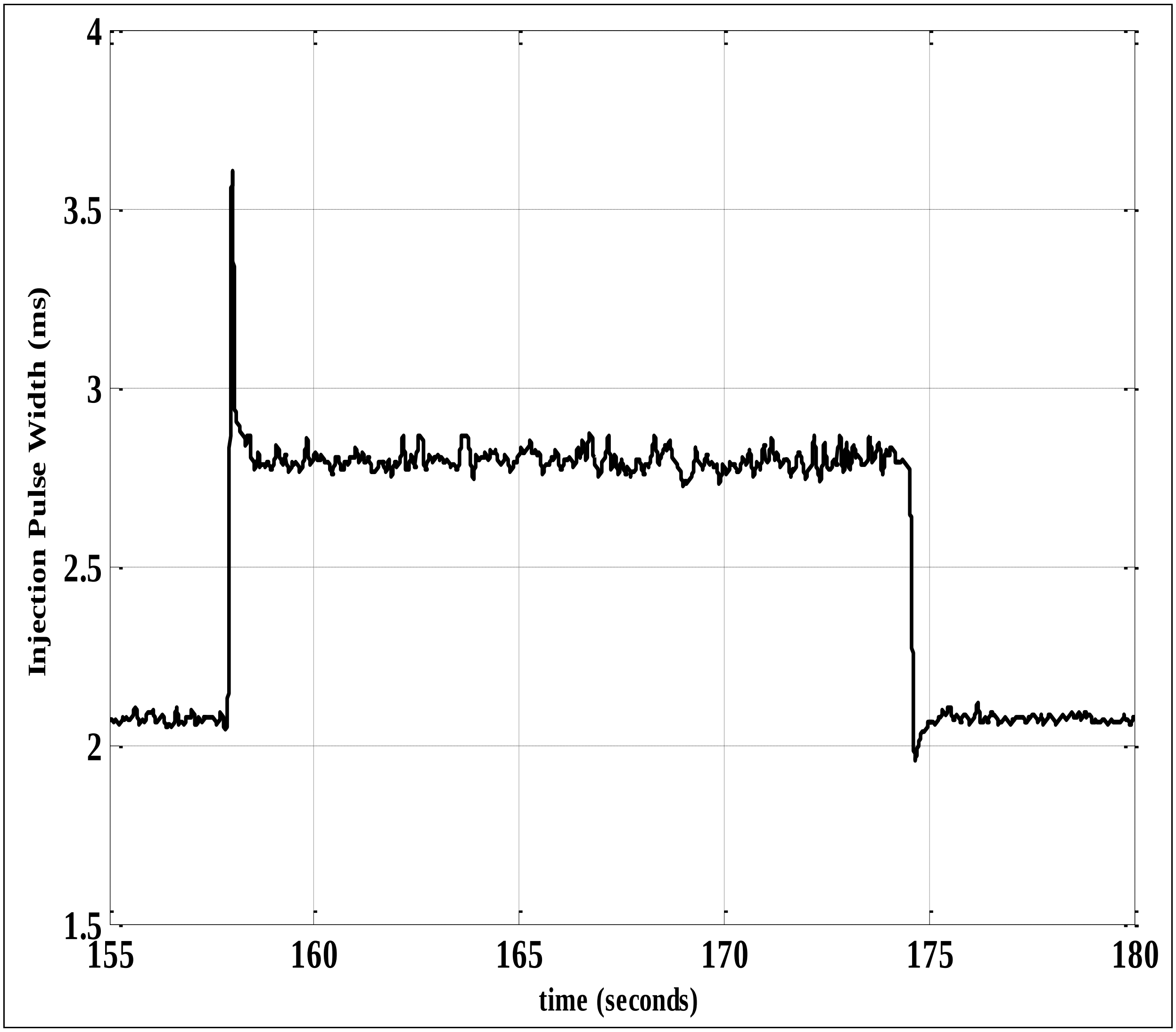

Figure 4-29: Response of DI system without wall wetting dynamics

Also from the engine test results, it can be observed when adding the PID feedback control with the LQ tracking feedforward control for both DI cases that the deviation of the AFR from stoichiometry is smaller than the LQ tracking controller by itself. Although the deviation is less, the settling time is significantly longer; see Table 4-4 and Table 4-6.

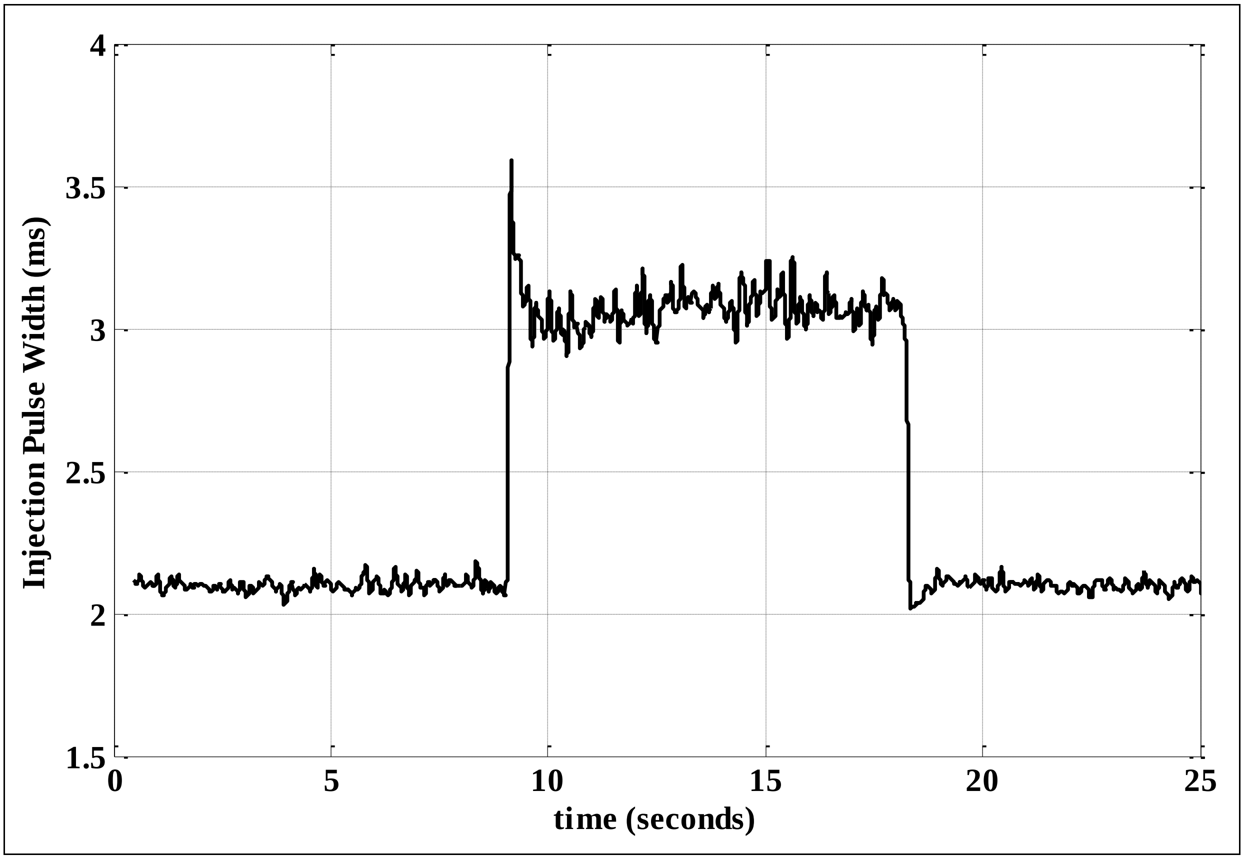

Figure 4-30: Response of DI system with wall wetting dynamics

Chapter 5: EGR and In-Cylinder Gas Temperature Control of an HCCI Internal Combustion Engine

5.1 Introduction

In this chapter, the modeling work of the air and EGR flow into the cylinder and the control problem for the EGR and in-cylinder gas temperature of a homogeneously charged compression ignition (HCCI) engine is presented. The previous control strategies and applications were designed specifically for spark ignited internal combustion engines, where the combustion process of the in-cylinder air-fuel mixture is initiated by an electrical spark from a spark plug. This type of combustion process has been studied for many decades and significant enhancements have been achieved, but there is always room for improvement. A different type of internal combustion process is compression ignition, where the heat of compression is used to initiate the combustion process to burn the air-fuel mixture trapped in the cylinder during the compression stroke. This type of combustion is called homogeneously charged compression ignition (HCCI). To accurately control the start of combustion (SOC) and burn duration of the HCCI combustion, the air-fuel charge mixture temperature and EGR fraction needs to be controlled accurately. In the future work presented at the end of this Chapter, an optimal control scheme will be used to control the in-cylinder charge mixture temperature and EGR fraction.

5.2 HCCI Combustion Mode

Homogeneously charged compression ignition (HCCI) combustion is a very promising combustion mode for internal combustion (IC) engines because it has the ability of meeting stringent federal and state emission regulations with improved fuel economy. In an HCCI capable IC engine, ignition is initiated by compressing the air-fuel mixture in the cylinder without using a spark plug. Therefore, HCCI combustion results in a flameless, low temperature burn that produces less NOx and better fuel economy. Furthermore, HCCI capable SI engines have been found to have very high fuel efficiency with significantly reduced NOx formation and reduced engine pumping loss ([20] and [21]).

5.2.1 Motivation of In-Cylinder Gas Temperature Control

Although the HCCI combustion starts without spark, it still requires an increased charge temperature (i.e. 450K) and other cylinder charge conditions to start the combustion process, and therefore its engine operational condition is limited. It is limited at cold start and low engine load conditions due to the lack of sufficient thermal energy to trigger auto-ignition of the air-fuel mixture in the compression stroke, and at high engine speed and high engine load due to audible engine knock [28]. Therefore, HCCI combustion requires another combustion type, such as spark ignited (SI), to operate the engine in its full operational range. Since a specific in-cylinder gas temperature, among other charge conditions, is very critical to HCCI ignition, the control of this temperature must be taken into consideration and is first component of the motivation of this work.

5.2.2 Motivation of EGR Control

Since auto-ignition timing of HCCI combustions is determined by the cylinder charge conditions, rather than the spark timing as is the case in SI combustion, regulating the charge properties, such as temperature, pressure, and composition at intake valve closing (IVC) has been the focus of many HCCI combustion researchers. Furthermore, researchers have shown that variable valve timing (VVT) can influence the mixing conditions at IVC ([29] and [30]). Early exhaust valve closing (EVC) and late intake valve opening allow internal exhaust gas recirculation (EGR) with high temperature to be trapped in the cylinder, and this can alleviate some of the preheating that is needed to begin auto-ignition [31].

Most HCCI capable SI engines are equipped with both intake and exhaust variable valve timing (VVT) and an external cooled exhaust gas recirculation (EGR) system which can allow the in-cylinder gas temperature and EGR fraction to be regulated. There has been various research conducted on the effects of external EGR on HCCI combustion including [32], [33], [34], and [35], and several EGR control schemes for HCCI combustion such as a robust control of external EGR [27] and model based control of EGR [36]. Therefore, the design of external EGR and internal EGR control coupled together to adjust the mixing temperature before ignition is the second component of the motivation of this work

5.3 EGR and In-Cylinder Gas Temperature Control Problem

Internal EGR is used primarily to increase the in-cylinder air-fuel mixture temperature at IVC so that HCCI combustion can be initiated, and the external EGR is used to add another degree of freedom to control both charge temperature and EGR fraction. During the gas exchange phase of the engine combustion process, the timing of exhaust valve closing and intake valve opening is used to control the in-cylinder air-fuel mixture temperature. More specifically, negative valve overlap (NVO), defined as the duration in crank angle in degrees between exhaust valve closing and intake valve opening, is used to adjust the EGR fraction gas temperature. Consequently, the in-cylinder air-fuel mixture temperature can be optimized for the desired SOC for HCCI. Therefore, the control objective of this work is to maintain both the in-cylinder air-fuel mixture temperature and EGR fraction at desired values. Figure 5-1 shows the control schematic EGR and in-cylinder gas temperature controller.

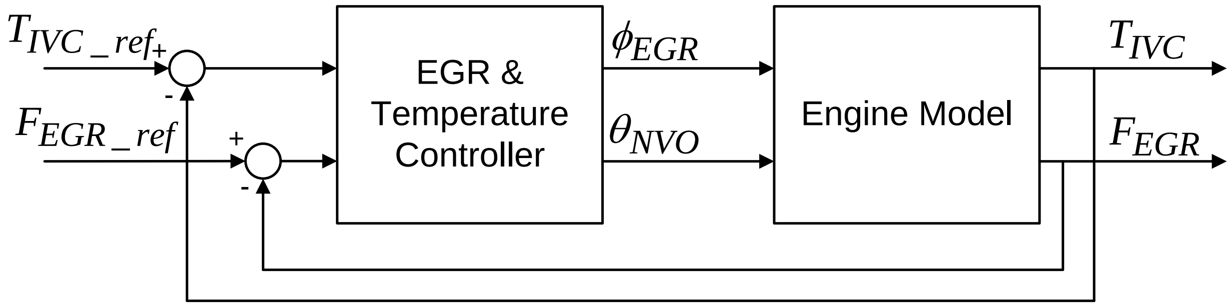

Figure 5-1: EGR and in-cylinder gas temperature control schematic

Since the control objective is to maintain both the in-cylinder air-fuel mixture temperature and EGR fraction at desired values, it is assumed that the EGR quantity and exhaust gas temperature can be measured indirectly or estimated. In some cases, the EGR fraction can be calculated by comparing the CO_2 concentration in the pre-combustion gas with the exhaust gas from the previous cycle. Therefore, the signals T_{IVC} and F_{EGR} corresponding to the in-cylinder gas temperature at intake valve closing and the EGR fraction, respectively, are available and will be used by the controller to determine the EGR throttle plate position (ϕ_{EGR}) and negative valve overlap duration (θ_{NVO}) needed to achieve the desired reference values T_{IVC_ref} and F_{EGR_ref}.

5.4 EGR and In-cylinder Gas temperature Model

To begin the design of an EGR and in-cylinder gas temperature controller, a control oriented model of the external EGR system and intake and exhaust VVT system is needed. First, consider the exhausted gas feedback from the exhaust manifold to intake manifold to have a pure time delay, typically 100 ~ 150 ms. This exhausted gas is cooled and passed through an external EGR throttle plate, with dynamics modeled by a first order transfer function as

$$\omega_{EGR\_throttle} = \frac{1}{\tau_1 s + 1} u_{EGR\_ext} \tag{103}$$

where u_{EGR_ext} is the EGR throttle actuator command, and $\omega_{EGR\_throttle}$ is the air flow across the EGR throttle valve. After passing through the EGR throttle, the cooled exhausted gases are combined with the fresh air in the intake manifold and are finally mixed with fuel in the intake runner. The air-fuel mixture is sucked into the cylinder and together with the hot internal EGR, due to exhaust VVT, combustion occurs. Figure 5-2 shows the schematic flow of the external EGR from exhaust manifold to engine cylinder.

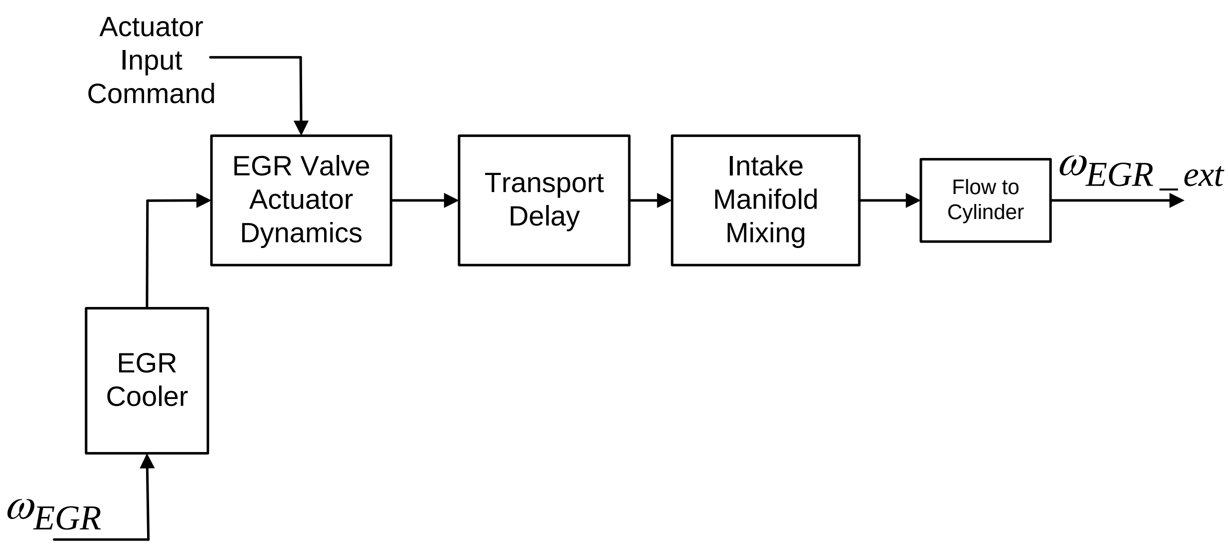

Figure 5-2: External EGR flow schematic

Next, consider a discretized isothermal model of the filling dynamics of an engine intake manifold,

$$\frac{P_{in}(k+1) - P_{in}(k)}{\Delta t_s} = \frac{RT_{in}}{V_{in}} \left(\omega_{throttle}(k) - \omega_{cyl}(k) + \omega_{EGR\_ext}(k) \right) \tag{104}$$

where the index k represents the engine cycle number, P_{in} is the intake manifold gas pressure, R is the gas constant, T_{in} is the intake manifold gas temperature, and V_{in} is the intake manifold volume. The air mass flow into the cylinders is modeled using the speed density equation (104) as

$$\omega_{cyl}(k) = \eta_{vol}\left(N_{engine}, P_{in}\right)\frac{N_{engine}}{2R \cdot T_{in}} V_{IVC}(k) \cdot P_{in}(k), \tag{105}$$

where η_{vol} is the volumetric efficiency, which is a highly nonlinear function of the engine speed, N_{engine}, and intake manifold pressure and V_{IVC} represents the volume of the cylinder at intake valve closing.

The air flow through the external EGR valve, ω_{EGR}, can be approximated using the standard office equation as

$$\omega_{EGR}(k) = \frac{C_d A}{\sqrt{R \cdot T_{in}}}\psi\left(\frac{P_{exh}}{P_{in}}\right) \cdot P_{in}(k), \tag{106}$$

where C_d is the valve discharge coefficient, A is valve opening area, P_{exh} is the exhaust manifold gas pressure, and

$$\psi(x) = \begin{cases} \sqrt{2x(1-x)}, & \text{if} \quad 1/2 < x < 1 \\ 1/\sqrt{2}, & \text{if} \quad x < 1/2 \end{cases}. \tag{107}$$

Note that Δt_S is the sampling rate, a function of engine speed, given as

$$\Delta t_S = \frac{120}{N_{engine}}. \tag{108}$$

The air flow across the engine throttle, $\omega_{throttle}$, is assumed to be known since it can be measured by the engine mass air flow sensor.

5.5 Future Work

Future works of the EGR and in-cylinder gas temperature control include continuing to research and simplify equations that describe the air flow and EGR flow into the cylinder in order to construct a state space model that can be used for control design. Upon constructing a control oriented model that describes the dynamics of the air flow and EGR flow into the cylinder, the design of the EGR and in-cylinder gas temperature controller will begin. Simulations will be conducted both in Matlab Simulink and in hardware-in-the-loop (HIL) environment. Upon satisfactory results from HIL simulations, real engine tests will be ran to further validate the controller design.

Chapter 6: Conclusions

6.1 Nonlinear Control of AFR and Fuel Ratio Conclusions

A multi-input-multi-output sliding mode controller, with state estimator, was developed based upon a simplified nonlinear equivalence and fuel ratio model to achieve nonzero desired equivalence and fuel ratio targets and validated in a HIL simulation environment where the engine control model is the “hardware”. The performance of the state feedback sliding mode controller was compared with that of the ad hoc multi-loop PID controller against the developed control oriented dual-fuel system model in Matlab simulations. The state feedback sliding mode controller showed improved performance over the ad hoc multi-loop PID controller. A state estimator with variable parameter gain was designed with guaranteed stability. The HIL simulations were then conducted, where the sliding mode controller feedback with estimated states was implemented into an ECM (“hardware”) and a three cylinder mixed mean value and crank resolved dual-fuel engine model was used. The HIL simulations achieved comparable performance to those obtained from the Matlab simulations, which indicated that implementation of the developed output feedback sliding mode controller in a production engine control module controller with satisfactory performance is feasible.

6.2 Optimal LQ Transient AFR Control Conclusions

The LQ optimal tracking controller was developed to minimize the air-to-fuel ratio tracking error, especially under the transient operations. Control simulations were conducted using a mean value engine model and show that under the optimal LQ tracking control the deviation of the AFR from the reference one is under 2% for all engine transient operational conditions. Furthermore, it showed significant overshoot reduction over the baseline (conventional) inverse fueling dynamics controller. The real-time control simulation was conducted under the hardware-in-the-loop simulation environment and the validation in engine dynamometer is the focus of potential future work.

6.3 Experimental Tests Conclusions

Engine test were conducted on a single cylinder research engine to validate the ability of the LQ tracking feedfoward control to reduce the deviation of the AFR from a desired value during engine transients. For the DI case when no wall wetting dynamics were added to the output of the fuel injection pulse width, the performance of the LQ tracking feedforward controller was able to maintain the AFR deviation to less than 8.5% for each engine transient and to less than 7.5% when the PID feedback control was added. Furthermore, it showed significant overshoot reduction over the baseline (conventional) inverse fueling controller.

Similarly, for the case when wall wetting dynamics were added to the output of the DI injector, the LQ tracking feedforward controller was able to maintain the AFR deviation to less than 8% for each engine transient and to less than 6% when the PID feedback control was added. Furthermore, the performance of the LQ tracking feedforward controller reduced the AFR deviation during engine transients much better than the baseline inverse fueling dynamics controller.

It is important to note that there was a significant fueling delay in the Opal-RT engine controller. This delay is from when the fuel control command was determined by the controller to when it was sent to the injector. This delay, which was determined to be 200 ms, was caused by the hardware and software limitations of the Opal-RT engine controller and is the main reason that the deviation of the AFR was much larger during the engine test than in simulation environment. In the presence of this delay, the performance of the LQ tracking controller was acceptable and has the potential to be implemented on a production engine.

6.4 Future Work

The AFR control performance of the LQ tracking feedforward control with PID closed loop control for both the DI and PFI cases were improved over that with the LQ tracking feedforward control only. This shows that there is still room to improve the LQ tracking controller by making the model used for the LQ tracking controller closer to the physical engine system.

For future work, it is proposed to improve the LQ tracking controller by accurately modeling the time delays of the fuel injection, the intake manifold filling dynamics and the throttle dynamics. Currently the fuel injection time delay is not modeled in the LQ tracking controller directly and it was added to the delay of the intake air flow. Matching these models with the physical systems should reduce the AFR tracking error significantly for the transient engine operations when the LQ tracking control is used.

BIBLIOGRAPHY

BIBLIOGRAPHY

[1] J. B. Heywood, *Internal Combustion Engine Fundamentals*: McGraw-Hill, 1988.

[2] G. Zhu, et al, "Closed-Loop Ignition Timing Control for SI Engines Using Ionization Current Feedback," *IEEE Trans on Control Systems*, pp. 416-427, May 2007.

[3] J. G. Rivard, "Closed-loop Electronic Fuel Injection Control of the IC Engine," in *Society of Automotive Engineers*, 1973.

[4] J. F. Cassidy, et al, "On the Design of Electronic Automotive Engine Controls using Linear Quadratic Control Theory," *IEEE Trans on Control Systems,* vol. AC-25, October 1980.

[5] W. E. Powers, "Applications of Optimal Control and Kalman Filtering to Automotive Systems," *International Journal of Vehicle Design*, vol. Applications of Control Theory in the Automotive Industry, 1983.

[6] N. F. Benninger, et al, "Requirements and Performance of Engine Management Systems under Transient Conditions," in *Society of Automotive Engineers*, 1991.

[7] C. H. Onder, et al, "Model-Based Multivariable Speed and Air-to-Fuel Ratio Control of an SI Engine," in *Society of Automotive Engineers*, 1993.

[8] S. B. Cho, et al, "An Observer-based Controller Design Method for Automotive Fuel-Injection Systems," in *American Controls Conference*, 1993, pp. 2567-2571.

[9] T. Kume, et al, "Combustion Technologies for Direct Injection SI Engine," in *Society of Automotive Engineers*, 1996.

[10] Y. Yildiz, et. al., "Adaptive Air Fuel Ratio Control for Internal Combustion Engines," in *American Control Conference* Seattle, WA, 2008.

[11] S. Pace, et. al., "Sliding Mode Control of a Dual-Fuel System Internal Combustion Engine," in *ASME Dynamic Systems and Control Conference* Hollywood, CA, 2009.

[12] A. White, et. al., "Gain-scheduling control of port-fuel-injection processes," in *American Controls Conference* Baltimore, MD, 2010.

[13] A. Kyung-ho, et. al., "Puddle Dynamics and Air-to-Fuel Ratio Compensation for Gasoline-Ethanol Blends in Flex-Fuel Engines," *IEEE Transactions on Control Systems Technology*, vol. 18, pp. 1241-1253, 2010.

[14] C. Chang, et. al., "Air-Fuel Ratio Control in Spark-Ignition Engines Using Estimation Theory," *IEEE Transactions on Control Systems Technology*, vol. 3, pp. 22-31, 1995.

[15] Y. Zhai, et. al., "Radial-basis-function-based Feedforward-feedback Control for Air-fuel Ratio of Spark Ignition Engines,," *IMechE Journal of Automobile Engineering*, vol. 222, pp. 415-428, 2008.

[16] J. Grizzle, et. al., "Improved Cylinder Air Charge Estimation for Transient Air Fuel Ratio Control," in *American Controls Conference* Baltimore, MD, 1994.

[17] A. Osburn, et. al., "Transient air/fuel ratio controller identification using repetitive control," *ASME Journal of Dynamic Systems, Measurement and Control,* vol. 126, pp. 781–789, 2004.

[18] R. Cipollone, et. al., "Transient Air/Fuel ratio control in SI engines," in *ASME Internal Combustion Engine Division Fall Technical Conference* New Orleans, LA, 2002.

[19] F. Zhang, et. al., "Transient Lean Burn Air-fuel Ratio Control using Input Shaping Method combined with Linear Parameter-Varying Control," in *American Controls Conference* Minneapolis, MN, 2006.

[20] P. Najt, et. al., "Compression-Ignited Homogeneous Charge Combustion," Society of Automotive Engineers, 1983.

[21] X. Yang, et. al., "A Control Oriented SI and HCCI Hybrid Combustion Model for Internal Combustion Engines," in *ASME Dynamic Systems and Control Conference* Cambridge, MA, 2010.

[22] N. Ravi, et. al., "Model-Based Control of HCCI Engines Using Exhaust Recompression," *IEEE Transactions on Control Systems Technology*, vol. 18, pp. 1289-1302, 2010.

[23] J. Kang, et. al., "Sufficient Condition on Valve Timing for Robust Load Transients in HCCI Engines," SAE International, 2010.

[24] G. M. Shaver, "Physics based modeling and control of residual-affected HCCI engines using Variable Valve Actuation," Stanford University, 2005.

[25] M. J. Roelle, Shaver, G. M., and Gerdes, J. C., " "Tackling the Transition: A Multi-Mode Combustion Model of SI and HCCI for Mode Transition Control,”" in *International Mechanical Engineering Conference and Exposition* Anaheim, CA, 2004.

[26] Y. Zhang, et. al., "Study of SI-HCCI-SI Transition on a Port Fuel Injection Engine Equipped with 4VVAS," Society of Automotive Engineers, 2007.

[27] J. Kang, et. al., "HCCI engine control strategy with external EGR," in *American Control Conference* Baltimore, MD, 2010.

[28] F. Zhao, et. al., "Homogeneous Charge Compression Ignition (HCCI) Engines Key Research and Development Issues," Society of Automotive Engineers, 2003.

[29] J. Martinez-Frias, et. al., "HCCI Control by Thermal Management," Society of Automotive Engineers, 2000.

[30] D. S. Stanglmaier, et. al., "Homogenous Charge Compression Ignition (HCCI): Benefits, Compromises, and Future Engine Applications," Society of Automotive Engineers, 1999.

[31] G. Kontarakis, et. al., "Demonstration of HCCI Using a Single Cylinder Four-stroke SI Engine With Modified Valve Timing," Society of Automotive Engineers, 2000.

[32] T. Ohmura, et. al., "Study on Combustion Control by Using Internal and External EGR for HCCI Engines Fuelled with DME," Society of Automotive Engineers, 2006.

[33] X. Lu, et. al., "A fundamental study on the control of the HCCI combustion and emissions by fuel design concept combined with controllable EGR, part 1: The Basic Characteristics of HCCI combustion," *Fuel,* vol. 84, pp. 1074–1083, 2005.

[34] X. Lu, et. al., "A fundamental study on the control of the HCCI combustion and emissions by fuel design concept combined with controllable EGR, part 2: Effect of operating conditions and EGR on HCCI combustion," *Fuel,* vol. 84, pp. 1084–1092, 2005.

[35] A. Amit Bhave, et. al., "Evaluating the EGR-AFR Operating Range of a HCCI Engine," Society of Automotive Engineers, 2005.

[36] N. Ravi, et. al., "A Physically Based Two-State Model for Controlling Exhaust Recompression HCCI in Gasoline Engines," in *Proceedings of International Mechanical Engineering Conference and Exposition* Chicago, IL, 2006.

[37] C. Aquino, "Transient A/F Control Characteristics of the 5 Liter Central Fuel Injection," Society of Automotive Engineers, 1981.

[38] X. Yang, et. al., "A mixed mean-value and crank-based model of a dual-stage turbocharged SI engine for hardware-in-the-loop simulation," in *American Controls Conference* Baltimore, MD, 2010.

[39] H. Khalil, *Nonlinear Systems*, 3 ed.: Prentice Hall, 2002.

[40] M. Won, et al, "Air to Fuel Ratio Control of Spark Ignition Engines Using Dynamic Sliding Mode Control and Gaussian Neural Network," in *American Controls Conference* Seattle, WA, 1995.

[41] J. Souder, et. al., "Adaptive Sliding Mode Control of Air-Fuel Ratio in Internal Combustion Engines," *International Journal of Robust and Nonlinear Control,* vol. 14, pp. 524-541, 2004.

[42] D. G. Luenberger, "Observers for Multivariable Systems," *IEEE Trans on Automatic Control*, vol. AC-11, pp. 190-197, 1966.

[43] M. Soliman, et. al., "Exponential stabilization of LPV systems: An LMI approach," in *Canadian Conference on Electrical and Computer Engineering* Niagara Falls , Ontario, Canada, 2008.

[44] S. Boyd, et. al., *Linear Matrix Inequalities in System and Control Theory*. Philadelphia, PA: SIAM, 1994.

[45] L. Guzzella, *Introduction to Modeling and Control of Internal Combustion Engine Systems*: Springer-Verlag Berlin Heidelberg, 2004.

[46] "http://www.opal-rt.com/," 2011.

[47] "http://mcs.woodward.com/," 2011.

[48] D. L. Stivender, "Engine air control – basis of a vehicular systems control hierarchy," in *Society of Automotive Engineers*, 1978.

[49] S. D. Hires, et. al., "Transient mixture strength excursions– an investigation of their causes and the development of a constant mixture strength fuelling strategy," in *Society of Automotive Engineers*, 1981.

[50] D. Rose, et. al., "In-cylinder mixture excursions in a port-injected engine during fast throttle opening," in *Society of Automotive Engineers*, 1996.

[51] N. Ladommatos, et. al., "Measurements of in-cylinder mixture strength and fuel accumulation in the inlet port of a gasoline-injected engine during very rapid throttle openings," *IMechE,* vol. 212, 1998.

[52] N. Ladommatos, et. al., "On the causes of in-cylinder air-fuel ratio excusions during load and fuelling transients in port-injected spark-ignition engines," in *Society of Automotive Engineers*, 1998.

[53] H. Xu, "Control of A/F Ratio During Engine Transients," in *Society of Automotive Engineers*, 1999.

[54] Z. Ye, "A Simple Linear Approach for Transient Fuel Control," in *Society of Automotive Engineers*, 2003.

[55] J. Yao, "Research on Transient Air Fuel Ratio Control of Gasoline Engines," in *International Forum on Information Technology and Applications*, 2009.

[56] D. Naidu, *Optimal Control Systems*: CRC Press, 2003.

[57] F. M. White, *Fluid Mechanics*, 6 ed. New York: McGraw-Hill, 2008.

[58] "http://www.aanddtech.com/CAS.html," 2011.